UNIVERSITE SAAD DAHLAB DE BLIDA 1

Faculté de Technologie

Département de Mécanique

THESE DE DOCTORAT (LMD)

En Génie Mécanique

Spécialité : Construction Mécanique

Etude dynamique des plaques nano composites fissurées par la méthode des éléments finis étendue (X-FEM).

Dynamic study of cracked nanocomposite plates using the extended finite element method (X-FEM).

Par

MAOUDJ Samah

Devant le jury composé de :

KIRAD Abdelkader	Pr, Univ. Blida1	Président
HACHI Brahim Elkhalil	Pr, Univ Djelfa	Examinateur
CHIKER Yasser	MCA, Univ Yahia Fares, Medea	Examinateur
TIBERKAK Rachid	Pr, Univ. Blida1	Directeur de Thèse
EZZRAIMI Madjid	MCA, Univ. Blida1	Co-directeur de Thèse

Blida, 2025

ملخص

تتناول هذه الدراسة بشكل معمّق السلوك الاهتزازي الحر للصفائح المتشققة المصنوعة من مواد مركبة ذات تدرج وظيفي ومُدعّمة بأنابيب نانوية كربونية، باستخدام طريقة العناصر المحددة الموسعة، تدرس هذه الدراسة تأثير نماذج التوزيع المختلفة للأنابيب النانوية الكربونية على الخصائص الاهتزازية، مع الأخذ في الاعتبار السلوك غير الخطي للأنابيب النانوية الكربونية وتأثير تسلسل التكديس في الرقائق. وباستخدام نظرية التشوه من المرتبة الأولى، تم تنفيذ منهج مشترك بين طريقة العناصر المحددة و طريقة العناصر المحددة الموسعة لنمذجة الشقوق بكفاءة دون الحاجة إلى إعادة توليد الشبكة. تم حساب معامل المرونة الفعّال للمادة المركبة باستخدام نموذج Halpin-Tsai المعدل، كما تم التنبؤ بالخصائص المرنة لطبقات FG-CNTRCباستخدام قاعدة الخلط.

تكشف هذه التحليلات عن التأثير الكبير لطول الشق، وموقعه، ونسبة العرض إلى السماكة، والنسبة الحجمية للأنابيب النانوية، ومعامل قانون القدرة، على الترددات الطبيعية وصلابة الصفائح FG-CNTRC .

تشير النتائج الرئيسية إلى الصلابة العالية التي توفّرها توزيعات FG-X بفضل التوزيع الاستراتيجي للأنابيب النانوية، وانخفاض الترددات الطبيعية مع زيادة طول الشق، بالإضافة إلى الميزة الأولية في الصلابة للرقائق المتصالبة مقارنة بتكوينات الطبقات الزاوية، والتي تتضاءل مع ازدياد طول الشقوق.

الكلمات المفتاحية: الاهتزاز الحر، صفائح FG-CNTRC ، الشقوق ، طريقة العناصر المحددة الموسعة XFEM ، نظرية التشوه للصفائح من الرتبة الأولى

ABSTARCT

This research investigates the free vibration behavior of cracked Functionally Graded Carbon Nanotube Reinforced Composite (FG-CNTRC) plates using the Extended Finite Element Method (XFEM). The study examines the impact of different CNT distribution patterns (UD, FG-X, FG-A, and FG-O) on the vibrational characteristics, accounting for the influence of laminate stacking sequences. Using First-Order Shear Deformation Plate Theory (FSDT), a combined FEM-XFEM approach is implemented to effectively model cracks without remeshing. The effective elastic modulus of the composite is computed using the modified Halpin-Tsai model, and the elastic properties of CNTRC plies are predicted using the rule of mixtures. This analysis reveals the significant influence of crack length, crack position, width/thickness ratios, fiber volume fraction, and power law index on the natural frequencies and stiffness of FG-CNTRC plates. Key findings highlight the enhanced stiffness achieved with

FG-X distributions due to strategic CNT placement, the reduction in natural frequencies with increasing crack length. The results demonstrate XFEM's accuracy and efficiency as a robust tool for the dynamic analysis of cracked FG-CNTRC structures, offering valuable insights for their design and optimization in demanding applications.

Keywords: free vibration, FG-CNTRC plates, cracks, extended finite element method, first order deformation plate theory

RESUME

Cette recherche étudie de manière approfondie le comportement vibratoire libre des plaques fissurées en composite fonctionnellement graduée renforcé par des nanotubes de carbone (FG-CNTRC) en utilisant la méthode des éléments finis étendue (XFEM). L'étude examine l'impact de différents modèles de distribution de CNT (UD, FG-X, FG-A et FG-O) sur les caractéristiques vibratoires, en tenant compte du comportement non linéaire des CNT et de l'influence des séquences d'empilement des stratifiés. En employant la théorie de déformation au premier ordre (FSDT), une approche combinée FEM-XFEM est mise en œuvre pour modéliser efficacement les fissures sans remaillage. Le module d'élasticité effectif du composite est calculé à l'aide du modèle de Halpin-Tsai modifié, et les propriétés élastiques des plis CNTRC sont prédites à l'aide de la règle des mélanges. Cette analyse révèle l'influence significative de la longueur de la fissure, de la position de la fissure, des rapports largeur/épaisseur, de la fraction volumique des fibres et de l'indice de la loi de puissance sur les fréquences naturelles et la rigidité des plaques FG-CNTRC. Les principaux résultats soulignent la rigidité accrue obtenue avec les distributions FG-X en raison du placement stratégique des CNT, la réduction des fréquences naturelles avec l'augmentation de la longueur des fissures. Les résultats démontrent la précision et l'efficacité de XFEM en tant qu'outil robuste pour l'analyse dynamique des structures FG-CNTRC fissurées, offrant des informations précieuses pour leur conception et leur optimisation dans des applications exigeantes.

Mots-clés : vibration libre, plaques FG-CNTRC, fissures, méthode des éléments finis étendue (XFEM), théorie de la déformation du premier ordre des plaques.

ACKNOWLEDGMENTs

I would first and foremost like to express my deepest gratitude to Allah, for His grace and guidance throughout this endeavor.

This thesis represents the culmination of my studies in the 3rd cycle, from 2021 to 2025, at the University of Blida 1

I owe a debt of gratitude to my supervisor, Pr. Rachid Tiberkak, for his unwavering support, guidance, and encouragement. His advice was invaluable throughout this entire period. I also extend my sincere appreciation to my co-supervisor, Dr. Madjid Ezrraimi, for his contributions to this work.

I am deeply grateful to the members of the jury Pr. KIRAD Abdelkader from university of Blida 1, Dr. CHIKER Yasser from university of Medea and Pr. HACHI Brahim elkhalil from university of Djelfa for accepting to examine my thesis. Their valuable time, expertise, and insightful feedback are sincerely appreciated.

My thanks are also due to all the members of the Structure Laboratory for providing a warm and productive working environment. In particular, I would like to thank my colleague, Ikram Slamani, who became a dear friend during this time.

I wish to express my profound gratitude to my family, especially my parents, for their unwavering belief in me and their steadfast support. Finally, I would like to thank my aunt and her husband HOUBAD Ghaouti for their generous hospitality and for providing me with everything I needed.

Thank you all, very much.

CONTENTS

ABSTRACT.

ACKNOWLEDGMENTS.

CONTENTS.

LIST OF FIGURES.

LIST OF TABLES.

LIST OF SYMBOLS.

LIST OF ABREVIATIONS.

GENERAL INTRODUCTION 1

CHAPTER 1 LITERATURE REVIEW 5

1.1 Introduction 5

1.2 Numerical modeling of cracks 6

1.2.1 Fracture modeling approach 6

1.2.2 Numerical methods for crack simulation 6

1.3 Failure mechanisms in composite materials 8

1.3.1 Matrix cracking 9

1.3.2 Delamination 9

1.3.3 Fiber/Matrix Debonding 10

1.3.4 Fiber breakage 10

1.4 Nanoscale-dependent failure mechanism 10

1.4.1 Fracture 10

1.4.2 Interfacial failure 11

1.4.3 Other failure mechanism: 12

1.5 Vibration of cracked composite plates 12

1.6 Laminated CNT reinforced composite plate 13

1.6.1 Definition of a Laminated Plate 13

1.6.2 The Advantage of Customizable Material Properties 14

1.6.3 Stacking Sequences 14

1.6.4 Fiber Configuration within Each Ply 15

1.7 Conclusion 17

CHAPTER 2 MATERIAL PROPERTIES AND BEHAVIOR……..18
2.1 Introduction 18
2.2 Introduction to Composite Materials 18
2.2.1 Definition 18
2.2.2 History 19
2.2.3 Classification of composites 20
2.3 Nanocomposite materials 22
2.3.1 Definition and overview 22
2.3.2 Physical structure of nanofillers 23
2.3.3 Nanocomposite classification 24
2.4 Carbon nanotubes (CNTs) 25
2.4.1 Mechanical properties of carbon nanotubes 28
2.5 Carbon nanotube reinforced composite 30
2.5.1 Processing techniques 30
2.5.2 Potential and current challenges 30
2.6 Carbon nanotube reinforced composite plates 31
2.6.1 Mechanical properties of CNTRC plate 33
2.7 Conclusion 35
CHAPTER 3 EXTENDED FINITE ELEMENT METHOD 36
3.1 Introduction 36
3.2 Extended finite element method 36
3.3 Crack modeling using discontinuities enrichment 37
3.4 Selection of enriched nodes 41
3.5 Numerical integration 42
3.6 Discretization 44
3.7 Application to the vibration analysis of cracked plates 46
3.7.1 Displacement field 47
3.7.2 Strain field 48
3.7.3 XFEM formulation 49
3.7.4 Equation of motion 54
3.8 Conclusion 58
CHAPTER 4 FREE VIBRATION ANALYSIS OF CRACKED COMPOSITE PLATE REINFORCED WITH CNT's USING XFEM 59

4.1 Introduction 59
4.2 Isotropic homogenous plate 60
4.3 Orthotropic plate 61
4.3.1 Virgin CNTRC plate 62
4.3.2 FG-CNTRC cracked plate 63
4.4 Parameter study 66
4.4.1 Effect of crack length 66
4.4.2 Effect of crack position 67
4.4.3 Effect of the power law index *Pin* 71
4.5 CNTRC vs Carbon/epoxy plates 72
4.6 Conclusion 74
CHAPTER 5 EFFECT OF CNT REINFORCEMENT ON THE FREE VIBRATION BEHAVIOR OF CRACKED MULTILAYER LAMINATED COMPOSITE 75
5.1 Introduction 75
5.2 Comparative study 77
5.3 Free vibration of cracked laminated CNTRC plates 80
5.3.1 Effect of CNT volume fraction and plate Width/thick ratio 87
5.3.2 Effect of power law-index 91
5.4 Conclusion 93
Conclusion…. 94
REFRENCES 96

LIST OF FIGURES

Figure 2.1: Simple definition of composite 19

Figure 2.2 : Classification of nanofiller (a) zero-dimensional, (b) one-dimensional, (c) two-dimensional, (d) three-dimensional (nano-meter sized of fillers which are less than 100 nm) [68]. 24

Figure 2.3 : The purple structure is a human hair fragment, with a diameter of about 80 to 100 thousand nanometers and in the background is a network of single-walled carbon nanotubes [74]. 26

Figure 2.4: Schematic view of carbon nanotubes single walled carbon nanotube (SWCNT) and multi-walled carbon nanotube (MWCNT) [75] 27

Figure 2.5: Schematic representation of how graphene sheets can be rolled up to form nanotubes [76]. 28

Figure 2.6: Yakobson's Simulation of SWNT Deformation 29

Figure 2.7 : Geometric parameters of FG-CNTRC plate and typical distribution patterns. 32

Figure 3.1: Finite element mesh of discontinuous enrichment 39

Figure 3.2: Crack not aligned with the mesh, circled nodes use a discontinuous function for enrichment, while squared nodes use tip enrichment functions 40

Figure 3.3: Local polar coordinates at the crack tips 41

Figure 3.4: An arbitrary crack placed on a mesh, the jump function in this case (H(x)=-1) 41

Figure 3.5: Enriched node I in the support region R_I 42

Figure 3.6: Heaviside and Asymptotic Enrichment for arbitrary Crack 42

Figure 3.7: (a) Nodes located within the region affected by the crack. 43

Figure 3.8: Partitioning of a four nodes elements 43

Figure 3.9: Discretization of a 10x10 mesh of a cracked plate. 44

Figure 3.10: (a): A mesh zone with a discontinuous element 45

Figure 3.11: Geometry of a cracked rectangular plate and its associated deformations 48

Figure 3.12: Transformation of the reference frame within a ply 51

Figure 4.1: Geometry and sign convention 66
Figure 4.2: CFCF plate with crack: varying x-axis position 68
Figure 5.1: Laminated Composite Plate with Functionally Graded Carbon Nanotubes (FG-CNTs) 76
Figure 5.2: Examples of Stacking Sequences in Laminated Composite Plates: (a) Cross-ply (0°/90°), (b) Angle-ply (45°/-45°) 76
Figure 5.3: Effect of Crack Length on Fundamental Frequency in Cross-Ply (0°/90°) Laminate plate with different fiber volume fraction and plate configuration 88
Figure 5.4: Effect of Crack Length on Fundamental Frequency in Angle-Ply (45°/-45°) Laminate plate with different fiber volume fraction and plate configuration 89
Figure 5.5: Effect of Crack Length on Fundamental Frequencies of SSSS Cross-Ply (0°/90°) Laminated square plate with different width to thick ratio. 90

LIST OF TABLES

Table 2.1: Mechanical Properties of Polymer Matrices [65] 21

Table 2.2: Mechanical Properties of Reinforcement Fibers [65] 22

Table 4.1: Boundary conditions combination 59

Table 4.2: Convergence of the first five Natural Frequencies with Mesh Refinement **Error! Bookmark not defined.**

Table 4.3: Non-dimensional first five natural frequencies $\bar{\omega} = \omega\sqrt{\rho h / D}$, $D = \frac{Eh^3}{12(1-\upsilon^2)}$ of isotropic plate 61

Table 4.4: Non-dimensional first five natural frequencies $\left(\bar{\omega} = \omega(L^2/h)\sqrt{\rho_m / E_m}\right)$ of SSSS CNTRC plate with different values of nanofiller volume fraction 62

Table 4.5: Non-dimensional first five natural frequencies $\bar{\omega} = \omega(W^2/h)\sqrt{\rho_m / E_m}$ of CNTRC plate 63

Table 4.6: Non- dimensional first five natural frequencies with different length of the crack and different boundary conditions 65

Table 4.7: Non-dimensional natural frequencies of CNTRC plate with different distribution patterns, different lengths of crack and different boundary conditions 67

Table 4.8 : Non-dimensional first five natural frequencies of CFCF cracked CNTRC plate with various crack positions along x-axis and (L/h) ratios. 69

Table 4.9 : Non dimensional first five natural frequencies of cracked CNTRC plate with various crack positions along y-axis and different boundary conditions. 70

Table 4.10: Non-dimensional first five natural frequencies of CFCF cracked CNTRC plate with various power law index 72

Table 4.11: First Natural frequencies for different volume fraction of Carbon/epoxy plate. 73

Table 5.1: Effect of CNT Volume Fraction f_{CNT}^{*} on CNT Efficiency Parameter in Laminated Composite Plates. 77

Table 5.2: Comparisons of the first six non-dimensional frequencies of cross ply (0°/90°/0°/90°/0°) laminated CNTRC plates with two types of boundary conditions 78

Table 5.3: Comparison of non-dimensional frequencies of cross-ply $(0°/90°)_n$ and angle ply $(45°/-45°)_n$ laminated SSSS CNTRC plates with different number of layers for $L/W = 1$, $W/h = 50$, $N_L = 20$ and $f^*_{CNT} = 0.11$ 79

Table 5.4: Comparison of first six non-dimensional frequencies of SSSS cross-ply (0°/90°) CNTRC laminated composite plates with various plate configuration 80

Table 5.5: The first five non-dimensional frequencies of cross ply (0°/90°/0°/90°/0°) laminate CNTRC plates with two types of boundary conditions and various length of the crack. 81

Table 5.6: Fundamental Non-dimensional frequencies of cross-ply $(0°/90°)_n$ and angle ply $(45°/-45°)_n$ laminated CFCF CNTRC plates with different number of plies and various crack length**.** 82

Table 5.7: Fundamental Non-dimensional frequencies of cross-ply $(0°/90°)_n$ and angle ply $(45°/-45°)_n$ laminated SSSS CNTRC plates with different number of plies and various crack length. 83

Table 5.8: Fundamental Non-dimensional frequencies of cross-ply $(0°/90°/0°)_s$ and angle ply $(45°/-45°/45°)_s$ laminated SSSS CNTRC plates with different number of plies and various crack length. 84

Table 5.9: Fundamental non-dimensional frequencies of cross-ply (0°/90°) CNTRC laminated composite plates with various plate configuration and various crack 85

Table 5.10: Fundamental non-dimensional frequency of angle-ply (45°/-45°) CNTRC laminated composite plates with various plate configuration and various crack. 86

Table 5.11: Fundamental non-dimensional frequencies of cross-ply (0°/90°) and angle- ply (45°/-45°) laminated CNTRC plates with various values of power-law index P_{in}, plate configuration and crack length (CFCF, $L/W = 1$, $f^*_{CNT} = 0.11$ and $W/h = 50$**)** 92

LIST OF SYMBOLS

E_{11}^{CNT}	: Longitudinal elastic modulus of CNTs	(GPa)
E_{22}^{CNT}	: Transverse elastic modulus of CNTs	(GPa)
G_{21}^{CNT}	: Shear modulus of CNTs	(GPa)
E_m	: Elastic modulus of the matrix	(GPa)
G_m	: Shear modulus of the matrix	(GPa)
$f_{CNT}^{(k)}$	: Volume fraction of nanofillers	
f_{CNT}^{*}	: Total volume fraction of the CNTs	
P_{in}	: Power law index	
W_{CNT}	: Weight fraction of the CNTs	
ρ_{CNT}	: Mass density of the CNTs	(Kg/m^3)
ρ_m	: Mass density of the matrix	(Kg/m^3)
N_L	: Number of layers	
η_j	: CNT reinforced composite efficiency parameters	
υ_{12}^{CNT}	: Poisson ratio of CNTs	
υ_m	: Poisson ratio of the matrix	
Δ	: Displacement approximation	
N	: Shape function	
δ	: Nodal displacement	
$H(x)$	: Heaviside function	
$F_l(x)$	: Asymptotic functions	
u	: Displacement of the plate with x direction	
v	: Displacement of the plate with y direction	
w	: Bending of the plate in z direction	
θ_x	: Rotation around *x axis*	

θ_y	: Rotation around *y axis*	
$[\varepsilon]$	: Strain field	
σ	: Normal stress	(GPa)
τ	: Shear stress	(GPa)
ε	: Normal strain	
γ	: Shear strain	
Q	: Elastic constants	
$[\bar{Q}]$	: Stiffness matrix	
$[J]$	: Jacobean matrix	
θ	: Fiber orientation	
$N\ (x, y)$	: Membrane stress resultant	
$M\ (x, y)$	: Bending and twisting moment	
$Q\ (x, y)$	: Shear stress resultants	
$[A]$	: Extension matrix	
$[B]$	: Coupling matrix	
$[D]$	: Bending matrix	
$[F]$	: Shear matrix	
V	: Total potential energy	(Joule)
T	: Kinetic energy	(Joule)
$[\bar{m}]$	: Inertia matrix	
[M]	: Global mass matrix	
[K]	: Global stiffness matrix	
ω	: Natural frequency	(rad/s)
$\bar{\omega}$	: Non dimensional natural frequency	
L	: Length of the plate	(m)
W	: Width of the plate	(m)
H	: Thickness of the plate	(m)

LIST OF ABREVIATIONS

NDT	: Non Destructive Testing
BEM	: Boundary Element Method
CZM	: Cohesive Zone Models
FEA	: Finite Element Analysis
XFEM	: Extended Finite Element Method
CNT, CNTs	: Carbon Nanotube, Carbon Nanotubes.
CNTRC	: Carbon nanotubes Reinforced Composite Plate.
FRP	: Fiber Reinforced Polymers
PMNC	: Polymer Matrix Nanocomposites
CMNC	: Ceramic Matrix Nanocomposites
MMNC	: Metal Matrix Nanocomposites
TEM	: Transmission Electron Microscopy
UD	: Uniform Distribution.
FG-X	: X Functionally Graded configuration.
FG-O	: O Functionally Graded configuration.
FG-A	: A Functionally Graded configuration.
FG-V	: V Functionally Graded configuration.
SWCNTs	: Single-Walled Carbon Nanotubes.
DWCNTs	: Double-Walled Carbon Nanotubes.
MWCNTs	: Multi-Walled Carbon Nanotubes.
FG-CNTRC	: Functionally Graded Carbon Nanotubes Reinforced Composite Plate.
FSDT	: First order Shear Deformation Theory.
HSDT	: High order Shear Deformation Theory.
SSSS	: Simply Supported plate on their four edges.
CCCC	: Clamped plate on their four edges.
CFCF	: Clamped plate on two edges and free on the other edges

GENERAL INTRODUCTION

Over the past decades, composite materials have become essential in numerous advanced engineering fields such as aerospace, aeronautics, automotive engineering, civil infrastructures, and biomedical devices. Their widespread use is mainly due to the unique combination of low weight, high stiffness, and excellent mechanical performance they offer. A composite material consists of two main phases: a matrix typically polymer, metal, or ceramic which ensures cohesion, and a reinforcement such as continuous fibers, short fibers, or particulates that provides mechanical strength and stiffness. The resulting synergy allows for the design of structures with properties superior to those of conventional homogeneous materials. Among the most common composites are fiber-reinforced polymers (FRPs), particularly glass- and carbon-fiber composites, which are valued for their strength-to-weight ratio, durability, and design versatility.

Despite their advantages, traditional composites present some limitations, especially regarding damage resistance, crack propagation, and dynamic performance in harsh environments. As industries move toward lighter, safer, and more efficient structures, the need for materials with enhanced multifunctional properties has become increasingly critical. This demand has led to the development of nanocomposites, a new class of materials in which nanometer-scale reinforcements such as metallic nanoparticles, clay platelets, carbon nanofibers, or carbon nanotubes (CNTs) are dispersed within the matrix. These nano reinforcements significantly enhance the mechanical, thermal, and electrical properties of the base material.

Among all nano reinforcements, carbon nanotubes (CNTs) stand out due to their exceptional mechanical and physical characteristics, including extremely high tensile strength, a Young's modulus several times greater than that of steel, remarkable thermal conductivity, and low density. When incorporated into a polymer matrix, CNTs can produce nanocomposite plates with superior stiffness, improved damping behavior, and enhanced structural integrity. In addition, the possibility of tailoring the distribution of CNTs across the plate thickness uniformly (UD) or functionally graded in patterns such as FG-X, FG-V, FG-O, FG-A offers additional flexibility for optimizing local mechanical properties and improving performance under dynamic loading.

Despite these advantages, nanocomposite structures remain vulnerable to one of the most critical forms of structural degradation: cracking. Cracks may originate during manufacturing, arise from mechanical or thermal loading, or develop gradually due to fatigue or environmental effects. The presence of a crack significantly alters the stiffness distribution of the structure, affects stress concentration zones, and can lead to progressive failure if not properly assessed. In plates made of composite or nanocomposite materials, a crack produces strong local discontinuities that directly influence bending behavior, buckling resistance, and more importantly, vibrational response.

Vibration analysis plays a crucial role in the design and health monitoring of engineering structures. When a structure is subjected to cyclic or periodic excitations, it may exhibit resonance if the excitation frequency matches one of its natural frequencies. Resonance can induce large deformations and high stress levels, ultimately resulting in catastrophic failure. Therefore, accurately determining the natural frequencies of a structure and understanding how these frequencies are influenced by cracks, material gradation, geometric parameters, and boundary conditions is essential to ensuring structural safety and reliability.

The analysis of cracked plates requires accurate modeling of displacement discontinuities and stress singularities near the crack tip. Traditional finite element methods (FEM) require a mesh that conforms to the crack geometry, which becomes complex and computationally expensive, especially when the crack changes position, orientation, or length. To overcome these limitations, the Extended Finite Element Method (XFEM) has emerged as a powerful numerical tool for modeling cracked structures. XFEM enriches the displacement field with additional functions such as the Heaviside function for capturing displacement jumps across the crack surface and asymptotic crack-tip functions for representing stress singularities. These enrichments allow cracks to be represented independently of the underlying mesh, eliminating the need for remeshing and enabling efficient simulation of complex crack configurations. XFEM has therefore proven to be an effective and robust approach for modeling fracture problems in composite and nanocomposite plates.

In the context of nanocomposite plates reinforced with CNTs, the use of XFEM offers significant advantages:

- it accurately captures crack-induced reductions in stiffness;

- it models discontinuities without modifying the mesh;
- it allows parametric studies involving changes in crack geometry;
- and it provides high accuracy in predicting natural frequencies for cracked structures.

Given these advantages, XFEM represents a key numerical strategy for investigating the dynamic behavior of cracked nanocomposite plates reinforced with functionally graded CNT distributions.

The main objective of this thesis is to investigate the free vibration behavior of cracked nanocomposite plates using the Extended Finite Element Method (XFEM). The study focuses particularly on understanding how various factors influence the dynamic response of such structures, including the distribution patterns of carbon nanotubes (CNTs), the effects of crack length, location, and orientation, geometric variations and aspect ratios, as well as the influence of CNT volume fraction and the power-law index. In the case of multi-layered structures, special attention is given to the impact of different stacking sequences and the various configurations of nanofillers within the plies. The research is organized around two main categories of structures: single-layer nanocomposite plates, in which CNTs are distributed according to different functional grading patterns, and laminated composite plates, where each ply may incorporate a distinct CNT distribution, resulting in a more complex and realistic representation of structural behavior. The methodology adopted throughout this work includes modeling the effective material properties of CNT-reinforced nanocomposites using extended micromechanical approaches such as the rule of mixtures and Halpin–Tsai relations, formulating the displacement and strain fields based on first-order shear deformation theory, and introducing crack-related enrichment functions within the XFEM framework to accurately capture displacement discontinuities. The global stiffness and mass matrices are then constructed, and the resulting eigenvalue problem is solved to determine the natural frequencies of the cracked nanocomposite plates

This research on the dynamic behavior of cracked nanocomposite plates is structured into five chapters: Chapter 1 provides a comprehensive literature review highlighting the research gap in nanocomposite plate vibration analysis. Chapter 2 details the material properties of nanocomposites, particularly carbon nanotubes, and characterizes the geometric and

mechanical properties of the composite plate. Chapter 3 elaborates on the Extended Finite Element Method (XFEM) used for modeling cracks via discontinuity enrichment, presenting the displacement and strain fields and the formulation of the stiffness and mass matrices. Chapter 4 presents a free vibration analysis of CNT-reinforced composite cracked plates using a developed MATLAB program validated through comparison with pervious researches. This chapter analyzes the impact of various CNT distribution patterns, crack parameters, plate dimensions, CNT volume fraction, and power law index on natural frequencies under different boundary conditions. Chapter 5 extends the investigation to the free vibration analysis of cracked laminated composite plates, considering n number of plies. This chapter focuses on the effect of different stacking sequences and various configurations of nanofillers within the plies on the free vibration analysis of the cracked composite plate.

CHAPTER 1

LITERATURE REVIEW

1.1 Introduction

Cracking, in its various forms, represents a fundamental mode of failure across diverse engineering applications. Current research emphasizes the complex interplay of factors leading to crack initiation and propagation. For instance, fatigue cracking, driven by cyclic loading, remains a critical concern**.** A foundational study by Suresh and Ritchie [1] in 1984 revealed that small fatigue cracks exhibit distinct growth behavior compared to long cracks, influenced by mechanical, metallurgical, and environmental factors. Ongoing advancements in modeling and prediction aimed at enhancing structural durability [2]. Recent studies [3]–[7] have highlighted the significance of micro-crack formation and coalescence in the early stages of fatigue damage, pushing the boundaries of detection and analysis. Stress corrosion cracking, another significant failure mechanism, reveals the critical influence of environmental factors on material performance, driving the development of corrosion-resistant alloys and advanced protective coatings [8]. Furthermore, the application of fracture mechanics, particularly in the context of advanced materials, continues to evolve, providing increasingly accurate predictions of crack growth and critical failure loads. It's crucial to acknowledge the diverse typology of cracks, including structural versus non-structural, and classifications based on cause like shrinkage, thermal, and fatigue cracks. Understanding the orientation, such as vertical, horizontal, or diagonal, is also vital. The state of the art also reflects a growing emphasis on non-destructive testing (NDT) techniques, such as ultrasonic testing and digital image correlation, for early crack detection and monitoring, enabling proactive maintenance and extending the lifespan of critical components [9]–[11]. These advanced techniques are increasingly capable of differentiating between active and dormant cracks, and even detecting subtle crazing, providing a more comprehensive understanding of material degradation.

1.2 Numerical modeling of cracks

Accurate simulation of crack initiation, propagation, and failure requires two complementary components: fracture models, which describe the mechanical behavior of the material near the crack, and numerical methods, which provide the computational framework for solving the governing equations.

1.2.1 Fracture modeling approach

1.2.1.1 Cohesive Zone Models (CZM)

CZMs define fracture behavior through cohesive elements or surfaces placed along potential crack paths. They simulate the gradual separation of material surfaces, accounting for the energy dissipation during fracture. CZMs are applicable when modeling ductile fracture or delamination in composite materials [12]–[14].

1.2.2 Numerical methods for crack simulation

1.2.2.1 Boundary Element Methods (BEM)

BEM discretizes only the boundaries of the domain into elements. It's particularly applicable when dealing with problems involving infinite or semi-infinite domains, such as crack analysis in large structures where the far-field behavior is crucial. It excels in problems where the solution is known in the domain but not on the boundary [15]–[17].

1.2.2.2 Finite Element Analysis (FEA)

A traditional mesh-based method, FEA discretizes the entire domain into elements. It has demonstrated its efficiency in solving many solid mechanics problems, but it is less adapted for successive crack propagation analyses. This is because FEA requires a mesh where element boundaries conform to the domain's boundaries. As crack growth changes internal boundaries, remeshing is needed at each step, making it computationally expensive, especially for complex 3D cracks. Thus, alternative numerical methods are often preferred for crack propagation analyses.

1.2.2.3 Meshless methods

Meshless methods are a diverse collection of numerical techniques that, unlike finite element methods, operate without a fixed mesh, using scattered nodes to represent geometry.

This flexibility allows for easier modeling of complex shapes and moving boundaries, like cracks, and encompasses various approaches such as EFG and SPH [18]–[20]. While offering potential for higher accuracy and adaptive capabilities, meshless methods often present challenges due to their complexity, computational cost, and difficulties in handling certain boundary conditions and geometries.

1.2.2.4 Extended Finite Element Method (XFEM)

An enhancement of FEA, XFEM enriches the standard finite element approximation to allow for discontinuities, like cracks, to be represented independently of the mesh. This eliminates the need for remeshing during crack propagation, making it particularly well-suited for simulating crack growth along arbitrary paths.

Extended Finite Element Method is like a supercharged version of the regular FEM. It keeps all the good things about FEM but adds some powerful new tricks. Two main advantages are: first, it can accurately show the intense stress around a crack tip. Second, it can simulate multiple cracks growing in any direction without needing to redraw the mesh. Basically, you don't have to draw the crack directly into the model's shape. Instead, XFEM uses special math formulas to represent the crack's effect on stress and displacement. These formulas are based on the known behavior of cracks, allowing the software to accurately simulate them.

1.2.2.5 A review of XFEM development

Belytschko and Black [21] pioneered XFEM, introducing a method to simulate crack growth with minimal remeshing. They enhanced standard finite element approximations by adding functions that represent the crack's discontinuity. Remeshing was only necessary for highly curved cracks to refine the accuracy of the solution. The term XFEM was introduced by Moës et al [22], who advanced the method to enable mesh-independent crack representation using enriched approximations. Dolbow et al [23]–[25] significantly advanced XFEM by applying it to 2D elasticity and Mindlin-Reissner plates, utilizing both jump functions and near-tip asymptotic fields. They also developed a partition of unity-based enrichment technique to model arbitrary discontinuities within the finite element framework. Daux et al [26] expanded XFEM to handle complex crack scenarios, including branched, intersecting, and cracks originating from holes. Sukumar et al [27] first applied XFEM to three-dimensional crack modeling. Later advancements focused on specific applications: Areias and Belytschko [28]

and Areias et al [29] created new XFEM formulations for crack propagation in shells, incorporating rotational enrichments. Additionally, Bayesteh and Mohammadi [30] investigated the influence of different crack tip enrichment terms on crack behavior in plates and pressurized shells. To handle cracks growing in any direction with XFEM, tracking the moving crack boundaries became necessary. The level set method (LSM) emerged as the preferred way to define the crack path and tip locations. Stolarska et al [31] first combined LSM with XFEM to simulate crack growth. Building on this, Belytschko et al [32] developed a method using signed distance functions (level sets) to represent discontinuities and their derivatives, allowing for accurate updates of crack positions. Building on its early success, XFEM has been widely used in engineering. Notably, research [33]–[35] has investigated cohesive crack behavior using this method. Mariani and Perego [36] utilized XFEM to simulate cohesive crack growth, employing a cubic displacement discontinuity to accurately model the process zone at the crack tip. Areias and Belytschko [28] further developed XFEM by integrating a viscosity-regularized continuum damage model, creating a 'crack-band' version. Researchers have extensively studied XFEM's accuracy, stability, and convergence. Laborde et al [37] examined the convergence of various XFEM models on cracked domains. Peters and Hack [38] addressed the issue of singular stiffness matrices by proposing methods to eliminate certain enhanced degrees of freedom. Bechet et al [39] introduced a geometrical enrichment approach, where enrichment is based on domain size rather than element-crack front contact. Ventura [40] demonstrated that standard Gauss quadrature can be effectively used in elements containing discontinuities without the need for element subdivision or additional approximations. To enhance the accuracy of XFEM crack-tip fields, Xiao and Karihaloo [41] explored the application of higher-order quadrature and statically admissible stress recovery procedures.

1.3 Failure mechanisms in composite materials

Composite materials, engineered by combining two or more distinct constituents to achieve enhanced properties, have become indispensable in numerous engineering applications due to their high strength-to-weight ratio, corrosion resistance, and design flexibility. However, despite these excellent characteristics, composites suffer from a number of inherent shortcomings that can compromise their structural integrity. These include brittleness, elevated

thermal and residual stresses, weak interfacial bonding, and low toughness, which collectively predispose composites to unstable cracking. Manufacturing imperfections, fatigue, yielding, and other operational stresses can exacerbate these vulnerabilities, leading to substantial damage characterized by reduced stiffness, diminished load-bearing capacity, and increased risk of catastrophic failure. This problem is particularly critical in applications involving concentrated dynamic loads, such as those encountered in high-velocity impacts or explosions.

Furthermore, the prevalent use of thin composite structures renders them highly sensitive to defects. Cracking, a common defect, can initiate and propagate due to production flaws or in-service stresses, necessitating a thorough understanding of crack stability and load-bearing capacity. Consequently, the computational mechanics community has increasingly focused on analyzing these phenomena, given their direct impact on safety and economic efficiency across various industries.

The complex layered, orthotropic, and often inhomogeneous nature of composite materials allows for a wide range of failure modes. These modes can be broadly categorized into fiber failure, ply delamination, matrix cracking, and fiber/matrix debonding. Critically, these failure modes, whether occurring individually or in combination, can severely degrade or entirely eliminate the composite action, thereby significantly impacting the material's performance.

1.3.1 Matrix cracking

In composite materials, the matrix typically represents the weakest link under applied loads. Its inherent brittleness makes it highly susceptible to cracking, which often serves as the primary failure initiation point. These initial matrix cracks can then propagate and trigger more severe failure modes, such as delamination and interfacial debonding, ultimately compromising the structural integrity of the composite.

1.3.2 Delamination

Delamination, or interlaminar cracking, is a prevalent failure mode in composite laminates, significantly compromising their ductility, stiffness, and strength, and potentially leading to abrupt brittle fracture. This damage can originate and propagate from stress concentrations induced by manufacturing, transportation, operational conditions (temperature, moisture, shrinkage), and especially sudden, concentrated loads like impacts or explosions. These effects

are amplified at geometric discontinuities such as curves, abrupt cross-sectional changes, and free edges. Critically, delamination can cause extensive internal damage between plies without any visible external signs, posing a significant safety concern.

1.3.3 Fiber/Matrix Debonding

Strong fiber-matrix bonding is crucial for composite integrity. Debonding or sliding weakens the material significantly. Ideally, the composite should be designed so that fiber/matrix debonding occurs only after matrix cracking and delamination initiate.

1.3.4 Fiber breakage

Fiber breakage signifies the near-final stage of composite failure, immediately preceding structural collapse. Upon fiber rupture, the material's load-bearing capacity experiences an abrupt and drastic reduction, effectively rendering it useless.

1.4 Nanoscale-dependent failure mechanism

While nanocomposites share failure mechanisms like matrix cracking and delamination with traditional composites, it's crucial to recognize that with their unique blend of nanoscale reinforcements within a matrix, exhibit complex failure mechanisms that differ significantly from traditional composite materials. These mechanisms are influenced by factors such as the type, size, dispersion, and interfacial adhesion of the nanoparticles, as well as the properties of the matrix material itself. Here are some of the key failure mechanisms observed in nanocomposite materials [42]:

1.4.1 Fracture

1.4.1.1 Brittle fracture

Similar to ceramics or some polymers, nanocomposites can fail suddenly with little or no plastic deformation. This is often associated with poor dispersion of nanoparticles leading to stress concentration points or weak interfacial bonding that allows cracks to propagate easily [43].

1.4.1.2 Ductile fracture

In contrast, some nanocomposites, particularly those with well-dispersed nanoparticles and strong interfacial adhesion, can exhibit more ductile behavior. Failure occurs after significant plastic deformation, often involving void nucleation, growth, and coalescence. Nanoparticles can hinder the movement of dislocations in the matrix, increasing strength but potentially reducing ductility if not properly controlled [44].

1.4.1.3 Fatigue fracture

Under cyclic loading, nanocomposites can fail due to fatigue [45]. Crack initiation and propagation occur over time at stress levels lower than the static strength. Nanoparticles can influence fatigue behavior by affecting crack initiation sites, crack growth rates, and crack closure mechanisms [46]. Well-dispersed nanoparticles and strong interfaces can improve fatigue resistance by deflecting or bridging cracks[47].

1.4.2 Interfacial failure

The interface between the nanoparticles and the matrix plays a critical role in the overall performance and failure of nanocomposites [48]. Weak interfaces can lead to several failure modes:

1.4.2.1 Debonding

Applied stress can cause the nanoparticles to detach from the matrix. This debonding can initiate cracks, reduce the effective reinforcement, and lower the overall strength and stiffness of the composite.

1.4.2.2 Pull out

In the case of high aspect ratio nanoparticles like nanotubes or nanofibers, failure can occur by the nanoparticles being pulled out of the matrix [42]. The energy dissipated during pull-out contributes to the fracture toughness of the material [49]. Stronger interfacial bonding can lead to nanoparticle fracture instead of pull-out, potentially increasing the energy absorption.

1.4.2.3 Interfacial cracking

Cracks can initiate and propagate along the interface between the nanoparticles and the matrix due to stress concentrations or thermal mismatches. This can lead to delamination and a loss of structural integrity.

1.4.3 Other failure mechanism:

1.4.3.1 Agglomeration

Poor dispersion of nanoparticles can lead to the formation of agglomerates, which act as stress concentration points and can initiate premature failure [50].

1.4.3.2 Fluid and thermal Aging

Environmental factors like moisture, chemical exposure, and temperature variations can degrade the matrix or the interface over time, leading to a reduction in mechanical properties and eventual failure [51].

1.5 Vibration of cracked composite plates

understanding of natural vibration frequencies is crucial in the design of composite plates. Composites, with their tailored material properties and complex layered structures, exhibit specific vibrational behaviors. During operation, if an external excitation frequency coincides with one of the plate's natural frequencies, it can lead to resonance, resulting in excessive and potentially damaging vibrations. Therefore, engineers strategically select materials, stacking sequences, and geometric parameters to ensure that the natural frequencies of the composite plate are sufficiently far from expected operational excitation frequencies. This proactive approach minimizes unwanted vibrations, enhances the structural integrity and longevity of the composite component, and contributes to quieter and more efficient systems.

Mohanty [52], investigates the vibrational behavior of cracked composite plates, a critical aspect in preventing resonance-induced structural damage. Experimental modal analysis was conducted on fabricated composite plates with varying crack depths, lengths, and orientations. The study identified significant reductions in natural frequencies with the introduction and growth of cracks. Boundary conditions also played a crucial role, with fully free (FFFF) plates exhibiting the highest frequencies. Furthermore, crack orientation was found to influence vibrational characteristics, with a maximum frequency observed at a 45-degree angle.

Research focused on the analytical modeling of cracks in aerospace structures, motivated by the need for improved damage detection methodologies [53]. This work generated a reduced-order analytical model to describe the vibration of a cracked plate panel subjected to external forces. The derived Duffing equation incorporated parameters related to the plate's geometry,

mass, loading, boundary conditions, and crack properties. The study obtained an approximate analytical solution. The findings indicated that the model could handle different boundary conditions and that crack geometry significantly influenced the plate's natural frequencies. Numerical investigations explored the changes in behavior of the cracked plate.

Research by Bachene et al [54], investigated the dynamic behavior of defective laminated composite plates using XFEM, considering shear deformation and rotary inertia. The study analyzed the impact of crack size and location on plate frequencies, finding that frequencies decrease with increasing crack length, particularly for certain modes. Impact analysis also revealed a critical crack length affecting the plate's rigidity.

Extensive prior research, as evidenced by the studies mentioned earlier, has significantly focused on the free vibration analysis of cracked composite plates. However, a notable gap exists in the specific investigation of cracked nanocomposite plates. While works such as Negi et al. [55], [56] have employed XFEM with the Heaviside step function and enrichment functions to analyze crack growth in Carbon Nanotube Reinforced Composites (CNTRC), and Taheri and Memarzadeh [57] , have utilized a similar approach to explore the buckling behavior of cracked CNTRC plates under shear loading. demonstrating the significant impact of cracking on their structural capacity, no prior work, to the best of our knowledge, has specifically addressed the free vibration analysis of cracked nanocomposite plates. This constitutes the initial focus and novelty of the present study. Furthermore, this work extends the investigation to an even more complex scenario by specifically addressing the free vibration analysis of cracked laminated nanocomposite plates (where "laminated" refers to the stacking of multiple layers with potentially different fiber orientations and configurations), representing a further significant contribution to the field.

1.6 Laminated CNT reinforced composite plate

1.6.1 Definition of a Laminated Plate

A laminated plate is a composite material engineered by bonding together two or more thin layers (plies) of reinforcing materials embedded in a matrix. These plies are stacked and adhered, and each can be composed of the same or different materials with varying orientations

of the reinforcing fibers. This layered structure enables the tailoring of the plate's overall mechanical properties.

1.6.2 The Advantage of Customizable Material Properties

Laminated composites offer a significant advantage: the ability to customize their material properties. This customization is achieved through two primary design parameters:

- Strategic Stacking of CNTRC Layers: The order and orientation of individual plies significantly influence the laminate's overall behavior.
- Controlled Nanofiller Distribution within Each Ply: By manipulating the concentration and arrangement of CNTs within each layer, the local material properties can be precisely controlled.

This dual-level design control unlocks the potential for optimizing a wide range of desired characteristics in the composite plate.

1.6.3 Stacking Sequences

The stacking sequence refers to the specific order and fiber orientation of the individual plies within the laminate. The notation used to describe this sequence reads from the bottom layer upwards, with fiber orientations indicated in degrees within square brackets, separated by slashes (e.g., [0°/45°/-45°/90°]). Key concepts and common types of stacking sequences include:

- Ply Orientation: The angle at which the reinforcing fibers in each ply are oriented relative to a reference axis.
- Stacking Sequence Notation: A shorthand method for representing the order and orientation of plies.
- Symmetry: A laminate where the stacking sequence below the mid-plane mirrors that above it, often denoted with a subscript 'S' (e.g., $[0°/45°/90°]_S$). Symmetry helps prevent coupling effects.

- Balance: A laminate containing pairs of plies with equal material and thickness but opposite fiber angles (e.g., [45°/-45°/0°/90°]), which minimizes in-plane shear-extension coupling.
- Repeat Stacking: Using subscripts to indicate the repetition of a ply group (e.g., $[0°/90°]_3$).

1.6.3.1 Common Stacking Sequence Types:

- Unidirectional [0°/0°/0°...]: Fibers aligned in one direction for high stiffness and strength in that direction.
- Cross-Ply [0°/90°/0°/90°...]: Alternating 0° and 90° plies for more balanced in-plane stiffness.
- Angle-Ply [θ/-θ/θ/-θ...]: Alternating positive and negative angles for good shear resistance.
- Quasi-Isotropic $[0°/\pm60°]_S$ or $[0°/\pm45°/90°]_S$: Designed for near-equal in-plane stiffness in all directions.
- Hybrid Laminates: Combining plies of different materials for tailored properties.
- Functionally Graded Laminates (in terms of ply properties): Where the material composition or fiber orientation varies between the layers.

The stacking sequence is critical in determining the overall mechanical behavior of the laminated plate, influencing stiffness, strength, buckling resistance, vibration characteristics, and failure modes.

1.6.4 Fiber Configuration within Each Ply

Beyond the overall orientation of fibers in a ply, the fiber configuration refers to the distribution of the reinforcing phase (in this case, CNTs) within the matrix of an individual layer. This is particularly relevant in functionally graded (FG) plies, where the CNT concentration is intentionally varied across the ply's thickness. Common fiber configurations include:

- UD (Unidirectional): CNTs are aligned in a single direction with a uniform concentration throughout the ply.
- FG-X: The concentration of CNTs is highest at the top and bottom surfaces of the ply and lowest at the mid-plane, creating an "X" shaped distribution. This configuration can effectively enhance the bending stiffness of the laminate.
- FG-O: The concentration of CNTs is highest at the mid-plane of the ply and lowest at the top and bottom surfaces, forming an "O" shaped distribution.
- FG-A: The concentration of CNTs varies linearly (asymmetrically) from one surface of the ply to the other.
- FG-V: The concentration of CNTs follows a "V" shaped (or inverted "V") distribution across the ply thickness, with higher concentrations at one or both surfaces and a lower concentration in the middle.

The strategic selection of the fiber configuration within each ply, in conjunction with the overall stacking sequence, provides a powerful tool for achieving optimized performance characteristics in laminated CNT reinforced composite plates. This approach allows for a more precise control over the material property distribution at both the macro (stacking sequence) and micro (fiber configuration) levels, unlocking significant potential for optimizing desired characteristics. Several research endeavors have further explored the behavior and design of these advanced materials. For instance, studies have indicated that concentrating nanofillers near the top and bottom surfaces represents an optimal strategy for enhancing the stiffness of laminated structures, a finding corroborated by Chiker et al. [58] who employed a layer-wise functionally graded model to represent the CNT volume fraction across the plate thickness. Nguyen-Quang et al. [59] investigated the dynamic response of FG-CNT-reinforced composite laminated plates integrated with piezoelectric layers using a Higher-Order Shear Deformation Theory (HSDT). Bachiri et al.[60] developed a mathematical model based on a new higher shear deformation plate theory to analyze the thermo-elastic response of CNTRC cross-ply laminated plates under thermal loading. Tran et al. [61] focused on the static response of smart laminated CNTRC plates incorporating a piezoelectric layer, utilizing a new four-variable refined plate theory. Furthermore, Lei et al. [62] investigated the buckling behavior of

functionally graded CNT-reinforced composite laminated plates by combining the First-order Shear Deformation Theory (FSDT) with the meshless kp-Ritz method. These studies collectively highlight the diverse analytical and modeling approaches employed to understand and optimize the performance of laminated plates reinforced with CNTs under various loading conditions and configurations.

1.7 Conclusion

This chapter reviewed the major numerical approaches used to model and simulate cracks in engineering structures, with particular attention to recent advances in crack growth representation. Various numerical methods for crack simulation were discussed, highlighting the advantages of the Extended Finite Element Method (XFEM) and its continuous development. The failure mechanisms in composite and nanocomposite materials were examined to understand how cracks initiate and propagate in such complex media. A survey of vibration studies on cracked composite plates demonstrated the sensitivity of dynamic behavior to damage and material configuration. Finally, the literature on laminated composite plates revealed the significant influence of stacking sequence, material gradation, and reinforcement patterns on stiffness and vibrational performance. This review identifies the gaps that motivate the present investigation of cracked laminated CNT-reinforced composites using XFEM

CHAPTER 2
MATERIAL PROPERTIES AND BEHAVIOR

2.1 Introduction

This chapter provides a foundational overview of composite and nanocomposite materials, emphasizing their growing importance in modern engineering applications. It begins by defining composite materials, outlining their classifications, and highlighting their advantages compared to conventional materials. The discussion then transitions to nanocomposites, where the unique characteristics of nanoscale reinforcements particularly carbon nanotubes (CNTs) are introduced. Special attention is given to the exceptional mechanical and physical properties of CNTs, along with the various synthesis techniques used to produce them. Finally, the chapter presents an overview of CNT-reinforced composites, addressing key fabrication challenges, dispersion issues, alignment strategies, and characterization methods. Together, these elements establish the scientific background necessary for understanding the behavior and potential of CNT-enhanced composite structures studied in the subsequent chapters.

2.2 Introduction to Composite Materials

2.2.1 Definition

Advanced composite materials are created by embedding fibrous materials within a resin matrix. To optimize both stiffness and strength, these materials are often laminated with fibers oriented in alternating directions (Figure 2.1). These composites, characterized by their distinct physical and chemical properties, are bonded at the atomic and molecular level, exceeding a scale of 1 micrometer. They offer significant advantages, including high strength, stiffness, low density, and excellent electrical and corrosion resistance. These properties make them ideal for weight reduction in finished parts. The reinforcing phase, typically composed of fibers or particles of similar size in all directions [63], provides superior stiffness and strength compared to the matrix. Commonly referred to as Fiber-Reinforced Polymer (FRP) composites, these

materials combine a polymer matrix with synthetic or natural fibers to enhance structural integrity and prevent cracking or fracturing.

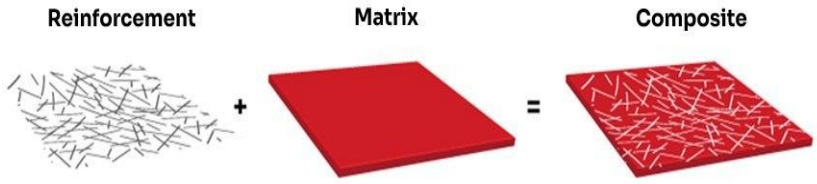

Figure 2.1 simple definition of composite

2.2.2 History

Early civilizations, such as the ancient Egyptians and Mesopotamians, demonstrated a basic understanding of composites. They combined mud and straw to create durable bricks for building construction, showcasing the concept of reinforcing a base material with an additive. This principle of combining materials with distinct properties to achieve superior performance has been a cornerstone of human innovation throughout history.

A significant leap occurred with the Mongol invention of the composite bow. This revolutionary weapon, crafted from a combination of wood, bone, animal glue, and birch bark, showcased the potential of combining diverse materials to achieve unparalleled strength and performance. The Mongol bow's accuracy and power provided a decisive military advantage, highlighting the strategic importance of composite materials in warfare and technology.

The modern era of composites began with the development of synthetic plastics in the early 20th century. These new materials, such as vinyl, polystyrene, and phenolic, offered superior properties to natural resins, opening doors to a wider range of applications. However, the true breakthrough came with the introduction of fiberglass in 1935. This lightweight yet incredibly strong material, created by combining glass fibers with a plastic polymer, laid the foundation for the Fiber Reinforced Polymers (FRP) industry, revolutionizing various sectors.

World War II accelerated the development and application of composites. The urgent need for lightweight and high-performance materials in aircraft and military equipment spurred innovation. Composites, with their unique combination of strength, stiffness, and lightweight properties, proved invaluable in these applications. The war also highlighted the versatility of composites, as they were found to be suitable for applications beyond aircraft, such as radar domes due to their radio frequency transparency.

Following the war, the focus shifted towards civilian applications. The marine industry quickly embraced composites, with the introduction of the first commercial boat hull in 1946. This marked the beginning of a broader adoption of composites in various sectors, including transportation, construction, and consumer goods.

The latter half of the 20th century witnessed significant advancements in composite materials. The development of high-performance fibers, such as Kevlar and carbon fiber, further expanded the possibilities of composites. These materials, with their exceptional strength-to-weight ratios, have found applications in diverse fields, from aerospace and defense to sports equipment and medical implants.

Today, the composites industry continues to evolve at a rapid pace. Ongoing research and development are focused on creating even stronger, lighter, and more sustainable composite materials. Advanced manufacturing techniques, such as 3D printing and nanotechnology, are being integrated to further enhance the performance and versatility of composites.

In conclusion, the history of composite materials is a testament to human ingenuity and our constant pursuit of materials with enhanced properties. From ancient building techniques to cutting-edge aerospace applications, composites have played a crucial role in shaping our world. As research and development continue to progress, we can expect even more innovative and transformative applications of composite materials in the years to come [64].

2.2.3 Classification of composites

Composite materials are engineered by combining two or more materials, typically a matrix and a reinforcement, to achieve enhanced properties. The matrix, the continuous phase, acts as a binder, holding the reinforcement together. While metals and ceramics can be used as matrices, polymers are the most common due to their cost-effectiveness, chemical resistance, and ease of processing. Polymers are categorized into thermosets, which are heat-resistant and chemically

stable, and thermoplastics, which are recyclable and shapeable. Table 2.1 presents the mechanical properties of polymers [65].

The reinforcement, the discontinuous phase, significantly improves the mechanical properties of the composite, such as strength, stiffness, and impact resistance. Synthetic fibers, including carbon, glass, and aramid, are widely used due to their high strength-to-weight ratio and tailored properties. Natural fibers, such as linen, sisal, and hemp, offer sustainability benefits and can be used in specific applications. Table 2.2 presents the mechanical properties of reinforcements [65].

Table 2.1: Mechanical Properties of Polymer Matrices [65]

Polymer	Volumetric Mass (g/cm^3)	Water Absorption after 24h (%)	Traction Resistance (MPa)	Young's Modulus (GPa)	Elongation at Break (%)	T_g (°C)	T_m (°C)
THERMOPLASTICS							
PP	0.90 - 0.92	0.01 - 0.02	26 - 41.4	0.9 - 1.8	15 - 700	-14	176
LDPE	0.91 - 0.93	<0.015	40 - 78	0.06 - 0.4	90 - 800	- 110	115
HDPE	0.94 - 0.96	0.01 - 0.2	14.5 - 38	0.4 - 1.5	2 - 130	-90	137
PS	1.04 - 1.06	0.03 - 0.1	25 - 69	4 - 5	1 - 2.5	100	239
PVC	1.38	0.1 - 0.3	53	3.0	-	87	212
PLA	1.24 - 1.25		72	2.11	10.7	60	180
THERMOSETS							
Polyester Resin	1.2 - 1.5	0.1 - 0.3	40 - 80	2 - 4.5	2	-	-
Epoxy Resin	1.1 - 1.4	0.1 - 0.4	35 - 100	3 - 6	1 - 6	-	-

Table 2.2: Mechanical Properties of Reinforcement Fibers [65]

Reinforcement	Origin	Volumetric Mass (g/cm^3)	Traction Resistance (MPa)	Young's Modulus (GPa)	Elongation at Break (%)
Carbon Fibre	PAN	1.8	3.53 - 7.06	230 - 540	0.7 - 2.0
Carbon Fibre	Petroleum	1.8	0.85 - 2.2	42 - 820	0.2 - 2.1
Glass Fibre E	Synthetic	2.53 - 2.55	1.5 - 3.7	72 - 76	2.5 - 4.9
Glass Fibre S	Synthetic	2.48 - 2.49	3.5 - 4.59	86 - 91	2.9 - 5.8
Aramid	Synthetic	1.38 - 1.47	2.75	70.5 - 112.4	2.4 - 3.6
Linen	Vegetable	1.5 - 3	0.2 - 0.77	13 - 55	1.8 - 8
Sisal	Vegetable	1.45	0.47 - 0.64	9.4 - 22	2 - 7
Hemp	Vegetable	1.47	0.31 - 0.90	30 - 70	1.6 - 4

2.3 Nanocomposite materials

2.3.1 Definition and overview

Nanocomposites are a class of materials where at least one phase exists on a nanoscale, such as nanoparticles, nanotubes, or layered nanostructures. This unique structure, often ranging from 1 to 100 nanometers [66], gives rise to exceptional properties that surpass those of traditional materials. These multiphase materials offer promising solutions to limitations in conventional engineering materials. Their versatility allows for the creation of a wide range of materials with tailored properties through innovative synthetic approaches. Nanocomposites often exhibit superior mechanical, thermal, electrical, optical, and magnetic properties compared to their constituent materials. Interactions at the nanoscale interfaces between phases play a crucial role in determining the overall behavior of the material. Sometimes, nanocomposites display properties that are not present in their individual components, leading to unexpected and beneficial outcomes. By utilizing building blocks with nanoscale dimensions, researchers can design and create novel materials with unprecedented flexibility and improved physical properties. Driven by their remarkable properties, nanocomposites are experiencing rapid growth, with a corresponding surge in their applications. Within the next decade, global

production is projected to surpass 600,000 tons. These innovative materials are poised to revolutionize various sectors [67], including:

- High-Strength Fibers and Films: Nanocomposites offer superior strength-to-weight ratios, making them ideal for lightweight yet robust structures in diverse applications.
- UV Protection Gels: Nanocomposite gels can effectively shield against harmful ultraviolet (UV) radiation, finding use in sunscreens, coatings for outdoor equipment, and protective films.
- Drug Delivery Systems: With their precise control over release rates, nanocomposites pave the way for targeted and efficient drug delivery systems.
- Fire Retardant Materials: Nanocomposite formulations offer significant improvements in fire resistance, enhancing safety in construction materials, textiles, and other applications.
- Anti-Corrosion Barrier Coatings: Nanocomposites provide exceptional protection against corrosion, extending the lifespan of infrastructure, pipelines, and machinery.
- Lubricant and Stretch Paints: Nanocomposite paints can deliver both lubrication and superior elasticity, offering unique functionalities for various applications.

Beyond these, nanocomposites are also making significant strides in the automotive and industrial sectors. Their exceptional mechanical properties make them ideal for components like engine covers, door panels, and timing belt covers in vehicles. Additionally, they find use in blades for vacuum cleaners, mower hoods, and mobile phone covers.

2.3.2 Physical structure of nanofillers

Recent research has focused on developing effective nanofillers to enhance the properties of polymer nanocomposites. Nanoparticles can be categorized based on their dimensions as shown in Figure 2.2 [68]:

Zero-Dimensional (0D) Nanofillers

- Spherical Nanoparticles: These are the most common type of 0D nanofillers. They have a uniform spherical shape and are typically used to improve the mechanical, thermal, and electrical properties of nanocomposites [69].

One-Dimensional (1D) Nanofillers

- Nanofibers: Long, thin fibers with a high aspect ratio. They can significantly enhance the mechanical properties, thermal conductivity, and electrical conductivity of nanocomposites.
- Nanotubes: Cylindrical structures with a hollow core. Carbon nanotubes, in particular, exhibit exceptional mechanical, electrical, and thermal properties, making them highly sought-after nanofillers [70].

Two-Dimensional (2D) Nanofillers

- Nanosheets: Thin, plate-like structures, such as graphene and clay nanosheets. They can improve the barrier properties, mechanical strength, and thermal conductivity of nanocomposites [71].

Three-Dimensional (3D) Nanofillers

- Dendrimers: Highly branched, tree-like structures with multiple functional groups. They can be used to improve the mechanical, thermal, and electrical properties of nanocomposites, as well as for drug delivery and catalysis applications [72].

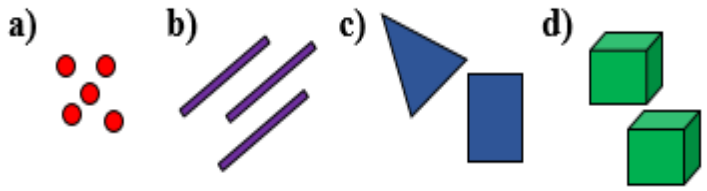

Figure 2.2 : Classification of nanofiller (a) zero-dimensional, (b) one-dimensional, (c) two-dimensional, (d) three-dimensional (nano-meter sized of fillers which are less than 100 nm) [68].

2.3.3 Nanocomposite classification

Nanocomposite materials are classified based on their matrix material [67], [68]. Here are the three main types:

- Polymer Matrix Nanocomposites (PMNCs):

  Matrix: Polymer (plastic)

  Reinforcement: Nanoparticles, nanotubes, nanofibers, or nanoclays

  Applications: Automotive components, aerospace parts, electronics, packaging, and biomedical devices.

- Ceramic Matrix Nanocomposites (CMNCs):

  Matrix: Ceramic material

  Reinforcement: Nanoceramics, carbon nanotubes, or nanofibers

  Applications: High-temperature applications, aerospace, electronics, and protective coatings.

- Metal Matrix Nanocomposites (MMNCs):

  Matrix : Metal

  Reinforcement: Nanoparticles, nanotubes, or nanofibers

  Applications: Aerospace, automotive, and structural engineering.

Due to their versatility, ease of processing, and lightweight nature, polymer matrix nanocomposites (PMNCs) are the most widely used type of nanocomposite. PMNCs have gained significant traction due to their wide range of applications in various industries, including automotive, aerospace, electronics, packaging, and biomedical fields.

A particularly promising class of PMNCs is carbon nanotube reinforced composites (CNTRCs). Carbon nanotubes (CNTs), renowned for their exceptional mechanical, electrical, and thermal properties, serve as ideal nanofillers for enhancing the performance of polymer matrices. By incorporating CNTs into polymer matrices, researchers and engineers can develop advanced materials with superior strength, stiffness, electrical conductivity, and thermal conductivity.

2.4 Carbon nanotubes (CNTs)

Carbon nanotubes (CNTs) are cylindrical carbon molecules composed of rolled-up sheets of graphene. They exist in two primary forms: single-walled carbon nanotubes (SWCNTs) and multi-walled carbon nanotubes (MWCNTs). SWCNTs consist of a single layer of graphene with diameters typically less than 1 nanometer, while MWCNTs are composed of multiple concentric layers of graphene and can have diameters exceeding 100 nanometers. Regardless of their type, CNTs can exhibit extraordinary lengths, often reaching several micrometers or even millimeters, endowing them with exceptional mechanical with young's moduli as high as 1 TPa and tensile strengths of up to 63 GPa. They also exhibit remarkable electronic properties, capable of behaving as either metals or semiconductors, depending on their specific structure and diameter [73]. As illustrated in Figure 2.3, where a network of single-walled carbon nanotubes is shown in the background, these properties are truly remarkable when considering their minuscule size, dwarfed

even by a human hair fragment (purple structure) with a diameter of about 80 to 100 thousand nanometers.

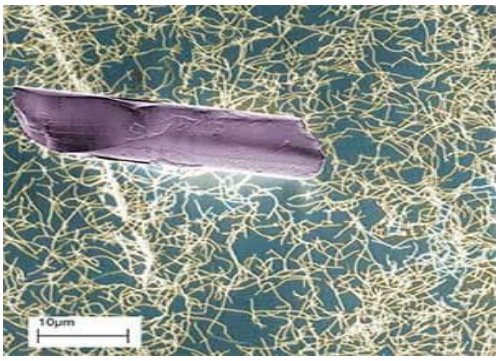

Figure 2.3 : The purple structure is a human hair fragment, with a diameter of about 80 to 100 thousand nanometers and in the background is a network of single-walled carbon nanotubes [74].

Carbon nanotubes can be classified based on their wall count: single-walled (SWCNTs), double-walled (DWCNTs), and multi-walled (MWCNTs). As illustrated in Figure 2.4, SWCNTs consist of a single graphene sheet rolled into a seamless cylinder, while MWCNTs comprise multiple concentric layers of graphene. This layered structure in MWCNTs introduces additional complexity, allowing for characterization not only by their morphology and structure but also by their texture and nanotexture. MWCNTs are essentially hollow, nano-sized carbon filaments. The spacing between adjacent graphene layers in MWCNTs typically corresponds to the van der Waals distance of approximately 0.34 nm, characteristic of turbostratic, polyaromatic carbons.

DWCNTs, on the other hand, represent a distinct class of coaxial nanostructures consisting of precisely two concentrically nested SWCNTs. Compared to SWCNTs of similar diameter, DWCNTs exhibit unique spectroscopic behavior. For instance, the inner tubes of DWCNTs demonstrate a slower decay in the intensity of their Raman modes upon electrochemical charging, unlike the rapid "bleaching" observed in SWCNTs under similar conditions. This differential response to chemical doping provides a valuable spectroscopic method for distinguishing the inner tubes of DWCNTs from individual SWCNTs [75].

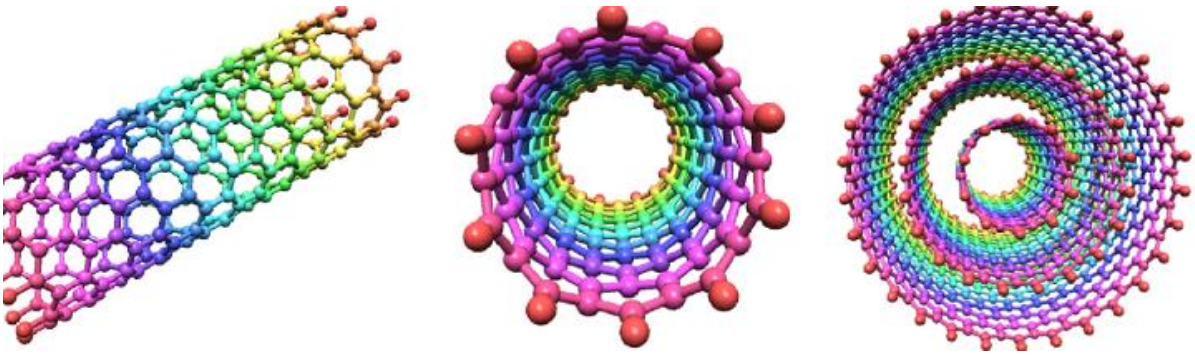

Figure 2.4: Schematic view of carbon nanotubes single walled carbon nanotube (SWCNT) and multi-walled carbon nanotube (MWCNT) [75]

An SWCNT can be visualized as a narrow rectangular strip of graphene, a single layer of sp2-bonded carbon atoms with a honeycomb lattice, rolled seamlessly into a cylinder with diameters typically ranging from 1 to 10 nanometers. The rolling process imposes specific constraints on the dimensions and orientation of the graphene strip, leading to distinct structural types: zigzag, armchair, and chiral as shown in Figure 2.5. These structural variations significantly influence the electronic properties of SWCNTs, determining whether they exhibit metallic or semiconducting behavior[76].

- **Armchair nanotubes**, characterized by high symmetry and a diameter of approximately $\sqrt{3} \times a$ (where 'a' is the graphene lattice constant), exhibit metallic behavior with a well-defined electronic band structure. Their high conductivity, exceptional mechanical strength, and excellent thermal conductivity make them promising candidates for applications in nanoelectronics, interconnects, field-effect transistors, reinforcement materials, and thermal management systems.
- **Chiral nanotubes** possess a helical structure with varying chiral angles, resulting in diverse electronic properties that can be tuned from metallic to semiconducting or a combination thereof. This tunability makes them suitable for a wide range of electronic and optoelectronic applications. Chiral nanotubes also exhibit excellent mechanical strength and flexibility, offering potential applications in nanocomposites and sensors.

- **Zigzag nanotubes**, with a diameter of approximately 3/2 × a, exhibit metallic behavior with localized edge states, enhancing conductivity and magnetic moments along the tube axis. These unique electronic and magnetic properties make zigzag nanotubes promising candidates for applications in spintronics, magnetic storage devices, and nanoelectronics. Like other SWCNTs, zigzag nanotubes possess exceptional mechanical and thermal properties, further expanding their potential applications in materials science and nanotechnology

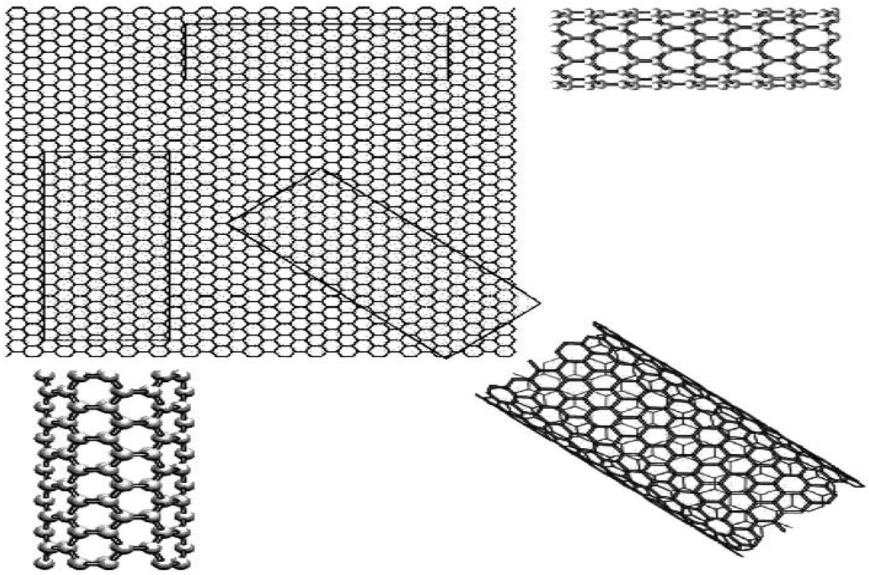

Figure 2.5: Schematic representation of how graphene sheets can be rolled up to form nanotubes [76].

2.4.1 Mechanical properties of carbon nanotubes

The exceptional mechanical properties of carbon nanotubes, such as their predicted stiffness and strength surpassing any known material, stem from the inherent strength of the carbon-carbon bonds within their structure.

Simulations [77] and experiments [78] show that carbon nanotubes exhibit a remarkable "bend, don't break" response to significant bending, as seen in individual SWNTs subjected to large transverse deformations. An example from Yakobson's simulation is shown in Figure 6. The parts of the nanotube on either side of the bent area can bend sharply without breaking. studies show that the nanotube will return to its original straight shape after bending.

The stiffness of individual MWNT was measured using a technique called transmission electron microscopy (TEM). The results showed that nanotubes can be very stiff, with a Young's modulus ranging from 1.0 to 1.8 TPa [79]. This is only slightly better than the strongest graphite fibers. Nanotubes have also shown excellent resistance to shock loads [80]. However, the stiffness and strength of nanotubes can vary greatly depending on how they are made and processed, likely due to the presence of defects. Some nanotubes made from organic materials have been found to be much less stiff, with a Young's modulus as low as 3 to 4 GPa [81]. Other tests using TEM have shown more reasonable values for the stiffness (0.8 GPa) and strength (150 GPa) of MWNT [82].

Figure 2.6: Yakobson's Simulation of SWNT Deformation

Groups of carbon nanotubes, like bundles of single-walled nanotubes (SWNTs) or multi-walled nanotubes (MWNTs), might be more resistant to bending but are likely weaker when pulled apart. In one experiment, 15 groups of SWNTs broke when stretched by only 5.3% or less. The way these groups break suggests that the load is mainly carried by the outer nanotubes, leading to estimated breaking strengths between 13 and 52 GPa [83]. This is much lower than the strength of a single MWNT [82]. However, the average stiffness was found to be 1 TPa, which is close to what would be expected for perfect nanotubes. This shows that structural imperfections have a much bigger impact on strength than on stiffness. There is always some uncertainty in how to calculate stress based on the size of the nanotube group. However, when comparing nanotubes to steel based on their weight, they perform much better, with stiffness and strength 19 and 56 times greater, respectively [84].

2.5 Carbon nanotube reinforced composite

2.5.1 Processing techniques

Several methods are used to create composites with carbon nanotubes and polymers. One common approach involves mixing nanotube solutions with polymer solutions and then removing the solvents. Often, nanotubes are chemically treated to make them easier to mix. For example, acid-treated nanotubes can be mixed with a polymer like polyvinyl alcohol (PVA) to create a composite.

Another method involves using solvents to dissolve both nanotubes and a polymer like polystyrene. This often requires treating the nanotubes with chemicals to make them soluble.

In some cases, chemical treatment isn't necessary. For instance, nanotubes can be dispersed in a solvent like toluene using high-energy sound waves, then mixed with a polystyrene solution. This technique allows for excellent nanotube distribution.

For thermoplastic polymers (those that melt when heated), melt processing techniques are used. These involve mixing nanotubes with the molten polymer using techniques like shear mixing or extrusion. This allows for creating composite shapes like fibers and films.

Epoxy resins can also be used to create nanotube composites. One method involves embedding nanotubes in liquid epoxy and allowing it to solidify. This can lead to the alignment of nanotubes.

In situ polymerization is another approach. This involves mixing nanotubes with the building blocks of the polymer (monomers) and then causing them to react to form the polymer. This technique has been used to create composites with polymers like polyaniline and polystyrene.

For some applications, layered composites are desirable. These can be made by repeatedly depositing layers of nanotubes and polymer onto a surface. This allows for creating strong, multi-layered structures [73].

2.5.2 Potential and current challenges

Several challenges hinder the widespread use of carbon nanotubes (CNTs) as effective reinforcements in polymer composites. Firstly, dispersing CNTs evenly within the polymer matrix is difficult due to their tendency to agglomerate. Moreover, current applications typically utilize only small amounts of CNTs (1-5% by weight), limiting their potential impact. Poor interfacial bonding between CNTs and the polymer matrix leads to weak interfaces, resulting

in either failure at the interface or the pulling out of individual CNTs from multi-walled nanotubes (MWNTs). Additionally, achieving uniform alignment of CNTs within the polymer matrix remains a significant challenge. Secondly, the length of commercially available CNTs is typically limited (0.5-5 micrometers), which hinders their ability to effectively transfer load to the polymer matrix. For effective load transfer, the CNT length needs to exceed a critical value, which depends on the CNT's strength, diameter, and the strength of the CNT-matrix bond. While longer CNTs have been synthesized in research settings, their commercial availability is limited. Thirdly, the high cost of CNT production remains a significant barrier. Current synthesis methods are expensive, and scaling up production methods like arc discharge and laser ablation is challenging. Furthermore, the presence of defects such as impurities and structural imperfections in commercially available CNTs can negatively impact their performance in composites. Research efforts are ongoing to address these challenges, including developing improved dispersion techniques, synthesizing longer and more uniform CNTs, enhancing interfacial bonding, and developing more cost-effective and scalable production methods [85].

2.6 Carbon nanotube reinforced composite plates

Fabricating high-quality CNT-reinforced composite plates presents significant challenges, including achieving uniform dispersion of CNTs within the polymer matrix, controlling the alignment of CNTs, and ensuring consistent thickness and density across the plate. Despite these challenges, researchers have developed various fabrication techniques and employed advanced simulation methods to predict the behavior of these complex materials. Accurate geometric characterization and mechanical testing are crucial to validate simulation results, understand the influence of fabrication parameters on plate properties, and ultimately optimize the design and performance of CNT-reinforced composite plates for various applications.

2.1.1.Geometric and mechanical characterization of a multilayer reinforced composite plate

Consider a multilayer composite plate with functionally graded mechanical properties, made of a mixture of carbon-based nanofibers (CNT) and an isotropic polymer matrix. The plate of dimensions $L(0 \le x \le L) \times W(0 \le y \le W) \times h(-h/2 \le z \le h/2)$ is referred to a Cartesian coordinate system (x, y, z) as shown in Figure 2.7. The plate is subdivided according to its

thickness into N_L sub-layers of equal thickness, given by $h_L = h / N_L$. The nanofibers are homogeneously dispersed in the (x, y) plane and gradually distributed in the thickness following different types of distributions, namely: uniformly distributed (UD), functionally graded in V shape (FG-V), in Λ shape (FG-Λ), in O shape (FG-O) and in X shape (FG-X).

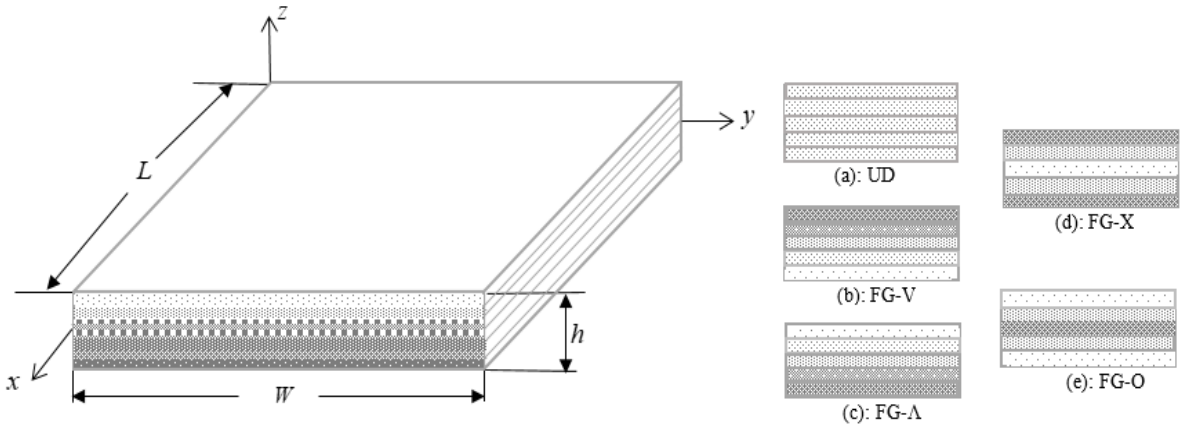

Figure 2.7 : Geometric parameters of FG-CNTRC plate and typical distribution patterns.

As shown in Figure 2.7, in the UD type, the nanofibers are distributed evenly throughout the thickness of the multilayer. In contrast, in the FG-V, FG-Λ, FG-O, and FG-X types, the nano-reinforcements are distributed gradually, linearly or non-linearly. The FG-V type allows for a high concentration of nanofibers on the upper surface of the plate; in other words, the volume fraction of nanofibers is maximal, decreasing gradually to the lower surface, where it reaches a very low distribution rate of nanofibers. The opposite phenomenon is observed in the case of the FG-Λ type. The FG-X model exhibits a high distribution of nanofibers on the upper and lower surfaces of the plate, while on the middle surface the distribution of nanofibers is low. As for the FG-O type, the distribution is reversed compared to the FG-X type.

Based on the distribution patterns discussed earlier, the volume fraction of nanofillers within a given sublayer (k) can be mathematically defined using the following expression [86]:

UD: $$f_{CNT}^{(k)} = f_{CNT}^{*} \tag{2.1}$$

FG-X: $$f_{CNT}^{(k)} = (1 + Pin)\left(\frac{|2k - N_L - 1|}{N_L}\right)^{Pin} f_{CNT}^{*} \tag{2.2}$$

FG-O: $$f_{CNT}^{(k)} = (1+Pin)\left(1-\frac{|2k-N_L-1|}{N_L}\right)^{Pin} f_{CNT}^{*} \quad (2.3)$$

FG-A: $$f_{CNT}^{(k)} = (1+Pin)\left(\frac{(0.5-k+N_L)}{N_L}\right)^{Pin} f_{CNT}^{*} \quad (2.4)$$

FG-V: $$f_{CNT}^{(k)} = (1+Pin)\left(\frac{k-0.5}{N_L}\right)^{Pin} f_{CNT}^{*} \quad (2.5)$$

Where:

$k = 1,2,3...N_L$, Pin is the power-law index and f_{CNT}^{*} is the total volume fraction of CNTRC given by the following equation:

$$f_{CNT}^{*} = \frac{w_{CNT}}{(1-w_{CNT})(\rho_{CNT}/\rho_m)+w_{CNT}} \quad (2.6)$$

w_{CNT} is the weight fraction of the Nano-fillers. ρ_{CNT} and ρ_m are the Nano-fillers and matrix mass density, respectively.

2.6.1 Mechanical properties of CNTRC plate

To estimate the mechanical properties of nanocomposite plate, two models, namely the rule of mixture and the Halpin-Tsai model are commonly used.

2.6.1.1 The rule of mixture:

The rule of mixture uses the following equations to calculate the elastic moduli of CNTRC plates [59], [87]:

E_{11} and E_{22} are respectively the longitudinal and transverse elastic modulus and G_{21} is the shear modulus given as follows:

$$E_{11}^{(k)} = f_{CNT}^{(k)}\eta_1 E_{11}^{CNT} + E_m(1-f_{CNT}^{(k)}) \quad (2.7)$$

$$E_{22}^{(k)} = \frac{\eta_2}{\frac{f_{CNT}^{(k)}}{E_{22}^{CNT}} + \frac{1-f_{CNT}^{(k)}}{E_m}} \quad (2.8)$$

$$G_{12}^{(k)} = \frac{\eta_3}{\frac{f_{CNT}^{(k)}}{G_{12}^{CNT}} + \frac{1 - f_{CNT}^{(k)}}{G_m}} \tag{2.9}$$

In these equations, E_{11}^{CNT}, E_{22}^{CNT}, E_m, G_{12}^{CNT} and G_m represent the elastic and shear moduli of the CNTs and matrix, respectively. η_j $(j = 1, 2, 3)$ represent the CNT reinforced composite efficiency parameters, these are numbers introduced into the equations to account for the small scale effect.

The densities and the Poisson's ratio of the CNTRC plate for the *kth* layer, using the rule of mixture are calculated as**:**

$$\rho^{(k)} = f_{CNT}^{(k)} \rho_{CNT} + (1 - f_{CNT}^{(k)}) \rho_m \tag{2.10}$$

$$\nu_{12}^{(k)} = f_{CNT}^{*} \nu_{12}^{CNT} + (1 - f_{CNT}^{(k)}) \nu_m \tag{2.11}$$

ρ_{CNT} and ν_{12}^{CNT} are the density and Poisson's ratio of CNT, respectively. While ρ_m and ν_m are the density and Poisson's ratio of the matrix, respectively.

2.6.1.2 The Halpin-Tsai model

This method relies on the following equations for calculating the elastic moduli of CNTRC plates [88]:

$$E_{11}^{(k)} = \left(\frac{1 + \xi \eta_L f_r^{(k)}}{1 - \eta_L f_r^{(k)}} \right) E_m \tag{2.12}$$

$$E_{22}^{(k)} = \left[\frac{3}{8} \left(\frac{1 + \xi \eta_L f_r^{(k)}}{1 - \eta_L f_r^{(k)}} \right) + \frac{5}{8} \left(\frac{1 + 2\eta_D f_r^{(k)}}{1 - \eta_D f_r^{(k)}} \right) \right] E_m \tag{2.13}$$

$$G_{12}^{(k)} = \left(\frac{1 + \eta_L f_r^{(k)}}{1 - \eta_L f_r^{(k)}} \right) G_m \tag{2.14}$$

Where:

$$\eta_L = \frac{(E_{cn}/E_m)-1}{(E_{cn}/E_m)+\xi} \tag{2.15}$$

$$\eta_D = \frac{(E_{cn}/E_m)-1}{(E_{cn}/E_m)+2} \tag{2.16}$$

$$\xi = 2(\ell_{cn}/D_{cn}) \tag{2.17}$$

$$\eta = \frac{(G_{cn}/G_m)-1}{(G_{cn}/G_m)+1} \tag{2.18}$$

In which E_{cn} and E_m are the elastic modulus of the CNTs and matrix, respectively. D_{cn} and ℓ_{cn} are the outer diameter and length of the CNTs, respectively.

2.7 Conclusion

In this chapter, we explored the fascinating world of composite materials, starting with a general overview of their definition, classification, and applications. We then delved into the realm of nanocomposites, focusing on the unique properties of nanofillers and the various ways they can be incorporated into matrices to create materials with enhanced performance. A significant portion of the chapter was dedicated to carbon nanotubes (CNTs), examining their exceptional structural and functional properties, as well as the diverse methods employed for their synthesis.

Furthermore, we investigated the fabrication and characterization of CNT-reinforced composites, paying particular attention to the challenges associated with achieving uniform dispersion, controlling CNT alignment, and ensuring strong interfacial bonding. We also discussed the critical role of geometric and mechanical characterization techniques in evaluating the performance of these advanced materials.

This comprehensive review highlights the immense potential of CNT-reinforced composites to revolutionize various industries. However, significant challenges remain, including the high cost of CNT production, the need for scalable and efficient manufacturing processes, and the need for a deeper understanding of the structure-property relationships in these complex materials.

CHAPTER 3
EXTENDED FINITE ELEMENT METHOD

3.1 Introduction

This chapter presents the numerical formulation used to model the free vibration behavior of cracked plates within the framework of the Extended Finite Element Method (XFEM). The objective is to establish the theoretical foundations required to incorporate discontinuities without modifying the mesh. To achieve this, the displacement approximation, enrichment strategy, and strain–displacement relations are developed in detail. The corresponding stiffness and mass matrices are then derived to construct the dynamic system. Overall, this chapter provides the mathematical basis that supports the XFEM implementation used in the subsequent numerical analyses.

3.2 Extended finite element method

The Extended Finite Element Method (XFEM) is a powerful numerical technique that was first introduced in 1999 by Moes et al [22], it extends the classical Finite Element Method (FEM) to model problems involving discontinuities, singularities, and complex geometries without the need for mesh refinement or conforming meshes. Traditional FEM struggles with problems where the solution field exhibits localized features such as cracks, material interfaces, or voids, as it requires the mesh to align with these features, leading to computationally expensive and often impractical meshing processes.

XFEM addresses these limitations by enriching the standard FEM approximation with additional functions that capture the local behavior of the solution. This enrichment is achieved through the partition of unity method, which allows the incorporation of known analytical solutions or special functions into the finite element space. The versatility of XFEM has made it a popular choice in various fields, including fracture mechanics, fluid-structure interaction, phase transformations, and bio-mechanics. Its ability to handle complex geometries and

evolving discontinuities has opened new possibilities for simulating real-world engineering problems with greater accuracy and efficiency.

This chapter provides an overview of the theoretical foundations of XFEM, its implementation, and its applications. Key concepts such as enrichment strategies, level set methods for tracking discontinuities, and numerical integration techniques will be discussed. Additionally, case studies and examples will be presented to illustrate the advantages of XFEM over traditional FEM in solving challenging problems.

3.3 Crack modeling using discontinuities enrichment

Consider a two-dimensional region with a discontinuity of any kind. The extended finite element method (XFEM) employs a specific approximation to determine the displacement at a point x within this region:

$$\Delta(x) = \Delta^{EF} + \Delta^{Enrich} = \sum_{i \in I} N_i(x)\delta_i + \sum_{j \in J} N_j(x) f(x)\delta_j^{'} \tag{3.1}$$

the term $\Delta^{EF} = \sum_{i \in I} N_i(x)\delta_i$ represents the classical finite element approximation, in which N_i and δ_i are the shape function and the classical nodal displacement at node i, respectively. The second term $\Delta^{Enrich} = \sum_{j \in J} N_j(x) f(x)\delta_j^{'}$ is the enrichment added by XFEM to account for the discontinuity, in which J represents the set of nodal points located on the discontinuity. $\delta_j^{'}(j \in J)$ are the degrees of freedom of enriched nodal and f is the enrichment function.

When two or more discontinuities (n_c) are present in the region, the equation (3.1) takes the following form:

$$\Delta(x) = \Delta^{EF} + \Delta^{Enrich} = \sum_{i \in I} N_i(x)\delta_i + \sum_{l=1}^{n_c} \sum_{j \in J} N_j(x) f(x)\delta_j^{'} \tag{3.2}$$

To simulate discontinuities (like cracks) in 2D models, the authors Möes, Dolbow, and Belytschko [25] used two types of enrichment functions:

- Heaviside Step Functions: These are used for elements that are completely split by the discontinuity. The Heaviside function is like a switch that abruptly changes value at the discontinuity, capturing the jump in the solution.
- Asymptotic Functions: For elements where the discontinuity ends (like at a crack tip), special functions are used. These functions are based on the known mathematical form of the solution near a crack tip, which has a characteristic shape.

The Heaviside function was first introduced by Moes in 1999, it is a mathematical function that's like a switch. By adding the Heaviside function to the standard FEM equations, the method can now handle elements that are completely split by the discontinuity, it has a value of -1 on one side of the discontinuity and +1 on the other. This abrupt change in value helps represent the "jump" in the material's displacement across the crack.

Moës developed a framework for crack representation that was independent of the finite element mesh. To illustrate the concept of discontinuous enrichment, he began with a simple model of an edge crack consisting of four elements (Figure 3.1). By aligning the local coordinate system with the crack tip, he showed how a discontinuous field could be introduced to create an equivalent discrete space (Figure 3.1b). This enriched space allowed the crack to be represented without conforming to the element boundaries, a key innovation of the XFEM method. The standard finite element approximation based on the mesh in Figure 3.1a is:

$$\Delta = \sum_{i=1}^{10} N_i \delta_i \tag{3.3}$$

In which δ_i is the displacement at node i, and N_i is the shape function associated with node i.

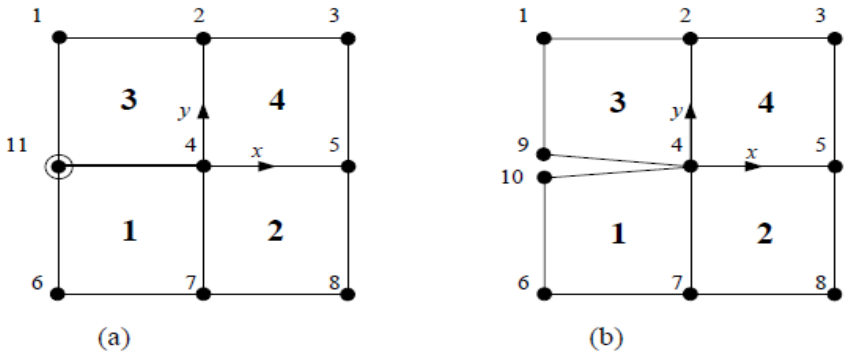

Figure 3.1: finite element mesh of discontinuous enrichment

(a) Regular mesh with enrichment of node 9

(b) Finite element mesh near a crack tip

the average displacement *a* and the displacement jump *b* of the double node are defining as:

$$a = \frac{\delta_9 + \delta_{10}}{2}, \qquad b = \frac{\delta_9 - \delta_{10}}{2}, \tag{3.4}$$

From (3.4), We can express δ_9 and δ_{10} in a term of *a* and *b:*

$$\delta_9 = a + b \ , \qquad \delta_{10} = a - b \tag{3.5}$$

Now replacing δ_9 and δ_{10} with their expressions in (3.3) we get :

$$\Delta = \sum_{i=1}^{8} N_i \delta_i + a(N_9 + N_{10}) + b(N_9 + N_{10}) H(x) \tag{3.6}$$

Where $H(x)$ is referred to the jump function, or Heaviside function. This is defined in the local crack co-ordinate system as:

$$H(x,y) = \begin{cases} +1 & (y > 0) \\ -1 & (y < 0) \end{cases} \tag{3.7}$$

H(x)=1 on element 1 and -1 on element 3, respectively.

$N_{11} = N_9 + N_{10}$ and $\delta_{11} = a$, We can rewrite the equation (3.6) as follow:

$$\Delta = \sum_{i=1}^{8} N_i \delta_i + \delta_{11} N_{11} + b N_{11} H(x) \tag{3.8}$$

When the crack tip isn't on an element edge (like in Figure 3.2), a simple jump function isn't enough. It only models the crack up to point 'p'. To model the whole crack, we also enrich the

squared nodes (in addition to the circled nodes) with special crack tip functions, as described in Belytschko and Black [21]. This allows us to accurately represent the discontinuity, and the approximation takes a specific form as follow:

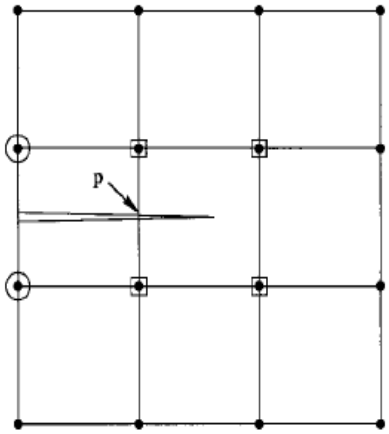

Figure 3.2: crack not aligned with the mesh, circled nodes use a discontinuous function for enrichment, while squared nodes use tip enrichment functions

$$\Delta = \sum_{i \in I} \delta_i N_i + \sum_{j \in J} b_j N_j H(x) + \sum_{k \in K} N_k \left(\sum_{l=1}^{4} c_k^l F_l(x) \right) \tag{3.9}$$

In which J is the set of circled nodes (those enriched with the Heaviside function), and K is the set of squared nodes (those use tip enrichment functions). *b* are the degrees of freedom associated with the node enriched by *H*, while *c* are the degrees of freedom associated with the asymptotic functions, the functions $F_l(x)$ are defined as;

$$\left\{ F_l(r,\theta) \right\} = \left\{ \sqrt{r} \sin\left(\frac{\theta}{2}\right), \sqrt{r} \cos\left(\frac{\theta}{2}\right), \sqrt{r} \sin\left(\frac{\theta}{2}\right) \sin(\theta), \sqrt{r} \cos\left(\frac{\theta}{2}\right) \sin(\theta) \right\} \tag{3.10}$$

Where (r,θ) are the local polar coordinates at the crack tip (Figure 3.3), the function $H(x)$ is the Heaviside function defined by (3.7) where the local axes aligned with the crack tip (Figure 3.1).

Now consider an arbitrary crack (Figure 3.4) the approximation becomes:

$$\Delta = \sum_{i \in I} \delta_i N_i + \sum_{j \in J} b_j N_j H(x) + \sum_{k \in K_1} N_k \left(\sum_{l=1}^{4} c_k^{l1} F_l^1(x) \right) + \sum_{k \in K_2} N_k \left(\sum_{l=1}^{4} c_k^{l2} F_l^2(x) \right) \tag{3.11}$$

Where K_1 and K_2 are the sets of nodes to be enriched for the first and second crack tip, respectively.

The functions $F_l^1(x)$ and $F_l^2(x)$ are identical to the ones given in (3.10). The crack is considered to be a curve, starting at one crack tip. For any point *X*, X^* is the closest point on the crack (Figure 3.4). The Heaviside function given by the equation (3.12) can be defined as the sign of the product (X-X^*). e_n . e_s and e_n are unit vectors, where e_s is tangent to the discontinuity (crack) at X^* and points in the crack's growth direction, and e_n is normal to the discontinuity at X^* and points perpendicular to the crack face.

$$H(x) = \begin{cases} +1 & for\left(X - X^*\right).e_n > 0 \\ -1 & for\left(X - X^*\right).e_n < 0 \end{cases} \tag{3.12}$$

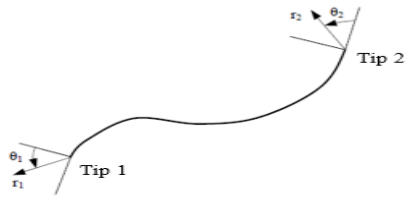

Figure 3.3:local polar coordinates at the crack tips

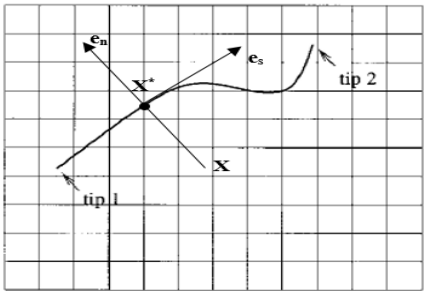

Figure 3.4:An arbitrary crack placed on a mesh, the jump function in this case (H(x)=-1)

3.4 Selection of enriched nodes

The extended finite element method introduces, through enrichment functions, additional degrees of freedom. These are associated with nodes whose support region is cut by the discontinuity [54]. A node is enriched if at least one of the interior edges of its support region is cut by the discontinuity. A simple example is shown in Figure 3.5; for node I of the mesh, the discontinuity cuts at least one of the interior edges of region R_I, so node I will be enriched.

Figure 3.6 illustrates the case of an arbitrary crack in a regular finite element mesh. The nodes of elements completely crossed by the discontinuity are enriched by Heaviside functions *H*, while the nodes of elements containing the crack tips are enriched by asymptotic functions *F*, given by equation 3.10.

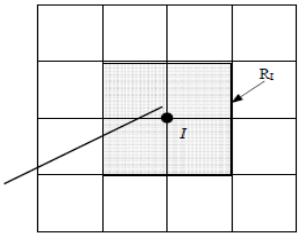

Figure 3.5: enriched node *I* in the support region R_I

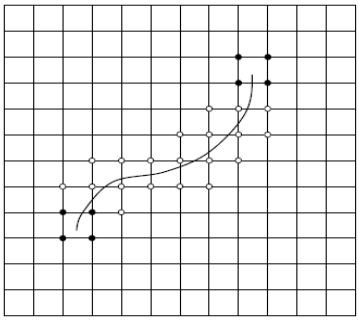

Figure 3.6: Heaviside and Asymptotic Enrichment for arbitrary Crack

○ Nodes enriched with the Heaviside functions

• Nodes enriched with asymptotic functions

3.5 Numerical integration

Addressing the challenge of accurate numerical integration within elements intersected by a crack has been a subject of significant research. Dolbow et al [25] proposed a method involving the subdivision of cracked elements into simpler subpolygons, such as triangles as shown in Figure 3.7. This subdivision enables the accurate integration of the discontinuous enrichment function, which is crucial when the crack orientation is arbitrary within an element. Standard Gauss quadrature may not adequately capture the discontinuity in such cases, potentially leading to spurious singular modes in the system of equations.

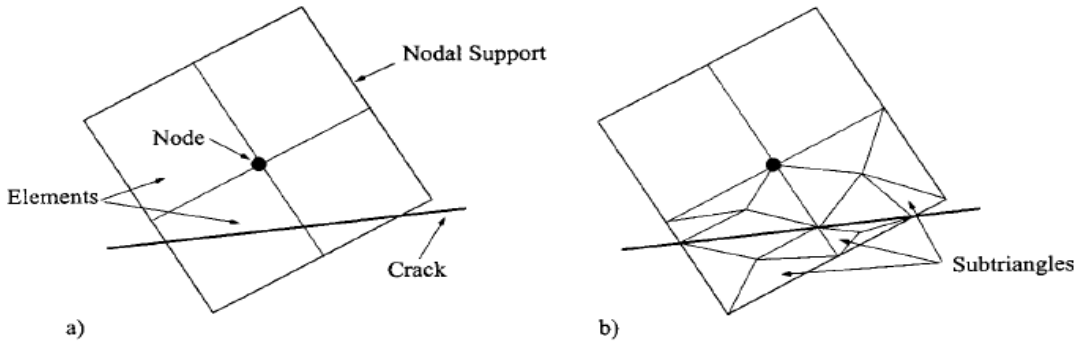

Figure 3.7: (a) Nodes located within the region affected by the crack.

(b) Sub-triangles generated within elements intersected by the crack for node selection and numerical integration of the weak form.

Ventura (2006) [40] presented an alternative approach that avoids the need for subcells. By replacing the discontinuous enrichment function with an equivalent polynomial, this method allows for the application of standard Gauss quadrature over the entire element domain. The equivalence relation is derived using the level set representation of the discontinuity surface, ensuring that the integration results are identical to those obtained using subcell integration. While this method is exact for triangular and tetrahedral elements, an approximation is required for quadrilateral elements with non-parallel opposite sides. Nistor et al (2008) [89] introduced yet another approach, subdividing the cracked element into sub-quadrilaterals as shown in Figure 3.8 and employing bilinear shape functions to interpolate the fields within these sub-quadrilaterals. This method, coupled with the use of the same integration scheme as for other elements in the mesh, has been shown to yield more accurate results compared to traditional sub-triangulation methods.

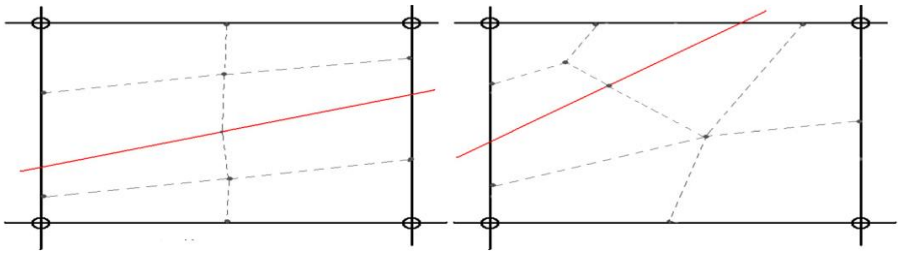

Figure 3.8: partitioning of four nodes elements

3.6 Discretization

Based on Figure 2.7, the plate's mid-surface is discretized into a mesh of quadrilateral isoperimetric finite elements, as illustrated in Figure 3.9. The standard nodes (black) possess 5 degrees of freedom (three displacements and two rotations), whereas the enriched nodes (red) have 10 degrees of freedom, an increase of 5 degrees of freedom, these additional degrees of freedom are multiplied by the enrichment functions, they allow the element to capture the discontinuity's behavior without requiring mesh refinement or remeshing.

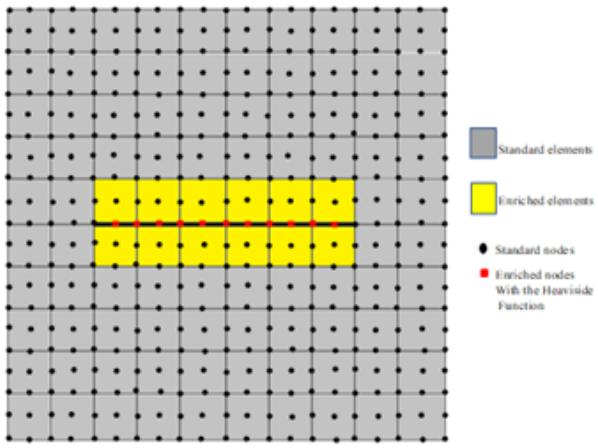

Figure 3.9: discretization of a 10x10 mesh of a cracked plate.

We have therefore chosen a mesh zone (Figure 3.10(a)) containing one cut element (E1), two elements with 3 enriched nodes (E2 and E4), and one element with a single enriched node (E3). For these elements, we retain the local numbering for their nodes.

it is advantageous to use a system of natural or intrinsic coordinates instead of the system of physical coordinates. This allows for the definition of a transformation from the physical domain of the element to a simple, dimensionless geometric domain. This system is defined by axes parallel to the sides of the element; the coordinates of the corner nodes take on unit values (+1 or -1), and the interface nodes take on the values 0 and 1 or -1 (Figure 3.10 (b)).

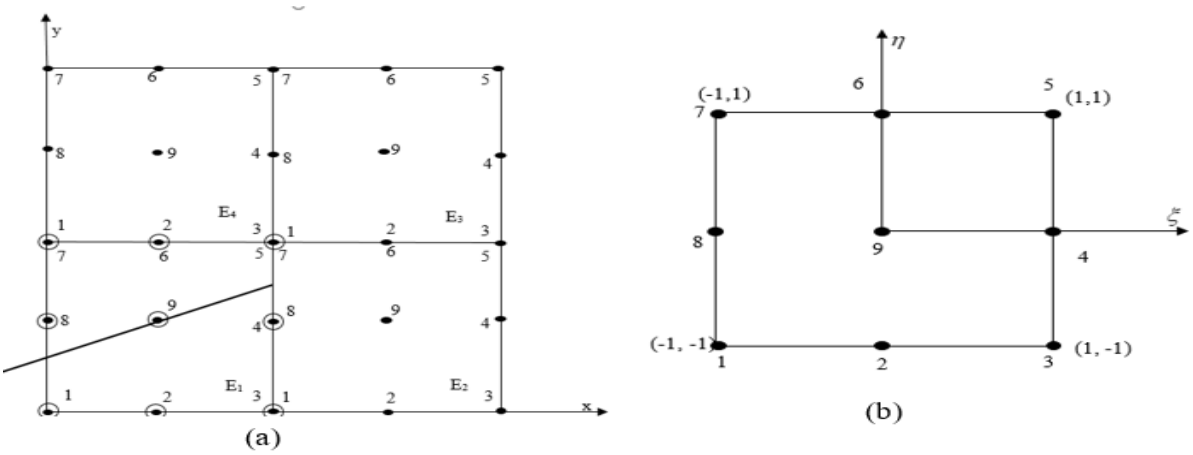

Figure 3.10: (a): A mesh zone with a discontinuous element

(b): Reference element

The elemental displacements are defined by

$$u_0 = \sum_I N_i u_{oi} + \sum_J N_j u'_{0j} \qquad v_0 = \sum_I N_i v_{oi} + \sum_J N_j v'_{0j} \qquad w_0 = \sum_I N_i w_{oi} + \sum_J N_j w'_{0j}$$

$$\theta_x = \sum_I N_i \theta_{xi} + \sum_J N_j \theta'_{xj} \qquad \theta_y = \sum_I N_i \theta_{yi} + \sum_J N_j \theta'_{yj} \tag{3.13}$$

Where N are the interpolation functions that govern the displacement field within the element's domain are expressed using the (ξ,η) coordinates of the parent domain, as shown in Figure 3.10 (b), by:

for the corner nodes: $\xi_i = \pm 1 \;\; ; \;\; \eta_i = \pm 1$

$$N_i = \frac{1}{4}\left(1+\xi\xi_i\right)\left(1+\eta\eta_i\right)\xi\eta$$

For the interface nodes:

$$N_i = \frac{1}{2}\left(1-\xi^2\right)\left(1+\eta\eta_i\right)\eta\eta_i \qquad \text{at} \qquad \xi_i = 0 \;\; ; \;\; \eta_i = \pm 1$$

$$N_i = \frac{1}{2}\left(1-\eta^2\right)\left(1+\xi\xi_i\right)\xi\xi_i \qquad \text{at} \qquad \xi_i = \pm 1 \;\; ; \;\; \eta_i = 0$$

For the center node:

$$N_i = \left(1-\xi^2\right)\left(1+\eta^2\right)$$

To transform derivatives from the global (Cartesian) coordinate system (x, y) to the natural (or intrinsic) coordinate system (ξ, η), the Jacobian matrix is used. This involves pre-multiplying the derivatives in the natural coordinate system by the inverse of the Jacobian matrix, as follow:

$$\begin{Bmatrix} \frac{\partial N_i}{\partial x} \\ \frac{\partial N_i}{\partial y} \end{Bmatrix} = [J]^{-1} \begin{Bmatrix} \frac{\partial N_i}{\partial \xi} \\ \frac{\partial N_i}{\partial \eta} \end{Bmatrix} \tag{3.14}$$

Where the Jacobian matrix is defined as:

$$[J] = \begin{bmatrix} \frac{\partial x}{\partial \xi} & \frac{\partial y}{\partial \xi} \\ \frac{\partial x}{\partial \eta} & \frac{\partial y}{\partial \eta} \end{bmatrix} \tag{3.15}$$

In which:

$$\begin{aligned} \frac{\partial x}{\partial \xi} &= \sum_{i=1}^{NN} \frac{\partial N_i(\xi,\eta)}{\partial \xi} x_i \\ \frac{\partial y}{\partial \xi} &= \sum_{i=1}^{NN} \frac{\partial N_i(\xi,\eta)}{\partial \xi} y_i \\ \frac{\partial x}{\partial \eta} &= \sum_{i=1}^{NN} \frac{\partial N_i(\xi,\eta)}{\partial \eta} x_i \\ \frac{\partial y}{\partial \eta} &= \sum_{i=1}^{NN} \frac{\partial N_i(\xi,\eta)}{\partial \eta} y_i \end{aligned} \tag{3.16}$$

3.7 Application to the vibration analysis of cracked plates

We are examining the Mindlin-Reissner plate model [90], which is the most commonly used approach in practical applications. This model is particularly well-suited for analyzing thick plates where transverse shear deformations play a significant role. It operates under the assumption that a line normal to the mid-surface of the plate remains straight after deformation but does not necessarily stay normal to the mid-surface. In its finite element formulation, the compatibility condition only requires C0 continuity. Furthermore, employing elements from the Lagrange family enables the analysis of both thin and thick plates.

In the subsequent discussion, the Extended Finite Element Method (XFEM) is utilized for the vibration analysis of cracked plates, incorporating Mindlin-Reissner kinematics. The cracks

under consideration are stationnary and extend through the entire thickness of the plate; crack propagation is not addressed in this study. In the XFEM framework, only Heaviside function (H) enrichment is considered. This approach necessitates that the crack tips (or discontinuities) be positioned along the edges of the finite elements. While enrichment with asymptotic functions can enhance the calculation of stress intensity factors when elements contain crack tips, this is not applicable here. The method will be applied sequentially to the analysis of composite plates.

3.7.1 Displacement field

The cracked plate analyzed here is a composite laminate with dimensions *L* and *W* and thickness *h* (Figure 3.11). The crack size is denoted as *c*. The laminate comprises *n* layers of identical material, each with differing fiber orientations (Figure 2.7). The displacement field of an arbitrary point *M* within the plate, relative to the middle surface, is determined using the Yang, Norris, and Stavsky theory [91]. This theory extends the Mindlin-Reissner plate theory to account for the complexities of composite materials. The displacement is given by:

$$\begin{aligned} u(x,y,z) &= u_0(x,y) + z\theta_x(x,y) \\ v(x,y,z) &= v_0(x,y) + z\theta_y(x,y) \\ w(x,y,z) &= w_0(x,y) \end{aligned} \tag{3.17}$$

u, v, w are the translations of pointe *M* in the *x, y* and *z* directions, respectively. *w* represents the transverse displacement of the middle surface, while θ_x and θ_y denote the rotations of the normal to the middle surface in the *xz* and *yz* planes, respectively.

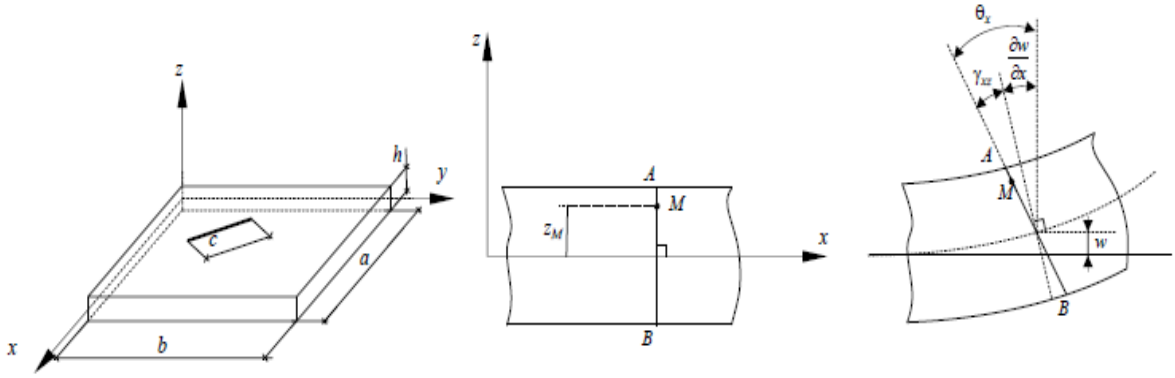

Figure 3.11: Geometry of a cracked rectangular plate and its associated deformations

3.7.2 Strain field

Based on the first order deformation theory (FSDT), the strain field is derived from the displacement field (3.17) and is written:

$$\begin{aligned}
\varepsilon_x &= \frac{\partial u}{\partial x} = \frac{\partial u_0}{\partial x} + z\frac{\partial \theta_x}{\partial x} = \varepsilon_{x0} + z\kappa_x \\
\varepsilon_y &= \frac{\partial v}{\partial y} = \frac{\partial v_0}{\partial y} + z\frac{\partial \theta_y}{\partial y} = \varepsilon_{y0} + z\kappa_y \\
\gamma_{xy} &= \frac{\partial u}{\partial y} + \frac{\partial v}{\partial x} = \left(\frac{\partial u_0}{\partial y} + \frac{\partial v_0}{\partial x}\right) + z\left(\frac{\partial \theta_x}{\partial y} + \frac{\partial \theta_y}{\partial x}\right) = \gamma_{xy0} + z\kappa_{xy} \\
\gamma_{xz} &= \frac{\partial u}{\partial z} + \frac{\partial w}{\partial x} = \theta_x + \frac{\partial w_0}{\partial x} \\
\gamma_{yz} &= \frac{\partial v}{\partial z} + \frac{\partial w}{\partial y} = \theta_y + \frac{\partial w_0}{\partial y}
\end{aligned} \tag{3.18}$$

With:

$$\varepsilon_{x0} = \frac{\partial u_0}{\partial x}, \quad \varepsilon_{y0} = \frac{\partial v_0}{\partial y}, \quad \gamma_{xy0} = \frac{\partial u_0}{\partial y} + \frac{\partial v_0}{\partial x}, \quad \kappa_x = \frac{\partial \theta_x}{\partial x}, \quad \kappa_y = \frac{\partial \theta_y}{\partial y}, \quad \kappa_{xy} = \frac{\partial \theta_x}{\partial y} + \frac{\partial \theta_y}{\partial x}$$

The equations (3.18) can be expressed as:

$$\begin{Bmatrix} \varepsilon_x \\ \varepsilon_y \\ \gamma_{xy} \\ \gamma_{yz} \\ \gamma_{xz} \end{Bmatrix} = \begin{Bmatrix} \partial u_0/\partial x \\ \partial v_0/\partial y \\ \partial u_0/\partial y + \partial v_0/\partial x \\ \partial w_0/\partial y + \theta_y \\ \partial w_0/\partial x + \theta_x \end{Bmatrix} + z\begin{Bmatrix} \partial \theta_x/\partial x \\ \partial \theta_y/\partial y \\ \partial \theta_x/\partial y + \partial \theta_y/\partial x \\ 0 \\ 0 \end{Bmatrix} \tag{3.19}$$

3.7.3 XFEM formulation

In classical finite element analysis of plates, each node *i* has five degrees of freedom: three translations (*u*, *v*, and *w*) in the *x*, *y*, and *z* directions, and two rotations (θ_x and θ_y) about the *x* and *y* axes. Enriching these nodes in the Extended Finite Element Method (XFEM) doubles the degrees of freedom. Thus, the XFEM formulation becomes [24]:

$$\begin{Bmatrix} u \\ v \\ w \\ \theta_x \\ \theta_y \end{Bmatrix} = \sum_{i\in I} \begin{bmatrix} N_i & 0 & 0 & 0 & 0 \\ & N_i & 0 & 0 & 0 \\ & & N_i & 0 & 0 \\ & sym & & N_i & 0 \\ & & & & N_i \end{bmatrix} \begin{Bmatrix} u_{0i} \\ v_{0i} \\ w_{0i} \\ \theta_{xi} \\ \theta_{yi} \end{Bmatrix} + \sum_{j\in J} \begin{bmatrix} HN_j & 0 & 0 & 0 & 0 \\ & HN_j & 0 & 0 & 0 \\ & & HN_j & 0 & 0 \\ & sym & & HN_j & 0 \\ & & & & HN_j \end{bmatrix} \begin{Bmatrix} u'_{0j} \\ v'_{0j} \\ w'_{0j} \\ \theta'_{xj} \\ \theta'_{yj} \end{Bmatrix} \tag{3.20}$$

its compact form is:

$$\{\Delta\} = \sum_{i\in I} [N_i]\{\delta_i\} + \sum_{j\in J} H(x)[N_j]\{\delta'_j\} \tag{3.21}$$

3.7.3.1 : Elementary strain field

Equations (3.13) and (3.18) define the relationship between strains and nodal displacements, considering membrane strains. It is written as:

$$\begin{Bmatrix} \varepsilon_{0x} \\ \varepsilon_{0y} \\ \gamma_{0xy} \\ \kappa_x \\ \kappa_y \\ \kappa_{xy} \\ \gamma_{xz} \\ \gamma_{yz} \end{Bmatrix} = \sum_I \begin{bmatrix} \partial N_i/\partial x & 0 & 0 & 0 & 0 \\ 0 & \partial N_i/\partial y & 0 & 0 & 0 \\ \partial N_i/\partial y & \partial N_i/\partial x & 0 & 0 & 0 \\ 0 & 0 & 0 & \partial N_i/\partial x & 0 \\ 0 & 0 & 0 & 0 & \partial N_i/\partial y \\ 0 & 0 & 0 & \partial N_i/\partial y & \partial N_i/\partial x \\ 0 & 0 & \partial N_i/\partial x & N_i & 0 \\ 0 & 0 & \partial N_i/\partial y & 0 & N_i \end{bmatrix} \begin{Bmatrix} u_{oi} \\ v_{oi} \\ w_{oi} \\ \theta_{xi} \\ \theta_{yi} \end{Bmatrix} +$$

$$\sum_J \begin{bmatrix} H\frac{\partial N_j}{\partial x} & 0 & 0 & 0 & 0 \\ 0 & H\frac{\partial N_j}{\partial y} & 0 & 0 & 0 \\ H\frac{\partial N_j}{\partial y} & H\frac{\partial N_j}{\partial x} & 0 & 0 & 0 \\ 0 & 0 & 0 & H\frac{\partial N_j}{\partial x} & 0 \\ 0 & 0 & 0 & 0 & H\frac{\partial N_j}{\partial y} \\ 0 & 0 & 0 & H\frac{\partial N_j}{\partial y} & H\frac{\partial N_j}{\partial x} \\ 0 & 0 & H\frac{\partial N_j}{\partial x} & HN_j & 0 \\ 0 & 0 & H\frac{\partial N_j}{\partial y} & 0 & HN_j \end{bmatrix} \begin{Bmatrix} u'_{0j} \\ v'_{0j} \\ w'_{oj} \\ \theta'_{xj} \\ \theta'_{yj} \end{Bmatrix} \tag{3.22}$$

Its compact form is:

$$\{\varepsilon\} = [B_i]\{\delta_i\} + [B'_j]\{\delta'_j\} \tag{3.24}$$

Where;

$$[B'_j] = H[B_j] \tag{3.25}$$

3.7.3.2 : Stress-Strain Relationship

The stress-strain relationship for the entire laminate must first be established for each ply because of the discontinuity of inter-laminar stresses. For a ply *k* of the laminated plate, this relationship, based on Hooke's Law and expressed with respect to the local coordinate system (1,2,3) (Figure 3.12) [92], is written:

$$\begin{Bmatrix} \sigma_1 \\ \sigma_2 \\ \tau_{12} \\ \tau_{23} \\ \tau_{13} \end{Bmatrix}^k = \begin{bmatrix} Q_{11} & Q_{12} & 0 & 0 & 0 \\ & Q_{22} & 0 & 0 & 0 \\ & & Q_{33} & 0 & 0 \\ & sym & & Q_{44} & 0 \\ & & & & Q_{55} \end{bmatrix} \begin{Bmatrix} \varepsilon_1 \\ \varepsilon_2 \\ \gamma_{12} \\ \gamma_{23} \\ \gamma_{13} \end{Bmatrix}^k \tag{3.26}$$

Where σ and τ represent the normal and shear stresses, respectively, ε and γ represent the corresponding normal and shear strains. The elastic constants Q, which relate stress to strain, are defined as follows:

$$Q_{11} = \frac{E_{11}}{1-\nu_{12}\nu_{21}}, \quad Q_{22} = \frac{E_{22}}{1-\nu_{12}\nu_{21}}, \quad Q_{12} = \frac{E_{11}\nu_{21}}{1-\nu_{12}\nu_{21}}, \; Q_{33} = G_{12}, \; Q_{44} = G_{23}, \quad Q_{55} = G_{13},$$

Where *E*, *G* and ν are, respectively Young's modulus, shear modulus and Poisson's ratio.

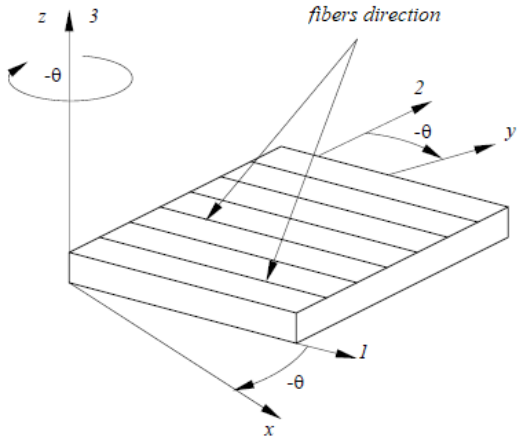

Figure 3.12: Transformation of the reference frame within a ply

Here, the *local coordinate system (1,2,3)* is defined as follows:

- *1-axis*: Longitudinal direction (parallel to the fibers).
- *2-axis*: Transverse direction (perpendicular to the fibers).
- 3-axis: Through-thickness direction.

To study the elastic behavior of a laminate, it is essential to express the stress-strain relationship (Equation 3.26) in the global coordinate system (*x*,*y*,*z*). This transformation is necessary because the global coordinate system aligns with the overall geometry of the laminate, whereas the local coordinate system (1,2,3) is specific to each ply's fiber orientation. By transforming Equation (3.26) into the global coordinate system, the relationship can be written as follows:

$$\begin{Bmatrix}\sigma_x\\ \sigma_y\\ \tau_{xy}\\ \tau_{yz}\\ \tau_{xz}\end{Bmatrix}^k = \begin{bmatrix}\bar{Q}_{11} & \bar{Q}_{12} & \bar{Q}_{13} & 0 & 0\\ & \bar{Q}_{22} & \bar{Q}_{23} & 0 & 0\\ & & \bar{Q}_{33} & 0 & 0\\ & sym & & \bar{Q}_{44} & 0\\ & & & & \bar{Q}_{55}\end{bmatrix} \begin{Bmatrix}\varepsilon_x\\ \varepsilon_y\\ \gamma_{xy}\\ \gamma_{yz}\\ \gamma_{xz}\end{Bmatrix}^k \tag{3.27}$$

$[\bar{Q}]$ is the stiffness matrix of a ply *k* expressed in the global coordinate system (*x*,*y*,*z*). It depends on its coefficients and the angle θ, which represents the fiber orientation:

$$\begin{aligned}
\bar{Q}_{11} &= Q_{11}\cos^4\theta + 2\left(Q_{12} + 2\,Q_{33}\right)\sin^2\theta\cos^2\theta + Q_{22}\sin^4\theta\\
\bar{Q}_{12} &= \left(Q_{11} + Q_{22} - 4\,Q_{33}\right)\sin^2\theta\cos^2\theta + Q_{12}\left(\sin^4\theta + \cos^4\theta\right)\\
\bar{Q}_{22} &= Q_{11}\sin^4\theta + 2\left(Q_{12} + 2\,Q_{33}\right)\sin^2\theta\cos^2\theta + Q_{22}\cos^4\theta\\
\bar{Q}_{13} &= \left(Q_{11} - Q_{12} + 2\,Q_{33}\right)\sin\theta\cos^3\theta + \left(Q_{12} - Q_{22} + 2\,Q_{33}\right)Q_{22}\sin^3\theta\cos\theta\\
\bar{Q}_{23} &= \left(Q_{11} - Q_{12} - 2\,Q_{33}\right)\sin^3\theta\cos\theta + \left(Q_{12} - Q_{22} + 2\,Q_{33}\right)Q_{22}\sin\theta\cos^3\theta\\
\bar{Q}_{33} &= \left(Q_{11} + Q_{22} - 2\,Q_{12} - 2\,Q_{33}\right)\sin^2\theta\cos^2\theta + Q_{33}\left(\sin^4\theta + \cos^4\theta\right)\\
\bar{Q}_{44} &= Q_{11}\cos^2\theta + Q_{55}\sin^2\theta\\
\bar{Q}_{45} &= \left(Q_{55} - Q_{44}\right)\cos\theta\sin\theta\\
\bar{Q}_{55} &= Q_{44}\sin^2\theta + Q_{55}\cos^2\theta
\end{aligned} \tag{3.28}$$

The variation in stresses through the laminate's thickness requires the stress–strain relationship to be expressed using stress resultants and moments. Integrating (3.27) through the plate's thickness allows the constitutive equation for the entire laminate to be expressed in terms of:

- membrane stress resultants:

$$R(x,y) = \begin{Bmatrix}R_x\\ R_y\\ R_{xy}\end{Bmatrix} = \sum_{k=1}^{N_L}\int_{z_{k-1}}^{z_k}\begin{Bmatrix}\sigma_x\\ \sigma_y\\ \tau_{xy}\end{Bmatrix}_k dz \tag{3.29}$$

- Bending and twisting moments:

$$M(x,y) = \begin{Bmatrix}M_x\\ M_y\\ M_{xy}\end{Bmatrix} = \sum_{k=1}^{N_L}\int_{z_{k-1}}^{z_k} z\begin{Bmatrix}\sigma_x\\ \sigma_y\\ \tau_{xy}\end{Bmatrix}_k dz \tag{3.30}$$

- Shear stress resultants (transverse shear resultant):

$$Q(x,y)=\begin{Bmatrix}Q_x\\Q_y\end{Bmatrix}=\sum_{k=1}^{N_L}\int_{z_{k-1}}^{z_k}\begin{Bmatrix}\tau_{xz}\\\tau_{yz}\end{Bmatrix}_k dz \tag{3.31}$$

where N_L represents the number of layers in the laminate.

By combining the equations (3.29), (3.30) and (3.31), the constitutive equation for the entire laminate is expressed as:

$$\begin{Bmatrix}R_x\\R_y\\R_{xy}\\M_x\\M_y\\M_{xy}\\Q_y\\Q_x\end{Bmatrix}=\begin{pmatrix}A_{11}&A_{12}&A_{13}&B_{11}&B_{12}&B_{13}&0&0\\&A_{22}&A_{23}&B_{12}&B_{22}&B_{23}&0&0\\&&A_{33}&B_{13}&B_{23}&B_{33}&0&0\\&&&D_{11}&D_{12}&D_{13}&0&0\\&&&&D_{22}&D_{23}&0&0\\&&sym&&&D_{33}&0&0\\&&&&&&F_{44}&F_{45}\\&&&&&&&F_{55}\end{pmatrix}\begin{Bmatrix}\varepsilon_{x0}\\\varepsilon_{y0}\\\varepsilon_{xy0}\\\kappa_x\\\kappa_y\\\kappa_{xy}\\\gamma_{yz}\\\gamma_{xz}\end{Bmatrix} \tag{3.32}$$

Its compact form is:

$$\begin{Bmatrix}R\\M\\Q\end{Bmatrix}=[C]\begin{Bmatrix}\varepsilon_0\\\kappa\\\gamma\end{Bmatrix} \tag{3.33}$$

With:

$$[C]=\begin{bmatrix}[A]&[B]&0\\[B]&[D]&0\\0&0&[F]\end{bmatrix} \tag{3.34}$$

In which [*A*] is the extension matrix, [*B*] is the coupling matrix and [*D*] is the bending matrix, their coefficients are defined as:

$$(A_{ij},B_{ij},D_{ij})=\sum_{k=1}^{N_L}\int_{z_{k-1}}^{z_k}(\bar{Q}_{ij})_k(1,z,z^2)dz \qquad i,j=1,2,3 \tag{3.35}$$

[*F*] is the shear matrix; their coefficients are defined as:

$$(F_{ij})=\alpha_{ij}\sum_{k=1}^{N_L}\int_{z_{k-1}}^{z_k}(\bar{Q}_{ij})_k\,dz \qquad i,j=1,2,3 \tag{3.36}$$

α_{ij} is the shear correction factor. Various values have been proposed (e.g., 2/3 by Timoshenko, 5/6 by Reissner, and $\pi^2/12$ by Mindlin), a value of 5/6 generally yields the best results [93].

3.7.4 Equation of motion

In the dynamic analysis of structures, Hamilton's principle is a powerful tool used to derive the equations of motion that govern the structure's behavior under dynamic loads. It provides an elegant and variational approach, offering an alternative to the more traditional force-based methods. Hamilton's principle states that the actual path or motion of a physical system between two points in time (t_1 and t_2) is the one that makes the action (S) stationary (typically a minimum).

The action (S) is defined as the time integral of the Lagrangian (L):

$$S = \int_{t_1}^{t_2} L dt \tag{3.37}$$

where $L = T - V$. T is the kinetic energy of the plate related the structure's motion, involving its mass distribution and velocity. V is the potential energy which includes strain energy and potential energy of the plate.

To extract the equation of motion from Hamilton's principle, we used the Euler-Lagrange equations [94]:

$$\frac{d}{dt}\left(\frac{\partial L}{\partial \dot{q}_r}\right) - \frac{\partial L}{\partial q_r} = 0 \qquad r = 1, 2, ..., R \tag{3.38}$$

R is the number of the degree of freedom of the plate.

The expression for the total potential energy V in the absence of work from external forces is:

$$V = \frac{1}{2}\int_{\Omega} \{\varepsilon\}^T \, d\Omega = \frac{1}{2}\int_{V} \{\varepsilon\}^T \underbrace{[C]\{\varepsilon\}}_{\{\sigma\}} dV \tag{3.39}$$

Where Ω is the plate surface.

$$\{\varepsilon\} = \begin{Bmatrix} \varepsilon_0 \\ \kappa \\ \gamma \end{Bmatrix}$$

While the expression of the kinetic energy T is:

$$T = \frac{1}{2}\int_{v}\left\{\dot{\delta}\right\}\rho\left\{\dot{\delta}\right\}dv \tag{3.40}$$

$\left\{\dot{\delta}\right\}$ is the velocity vector of a point *M (x, y, z)* of the laminate. $\left\{\dot{\delta}\right\}^T = \{\dot{u} \quad \dot{v} \quad \dot{w}\}$.

v and ρ are respectively, the volume and the density of the plate.

Integrating equation (3.40) over the thickness of the plate leads to writing:

$$T = \frac{1}{2}\int_{\Omega}\left\{\dot{\delta}\right\}^T\left[\bar{m}\right]\left\{\dot{\delta}\right\}d\Omega \tag{3.41}$$

Where $\left[\bar{m}\right]$ is the inertia matrix:

$$\left[\bar{m}\right] = \begin{bmatrix} I_0 & 0 & 0 & I_1 & 0 \\ 0 & I_0 & 0 & 0 & I_1 \\ 0 & 0 & I_0 & 0 & 0 \\ I_1 & 0 & 0 & I_2 & 0 \\ 0 & I_1 & 0 & 0 & I_2 \end{bmatrix} \tag{3.42}$$

In which: $I_i = \sum_{k=1}^{n}\int_{z_{k-1}}^{z_k} z^i\rho^k dz$, $i = 0,1,2$ and ρ^k is the material density of the kth layer.

Because a discrete plate is made up of separate parts, its total potential energy is the sum of the individual elementary potential energy of those parts:

$$V = \sum_{e=1}^{NE} V_e \tag{3.43}$$

NE is the number of elements.

Using the equation (3.39), the elementary potential energy is written as:

$$V_e = \frac{1}{2}\{\delta_e\}^T\left[K_e\right]\{\delta_e\} \tag{3.44}$$

[K_e] is the elementary stiffness matrix, it is given by the following relationship:

$$\left[K_e\right] = \int_{\Omega_e}\left[B\right]^T\left[C\right]\left[B\right]d\Omega_e \tag{3.45}$$

Ω_e is the surface of one element.

Similarly, the kinetic energy of the plate is the sum of all the elementary kinetic energies:

$$T = \sum_{e=1}^{NE} T_e \tag{3.46}$$

Using the equation (3.41), the elementary kinetic energy is written as:

$$T_e = \frac{1}{2}\{\dot{\delta}_e\}^T [M_e]\{\dot{\delta}_e\} \tag{3.47}$$

$[M_e]$ is the elementary mass matrix, its expression is given as follows

$$[M_e] = \int_{\Omega_e} [N]^T [\bar{m}][N] d\Omega_e \tag{3.48}$$

The element's Lagrange equation is obtained by substituting (3.44) and (3.47) into (3.38):

$$[M_e]\{\ddot{\delta}_e\} + [K_e]\{\delta_e\} = 0 \tag{3.49}$$

Where $\{\ddot{\delta}_e\}$ is the vector of elementary accelerations.

Relation (3.49) represents the equations of motion for a single element of the plate under the assumptions of no external forces and an undamped system; the global equations of motion are obtained using relations (3.43) and (3.46):

$$[M]\{\ddot{\delta}\} + [K]\{\delta\} = 0 \tag{3.50}$$

$\{\ddot{\delta}\}$: Vector of the global accelerations.

$\{\delta\}$: Vector of the global displacements.

$[M]$: Global mass matrix.

$[K]$: Global stiffness matrix.

For a harmonic motion, the displacement field $\{\delta\}$ can be considered as a solution of the equation of motion in the form:

$$\{\delta\} = \{\delta_0\} e^{i\omega t} \tag{3.51}$$

We arrive at the equation of motion by replacing terms in (3.50) with the expression from (3.51):

$$([K] - \omega^2 [M])\{\delta_0\} = 0 \tag{3.52}$$

3.7.4.1 Stiffness and mass matrices

The elementary stiffness matrices are defined by relations (3.45) and (3.21). They are symmetric of order 90 x 90, their form is given as follows:

$$\left[K^e\right]=\begin{bmatrix}\left[K_{ii}^e\right] & \left[K_{ij}^e\right]\\ \left[K_{ji}^e\right] & \left[K_{jj}^e\right]\end{bmatrix}=\begin{bmatrix}\int_{\Omega_e}\left[B_i\right]^T\left[C\right]\left[B_i\right]d\Omega & \int_{\Omega_e}\left[B_i\right]^T\left[C\right]\left[B_j^{'}\right]d\Omega\\ \int_{\Omega_e}\left[B_j^{'}\right]^T\left[C\right]\left[B_i\right]d\Omega & \int_{\Omega_e}\left[B_j^{'}\right]^T\left[C\right]\left[B_j^{'}\right]d\Omega\end{bmatrix} \tag{3.53}$$

Where $\left[K_{ii}^e\right]$ is the classical stiffness matrix. $\left[K_{ij}^e\right]$ and $\left[K_{ji}^e\right]$ are the coupling stiffness matrix and $\left[K_{jj}^e\right]$ is the enriched stiffness matrix.

The $\left[K_{ii}^e\right]$ submatrix within the elementary matrix is defined as follows:

$$\left[K_{ii}^e\right]=\begin{bmatrix}\left[K^{11}\right] & \left[K^{12}\right] & 0 & \left[K^{14}\right] & \left[K^{15}\right]\\ & \left[K^{22}\right] & 0 & \left[K^{24}\right] & \left[K^{25}\right]\\ & & \left[K^{33}\right] & \left[K^{34}\right] & \left[K^{35}\right]\\ & sym & & \left[K^{44}\right] & \left[K^{45}\right]\\ & & & & \left[K^{55}\right]\end{bmatrix} \tag{3.54}$$

The elements of the matrices [K^{ab}] (*a, b=1,2…5),* are expressed as:

$$\begin{aligned}
K_{ij}^{11} &= A_{11}S_{ij}^{\xi}+A_{16}\left(S_{ij}^{\xi\eta}+S_{ji}^{\xi\eta}\right)+A_{66}S_{ij}^{\eta}\\
K_{ij}^{12} &= A_{12}S_{ij}^{\xi\eta}+A_{16}S_{ij}^{\xi}+A_{26}S_{ij}^{\eta}+A_{66}S_{ij}^{\xi\eta}\\
K_{ij}^{14} &= B_{11}S_{ij}^{\xi}+B_{16}\left(S_{ij}^{\xi\eta}+S_{ji}^{\xi\eta}\right)+B_{66}S_{ij}^{\eta}\\
K_{ij}^{15} &= B_{12}S_{ij}^{\xi\eta}+B_{16}S_{ij}^{\xi}+B_{26}S_{ji}^{\eta}+B_{66}S_{ij}^{\xi\eta}\\
K_{ij}^{22} &= A_{22}S_{ij}^{\eta}+A_{26}\left(S_{ij}^{\xi\eta}+S_{ji}^{\xi\eta}\right)+A_{66}S_{ij}^{\eta}\\
K_{ij}^{24} &= B_{16}S_{ij}^{\xi}+B_{66}S_{ij}^{\xi\eta}+B_{12}S_{ji}^{\xi\eta}+B_{26}S_{ij}^{\eta}\\
K_{ij}^{25} &= B_{66}S_{ij}^{\xi}+B_{26}\left(S_{ij}^{\xi\eta}+S_{ji}^{\xi\eta}\right)+B_{22}S_{ij}^{\eta}\\
K_{ij}^{33} &= F_{44}S_{ij}^{\xi}+F_{45}\left(S_{ij}^{\xi\eta}+S_{ji}^{\xi\eta}\right)+F_{55}S_{ij}^{\eta}\\
K_{ij}^{34} &= F_{44}S_{ij}^{\xi 0}+B_{45}S_{ij}^{\eta 0}\\
K_{ij}^{35} &= F_{45}S_{ij}^{\xi 0}+F_{55}S_{ij}^{\eta 0}\\
K_{ij}^{44} &= D_{11}S_{ij}^{\xi}+D_{16}\left(S_{ij}^{\xi\eta}+S_{ji}^{\xi\eta}\right)+D_{66}S_{ij}^{\eta}+F_{44}S_{ij}^{0}\\
K_{ij}^{45} &= D_{12}S_{ij}^{\xi\eta}+D_{16}S_{ij}^{\xi}+D_{26}S_{ji}^{\eta}+D_{66}S_{ij}^{\xi\eta}+F_{45}S_{ij}^{0}\\
K_{ij}^{55} &= D_{66}S_{ij}^{\xi}+D_{26}\left(S_{ij}^{\xi\eta}+S_{ji}^{\xi\eta}\right)+D_{22}S_{ij}^{\eta}+F_{55}S_{ij}^{0}
\end{aligned} \tag{3.55}$$

With:

$$
\begin{aligned}
S_{ij}^{\xi\eta} &= \int_{-1}^{+1}\int_{-1}^{+1} \frac{\partial N_i}{\partial \xi}\frac{\partial N_j}{\partial \eta}\left|J\right| d\xi d\eta \\
S_{ij}^{00} &= S_{ij} \qquad\qquad (i, j = 1,...,n) \\
S_{ij}^{\xi\xi} &= S_{ij}^{\xi}
\end{aligned}
\tag{3.56}
$$

$\left|J\right|$ is the determinant of the Jacobian matrix.

The elementary mass matrix $\left[M^e\right]$ is giving by the following:

$$
\left[M^e\right] = \begin{bmatrix} \left[M_{ii}^e\right] & \left[M_{ij}^e\right] \\ \left[M_{ji}^e\right] & \left[M_{jj}^e\right] \end{bmatrix} = \begin{bmatrix} \int_{\Omega_e} \left[N_i\right]^T \left[\bar{m}\right]\left[N_i\right] d\Omega & \int_{\Omega_e} \left[N_i\right]^T \left[\bar{m}\right]\left[N_j^{'}\right] d\Omega \\ \int_{\Omega_e} \left[N_j^{'}\right]^T \left[\bar{m}\right]\left[N_i\right] d\Omega & \int_{\Omega_e} \left[N_j^{'}\right]^T \left[\bar{m}\right]\left[N_j^{'}\right] d\Omega \end{bmatrix}
\tag{3.57}
$$

Once the element matrices are calculated, we construct the global matrices. Then, to determine the vibrational responses of the structure, we solve the equation of motion (3.52). This often involves solving a standard eigenvalue problem, represented by equation (3.52). There are many ways to solve this eigenvalue problem, like Householder, Q-R, or subspace iteration. The best method depends on the matrices' properties and size. For large matrices, such as those found in structural analysis, subspace iteration is commonly used because it efficiently finds the smallest eigenvalues. This method iteratively transforms the matrices into a simpler, diagonal form, which facilitates the use of the Jacobi method.

3.8 Conclusion

This chapter detailed the application of the Extended Finite Element Method (XFEM) for vibration analysis of cracked plates. By using enrichment functions, XFEM efficiently models crack without remeshing. We derived the displacement and strain fields, formulated the XFEM system, and established the stiffness and mass matrices. This demonstrates XFEM's effectiveness for dynamic analysis of cracked structures, offering a robust tool for structural integrity assessments.

CHAPTER 4

FREE VIBRATION ANALYSIS OF CRCKED COMPOSITE PLATES REINFORCED WITH CNT's USING XFEM

4.1 Introduction

This chapter presents the results and discussion of a study on the free vibration of cracked composite plates reinforced with carbon nanotubes (CNTs). To achieve this, a MATLAB program was developed based on the extended finite element method (XFEM). This program accommodates both thick and thin plates, single or multiple layers, and various material types (isotropic, composite, or nanocomposite). It also allows for the modeling of single or multiple cracks at any location. The program's accuracy was validated through a comparative study. Subsequently, the free vibration behavior of CNT-reinforced composite (CNTRC) cracked plates was analyzed for different CNT distribution patterns (UD, FG-X, FG-O, FG-A, and FG-V). The modified Halpin-Tsai model was used to determine the effective elastic modulus, while the rule of mixture was employed for mass density and Poisson's ratio. Finally, a parametric study explored the influence of crack length, crack position, width-to-thickness ratios, CNT volume fraction, and power law index (P_{in}) on the natural frequencies of the CNTRC plate under various boundary conditions, providing valuable insights for different distribution patterns**.**

The boundary conditions for this study are presented in table 4.1.

Table 4.1: Boundary conditions combination

Boundary conditions	$y=0$	$x=L$	$y=W$	$x=0$
SSSS	S	S	S	S
CCCC	C	C	C	C
CSCS	C	S	C	S
CFCF	C	F	C	F

- **Simply supported edge (S):**

At $x = 0, L : u_0 = w_0 = \theta_y = 0$

At $y = 0, W : v_0 = w_0 = \theta_x = 0$

- **Clamped edge (C):**

On all edges $u_0 = v_0 = w_0 = \theta_x = \theta_y = 0$

- **Free edge (C):**

On all edges $u_0 = v_0 = w_0 = \theta_x = \theta_y \neq 0$

4.2 Isotropic homogenous plate

This section details the investigation into the free vibration behavior of a cracked isotropic homogeneous plate. The analysis of a square isotropic plate, with a thick to length ratio (*h/L)* of 0.001, was performed using a mesh of nine-node isoperimetric elements. The plate's material properties are $E=70\times10^9$ *Pa, v=0.3, and* $\rho=2700kg/m3$ [95]. To validate the methodology, the non-dimensional natural frequencies obtained for a square plate with a central crack and fully simply supported (SSSS) boundary conditions using XFEM, are compared with existing literature and presented in Table 4.2.

Table 4.2: Non-dimensional first five natural frequencies $\bar{\omega} = \omega\sqrt{\rho h/D}$, $D = \frac{Eh^3}{12(1-\upsilon^2)}$ of isotropic plate

Source of results	$\bar{a}$	Mode number				
		1	**2**	**3**	**4**	**5**
Stahl [96]	0.0	19.739	49.348	49.348	78.957	98.696
Liew [97]		19.74	49.35	49.35	78.96	98.70
Bachen [98]		19.739	49.348	49.348	78.955	98.698
Duc [99]		19.7393	49.350	49.3501	78.9641	98.7130
Present		19.7370	49.3508	49.3508	78.9477	98.7519
Stahl [96]	0.2	19.305	49.170	49.328	78.957	93.959
Liew [97]		19.38	49.16	49.31	78.81	94.96
Bachen [98]		19.305	49.181	49.324	78.945	93.893
Duc [99]		19.2734	49.252	49.3181	78.8544	93.8339
Present		19.333	49.1458	49.3305	78.9376	94.3482
Stahl [96]	0.4	18.279	46.624	49.032	78.602	85.510
Liew [97]		18.44	46.44	49.04	78.39	86.71
Bachen [98]		18.278	46.635	49.032	78.600	85.450
Duc [99]		18.2508	46.6033	49.0327	78.6611	85.9037
Present		18.3945	46.5996	49.0625	78.5774	86.5764
Stahl [96]	0.6	17.193	37.978	48.223	75.581	79.588
Liew [97]		17.33	37.75	48.26	75.23	80.32
Bachen [98]		17.180	37.987	48.214	75.579	79.556
Duc [99]		17.1936	38.0012	48.8601	78.2405	80.3774
Present		17.3615	38.0325	48.3240	75.5472	80.6430
Stahl [96]	0.8	16.403	27.779	47.256	65.732	76.371
Liew [97]		16.47	27.43	47.27	65.19	76.60
Bachen [98]		16.406	27.753	47.201	65.715	76.351
Duc [99]		16.4885	27.8042	48.7430	77.3879	77.7614
Present		16.5958	27.7715	47.4085	65.6772	76.5993

Notably, the presence of a crack has a direct impact on the dynamic properties of the plate. As evidenced in Table 4.2, the natural frequencies exhibit a decreasing trend with increasing crack length. Importantly, these results show excellent agreement with previous works.

4.3 Orthotropic plate

To further validate the methodology, we will also demonstrate its applicability to an orthotropic plate. Additionally, to evaluate the effectiveness of the current approach, we present a study involving two cases of CNTRC plates (with and without cracks), considering various CNT filler distributions and boundary conditions.

4.3.1 Virgin CNTRC plate

This study investigates a CNTRC plate with varying nanofiller volume fractions and fully simply supported boundary conditions. The plate under consideration possesses the following properties for the uniformly distributed (UD) CNT reinforcements [100], [101]: $E_{11} = 5646.6GPa$, $E_{22} = 7080GPa$, $G_{12} = 1944.5GPa$, $\rho_{CNT} = 1400kg/m^3$. For $f^*_{CNT} = 0.11$ The CNT efficiency parameters are taken as: $(\eta_1 = 0.149, \eta_2 = 0.934, \eta_3 = 0.934)$, for $f^*_{CNT} = 0.14$ $(\eta_1 = 0.15, \eta_2 = 0.941, \eta_3 = 0.941)$ and for $f^*_{CNT} = 0.17$ $(\eta_1 = 0.149, \eta_2 = 1.381, \eta_3 = 1.381)$.

The mechanical properties for the matrix are: $E_m = 2.1GPa$ $\upsilon_m = 0.34$, $\rho_m = 1150kg/m^3$.

Table 4.3: Non-dimensional first five natural frequencies $\left(\bar{\omega} = \omega(L^2/h)\sqrt{\rho_m/E_m}\right)$ of SSSS CNTRC plate with different values of nanofiller volume fraction

f^*_{CNT}	Source	Mode number				
		1	2	3	4	5
0.11	FSDT [102]	19.223	23.408	34.669	54.043	70.811
	Q9FPM [103]	19.1547	23.2703	34.038	51.9021	70.0233
	Duc [99]	19.1547	23.2683	34.0315	51.887	69.9971
	Present	19.1523	23.2433	34.0470	52.3616	70.0509
0.14	FSDT [102]	21.354	25.295	36.267	55.608	78.11
	Q9FPM [103]	21.3168	25.188	35.6672	53.4806	77.3941
	Duc [99]	21.3167	25.1859	35.6607	53.4656	77.3604
	Present	21.3141	25.1559	35.6571	53.9057	77.4167
0.17	FSDT [102]	23.697	28.865	42.667	67.475	87.385
	Q9FPM [103]	23.6071	28.8099	42.3671	64.7828	86.3904
	Duc [99]	23.6072	28.8076	42.3593	64.7646	86.3592
	Present	23.6043	28.7771	42.3825	65.3670	86.4261

To validate the findings of this study, the results are compared with those of Zhu et al [102], Wu et al [103], and Duc et al [99] who employed FSDT and FEM, the convergent finite prism method (FPM), and Shi's third-order theory (TSDT) coupled with phase field theory, respectively. The close agreement observed with these published references confirms the

reliability of the current results. Additionally, the study reveals that increasing the nanofiller volume fraction leads to a rise in the natural frequencies.

A comparative study was performed considering various carbon nanotube (CNT) filler distribution patterns: uniform distribution (UD), functionally graded X (FG-X), functionally graded O (FG-O), and functionally graded A (FG-A). Considering simply supported on all four sides (SSSS). The nanofiller volume fraction and the power law index values are respectively set at $f_{CNT}^{*} = 0.11$, and $Pin = 1$. $W/h = 10$; $N_l = 20$ and $L/W = 1$. The first five non-dimensional natural frequencies obtained from this study are presented in Table 4.3.

Table 4.4: Non-dimensional first five natural frequencies $\bar{\omega} = \omega(W^2/h)\sqrt{\rho_m / E_m}$ of CNTRC plate

Source of results	**Distribution**	**Mode number**				
		1	**2**	**3**	**4**	**5**
Zhu [102]	FG-O	11.550	16.265	19.499	19.499	26.513
Yasser [86]		11.593	16.245	19.477	19.477	26.138
Present		11.554	16.193	19.477	19.477	26.061
Zhu [102]	FG-V	12.452	17.060	19.499	19.499	27.340
Yasser [86]		12.478	17.023	19.477	19.477	26.957
Present		12.433	16.974	19.477	19.477	26.879
Zhu [102]	UD	13.532	17.700	19.449	19.449	27.569
Yasser [86]		13.564	17.669	19.427	19.427	27.194
Present		13.506	17.617	19.427	19.427	27.123
Zhu [102]	FG-X	14.616	18.646	19.499	19.499	28.519
Yasser [86]		14.653	18.614	19.477	19.477	28.132
Present		14.582	18.556	19.477	19.477	28.060

The results presented in Table 4.4 demonstrate excellent agreement with the findings reported in references [102] and [86]. Notably, the FG-X configuration exhibits higher rigidity compared to the other considered configurations: FG-O, FG-V, and UD.

4.3.2 FG-CNTRC cracked plate

This study investigates a unidirectional (UD) carbon nanotube-reinforced composite (CNTRC) square plate featuring a central crack and a width-to-thickness ratio *(W/h)* of 50. The analysis is conducted under various boundary conditions and crack lengths (0.0, 0.2, 0.4, 0.6, 0.8), with the power law index fixed at P_{in}=1. For comparison, the polymer matrix is epoxy, with an elastic

modulus of 2.9GPa, a mass density of 1200kg/m^3, and a Poisson's ratio of 0.35. The CNT volume fraction is 0.1, and their elastic and shear moduli are 1002GPa and 431GPa, respectively, with a mass density of 1800kg/m^3. The first five non-dimensional frequencies $(\bar{\omega} = \omega(L^2/h)\sqrt{\rho_m/E_m})$ obtained are presented in Table 4.5 and show good agreement with published results [99]. The findings indicate that the fully clamped (CCCC) plate exhibits the highest stiffness, followed by CFCF and CSCS, with the fully simply supported (SSSS) plate showing the lowest stiffness. This confirms the expected rigidity order (CCCC > CFCF > CSCS > SSSS). Furthermore, the natural frequencies are observed to decrease with increasing crack length.

Table 4.5: Non- dimensional first five natural frequencies with different length of the crack and different boundary conditions

Boundary Condition	$\bar{a}$	Source	Mode number				
			1	2	3	4	5
CCCC	0.0	Duc [99]	35.2758	60.4979	78.6019	95.3013	103.344
		Present	35.2740	60.5008	78.6165	95.2757	103.439
	0.2	Duc [99]	34.0929	59.6372	78.4502	95.2403	95.3575
		Present	34.0151	59.7899	78.5298	94.8449	95.3204
	0.4	Duc [99]	32.372	53.3383	77.6542	86.5979	94.5860
		Present	31.9543	54.3782	77.6570	85.0072	94.7627
	0.6	Duc [99]	31.3717	41.096	76.2747	82.4377	85.9975
		Present	30.6274	42.1109	76.0593	80.0360	85.7602
	0.8	Duc [99]	31.1032	32.9939	75.5274	80.1239	81.1802
		Present	30.2905	33.5923	74.9988	78.8082	81.1820
CSCS	0.0	Duc [99]	24.3879	54.6869	56.4368	77.9684	99.9443
		Present	24.3873	54.6996	56.6369	77.9506	100.062
	0.2	Duc [99]	23.1422	53.9495	56.3288	77.919	92.7202
		Present	22.9050	54.0834	56.3745	77.9022	91.2698
	0.4	Duc [99]	21.059	48.5024	55.6341	77.4162	84.0712
		Present	19.7080	49.4038	55.6972	77.2016	79.4980
	0.6	Duc [99]	19.2831	36.9387	54.0584	74.4508	79.4381
		Present	18.5727	38.0291	54.1555	75.1834	77.1103
	0.8	Duc [99]	18.2373	26.9028	52.3625	65.4198	77.3064
		Present	17.2269	28.0655	52.2591	67.4455	74.2886
CFCF	0.0	Duc [99]	19.1249	19.6401	36.9273	50.7509	50.0891
		Present	18.6420	19.1263	36.9229	50.1116	50.7728
	0.2	Duc [99]	18.133	19.1152	35.838	49.8415	50.7411
		Present	18.0761	19.1176	35.9426	49.9345	50.7682
	0.4	Duc [99]	17.0008	18.9996	34.5339	47.0501	50.6599
		Present	16.7360	18.9928	34.5555	47.9598	50.7043
	0.6	Duc [99]	15.6045	18.5402	34.0108	36.7397	50.0860
		Present	14.9888	18.4802	33.9637	38.7281	50.2549
	0.8	Duc [99]	14.2179	17.3632	26.4388	34.0019	47.2881
		Present	13.2069	17.1273	27.6370	33.9384	48.0131
SSSS	0.0	Duc [99]	17.3412	38.8809	53.5239	67.4351	77.9022
		Present	17.3410	38.8830	53.5289	67.4258	77.9447
	0.2	Duc [99]	16.6532	38.5319	53.4525	67.4037	72.2394
		Present	16.5579	38.5738	53.4943	67.3820	71.1071
	0.4	Duc [99]	15.4479	36.0161	53.0383	64.8399	67.1589
		Present	15.3974	37.4345	53.2128	63.6248	67.3744
	0.6	Duc [99]	14.3362	29.5459	52.0729	60.3074	65.7607
		Present	13.9672	30.9514	52.1822	58.2146	66.1350
	0.8	Duc [99]	13.6425	21.8979	50.9514	58.1174	60.8961
		Present	13.578	23.0670	50.9217	55.4714	60.1541

4.4 Parameter study

This section presents an investigation into the behavior of a CNTRC plate considering different crack lengths and positions within the *x*-*y* plane.

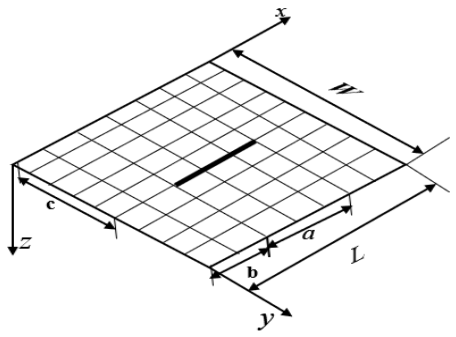

Figure 4.1: Geometry and sign convention

- $\bar{a} = a / L$ (Ratio of crack length along *x*-axis to the plate length)
- $\bar{b} = b / L$ (Ratio of crack position along *x*-axis to the plate length)
- $\bar{c} = c / W$ (Ratio of crack position along *y*-axis to the plate length)

The studied plate consists of an epoxy polymer matrix with an elastic modulus of E_m=*2.9GPa*, a mass density of *1200kg/m*^{3}, and a Poisson's ratio of *0.35*. Carbon nanotubes (CNTs) are incorporated with a volume fraction (f^*_{CNT}) of 0.1 and a power law index (*Pin*) of 1. The CNTs possess an elastic modulus (E_{CNT}) of 1002GPa, a shear modulus (G_{CNT}) of 431.9GPa, and a mass density of 1800kg/m^3. The natural frequencies are presented in non-dimensional form ($\bar{\omega} = \omega(L^2/h)\sqrt{\rho_m / E_m}$) . The plate, with a length of 1 meter, is composed of 20 layers (N_L=*20*) of equal thickness, considering various nanofiller distributions (UD, FG-X, FG-O, FG-A).

4.4.1 Effect of crack length

This application considers a CNTRC square plate with the same material properties as described previously, but subjected to different boundary conditions (CCCC, CSCS, CFCF, SSSS) and varying central crack lengths $\bar{a} = (0, 0.2, 0.4, 0.6, 0.8)$. The crack's configuration, running through the center of the plate, is illustrated in Figure 4.2.

Table 4.6: Non-dimensional natural frequencies of CNTRC plate with different distribution patterns, different lengths of crack and different boundary conditions

Boundary Condition	$\bar{a}$	Distribution			
		FG-X	UD	FG-A	FG-O
CCCC	0.0	42.190	35.275	30.387	26.512
	0.2	40.586	34.015	29.278	25.653
	0.4	37.995	31.934	27.353	24.212
	0.6	36.306	30.627	26.028	23.284
	0.8	35.871	35.871	25.637	23.044
CSCS	0.0	29.286	24.387	22.019	18.416
	0.2	27.624	22.905	20.909	17.564
	0.4	24.591	19.708	18.769	15.952
	0.6	21.785	18.572	16.765	14.490
	0.8	20.028	17.226	15.528	13.586
CFCF	0.0	22.428	18.642	16.184	14.066
	0.2	21.680	18.076	15.685	13.692
	0.4	19.918	16.736	14.432	12.799
	0.6	17.598	14.988	12.714	11.694
	0.8	15.235	13.206	10.889	10.469
SSSS	0.0	20.907	17.341	16.797	13.010
	0.2	20.025	16.670	16.061	12.569
	0.4	18.273	15.327	14.640	11.672
	0.6	16.470	13.967	13.269	10.779
	0.8	15.248	13.057	12.398	10.191

Table 4.6 reveals that crack length, boundary conditions, and nanofiller distribution patterns significantly influence the frequency parameter and the plate's stiffness. Specifically, the clamped-clamped-clamped-clamped (CCCC) plate exhibits the highest stiffness, while the simply supported (SSSS) plate demonstrates the lowest. Across all boundary conditions, the functionally graded X (FG-X) distribution yields the greatest stiffness, and the functionally graded O (FG-O) distribution results in the least. Furthermore, an inverse relationship is observed between crack length and natural frequencies: as the crack length increases, the frequencies decrease.

4.4.2 Effect of crack position

4.4.2.1 Effect of position crack ratio $\bar{b}$:

This section investigates the effect of crack position

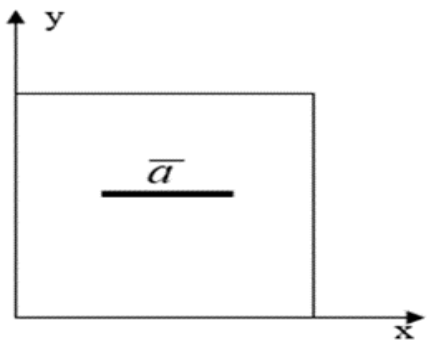

Figure 4.2: plate with central crack

along the *x-axis* ($\bar{b}$) on a clamped-free-clamped-free (CFCF) CNTRC plate, while keeping the crack length ($\bar{a} = 0.6$) and its position along the *y-axis* ($\bar{c} = 0.5$) constant. Table 4.7 illustrates how the free vibration parameter is influenced by both the crack's *x-axis* position ($\bar{b}$) and its length-to-thickness ratio (*L/h*). When the crack is located at the plate's edge along the *x-axis*, the natural frequencies decrease due to the free boundary conditions on the left and right sides, which reduce the overall stiffness. Notably, increasing the *L/h* ratio leads to an increase in the free vibration parameter across all distribution patterns, with FG-X exhibiting the highest stiffness and FG-O the lowest. Figure 4.3 visually depicts the crack's appearance in different positions (central and un-center).

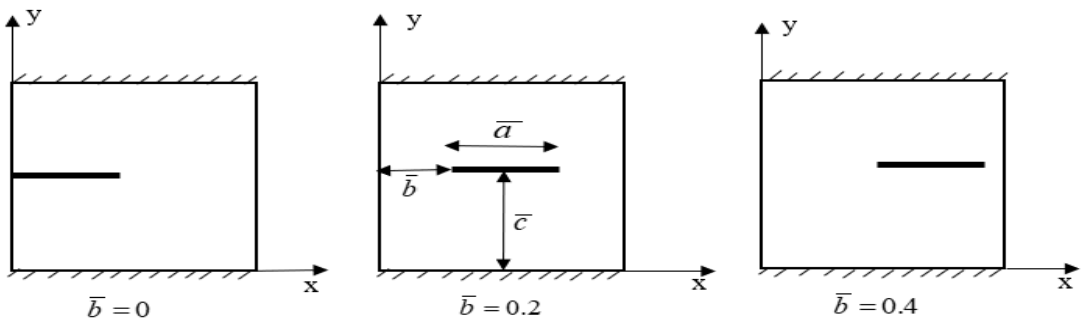

Figure 4.2: CFCF plate with crack: varying x-axis position

Table 4.7 : Non-dimensional first five natural frequencies of CFCF cracked CNTRC plate with various crack positions along x-axis and (L/h) ratios.

L/h			**Modes Number**				
	Distribution	$\bar{b}$	**1**	**2**	**3**	**4**	**5**
L/h=10	FG-X	0.0	10.369	14.373	18.461	20.062	28.805
		0.2	12.229	14.302	20.103	21.984	28.603
		0.4	10.607	14.390	18.483	20.062	28.893
	UD	0.0	9.745	13.217	17.487	19.986	25.995
		0.2	11.259	13.177	20.027	20.611	25.782
		0.4	9.881	13.225	17.503	19.986	26.055
	FG-A	0.0	7.993	12.233	16.704	20.035	23.360
		0.2	9.889	12.224	19.521	20.078	23.116
		0.4	8.194	12.245	16.738	20.035	23.437
	FG-O	0.0	8.550	11.356	16.002	20.062	21.590
		0.2	9.628	11.381	18.484	20.103	21.376
		0.4	8.590	11.358	16.012	20.062	21.622
L/h=20	FG-X	0.0	12.202	19.241	28.948	36.801	40.124
		0.2	12.229	14.302	20.103	21.984	28.603
		0.4	12.370	19.264	28.994	36.906	40.124
	UD	0.0	11.199	16.705	26.448	31.625	39.972
		0.2	11.259	13.177	20.027	20.611	25.782
		0.4	11.174	16.718	26.482	31.695	39.972
	FG-A	0.0	9.028	14.860	24.478	27.664	37.687
		0.2	9.889	12.224	19.521	20.078	23.116
		0.4	9.104	14.878	24.547	27.734	37.690
	FG-O	0.0	9.477	13.313	22.650	24.772	34.082
		0.2	9.628	11.381	18.484	20.103	21.376
		0.4	9.486	13.318	22.673	24.807	34.083
L/h=50	FG-X	0.0	13.484	21.997	40.831	41.695	59.543
		0.2	17.598	22.002	40.716	45.264	59.599
		0.4	13.555	22.024	41.110	41.160	40.601
	UD	0.0	12.078	18.430	34.387	35.640	50.162
		0.2	14.988	18.480	33.963	38.728	50.254
		0.4	12.140	18.449	34.540	35.614	50.163
	FG-A	0.0	9.772	16.085	29.732	31.645	43.970
		0.2	12.717	16.192	29.304	34.207	44.108
		0.4	9.894	16.109	29.888	31.655	43.971
	FG-O	0.0	9.959	14.139	26.197	28.098	38.531
		0.2	11.649	14.257	25.794	30.236	38.701
		0.4	10.004	14.150	26.261	28.102	38.531

4.4.2.2 Effect of position crack ratio $\bar{c}$

This section investigates the influence of crack position along the *y-axis* ($\bar{c}$) on a plate with a fixed crack length ($\bar{a} = 0.6$) and a fixed *x-axis* position ($\bar{b} = 0.5$), maintaining a width-to-

thickness ratio (*W/h*) of 50. Table 4.8 presents the non-dimensional frequencies for various boundary conditions. For CCCC plates, un-central cracks at $\overline{c}$ =0.1 and $\overline{c}$ =0.8 yield the highest frequencies across all distributions, while a central crack ($\overline{c}$ =0.3 and $\overline{c}$ =0.5) results in the lowest, indicating increased stiffness as the crack approaches a clamped edge. A similar trend is seen for SSSS plates in UD, FG-A, and FG-O distributions, where cracks near the simply supported edge increase stiffness; however, this is not the case for FG-X, where central cracks exhibit the highest frequencies. In contrast, CFCF plates show a different behavior: frequencies are lowest when the crack is near the free edges and highest when centrally located and distant from these edges, regardless of the distribution pattern.

Table 4.8 : Non dimensional first five natural frequencies of cracked CNTRC plate with various crack positions along y-axis and different boundary conditions.

Boundary conditions	**Distribution**		**Modes Number**				
	$\overline{c}$		**1**	**2**	**3**	**4**	**5**
CCCC	FG-X	0.1	38.497	51.328	87.222	91.538	106.458
		0.3	37.949	55.498	68.602	90.587	103.166
		0.5	17.598	22.002	40.716	45.264	059.599
		0.8	38.520	54.234	91.580	96.114	104.176
	UD	0.1	32.267	43.654	73.875	77.965	91.141
		0.3	31.932	47.229	58.685	77.164	88.257
		0.5	14.988	18.480	33.963	38.728	50.254
		0.8	32.322	46.163	77.975	82.125	89.114
	FG-A	0.1	27.719	38.126	64.457	67.502	79.783
		0.3	27.365	40.564	51.751	66.822	77.029
		0.5	12.717	16.192	29.304	34.207	44.108
		0.8	27.775	40.092	67.493	71.156	77.778
	FG-O	0.1	24.255	33.836	57.111	59.441	70.433
		0.3	24.161	36.657	45.955	58.895	68.296
		0.5	11.649	14.257	25.794	30.236	38.701
		0.8	24.337	35.801	59.432	64.244	68.997
SSSS	FG-X	0.1	8.174	23.059	51.354	63.836	74.308
		0.3	16.796	32.713	54.876	62.937	74.785
		0.5	16.470	36.469	62.583	68.348	78.679
		0.8	16.431	30.080	54.481	63.294	73.910
	UD	0.1	15.422	24.253	49.718	53.241	63.614
		0.3	14.360	27.968	47.100	52.491	62.966
		0.5	13.967	30.951	52.182	58.214	66.135
		0.8	14.222	26.150	47.170	52.771	62.366
	FG-A	0.1	13.755	19.581	42.000	45.558	55.448
		0.3	13.619	24.606	41.884	44.901	54.880

		0.5	13.269	27.644	44.589	50.617	57.595
		0.8	13.195	22.859	41.678	45.115	54.366
		0.1	12.244	21.559	39.697	42.977	48.948
	FG-O	0.3	11.160	21.955	37.033	39.069	48.090
		0.5	10.779	23.942	38.967	45.477	50.257
		0.8	11.120	20.976	37.540	39.386	47.731
FCFC		0.1	30.002	32.987	33.012	43.967	61.235
	FG-X	0.3	33.776	34.006	34.596	49.221	66.663
		0.5	33.769	34.003	34.207	49.461	86.913
		0.8	30.638	33.940	34.100	46.008	62.204
		0.1	28.044	28.318	31.062	36.888	59.075
	UD	0.3	28.201	28.400	29.963	42.567	56.866
		0.5	28.217	28.437	29.156	42.314	73.820
		0.8	28.190	28.447	28.635	40.333	53.999
		0.1	13.439	24.022	24.370	30.370	48.865
	FG-A	0.3	23.947	24.193	25.580	36.909	50.054
		0.5	23.964	24.234	24.815	37.195	63.639
		0.8	22.535	24.030	24.315	34.217	47.444
		0.1	20.916	21.217	26.191	33.771	55.965
	FG-O	0.3	23.947	24.193	25.580	36.909	50.054
		0.5	20.917	21.260	22.728	33.040	55.961
		0.8	20.926	21.287	23.475	32.917	43.814

4.4.3 Effect of the power law index *Pin*

This section details the computed natural frequencies of a clamped-free-clamped-free (CFCF) cracked CNTRC plate. These calculations assumed a crack length of $\bar{a} = 0.6$, a length-to-thickness ratio (*W/h*) of 50, and a carbon nanotube volume fraction (f_{CNT}^{*}) of 0.11. The results presented in Table 4.9 indicate that increasing the power law index leads to an increase in natural frequencies for the FG-X distribution pattern, but a decrease for the FG-A and FG-O patterns. This behavior can be attributed to the varying CNT filler concentrations: a higher power law index results in greater CNT concentration at the middle surface for FG-O, at the bottom surface for FG-A, and at both the top and bottom surfaces for FG-X. These observations highlight that the influence of Pin is strongly dependent on how the CNTs are distributed across the plate thickness, and each distribution responds differently as Pin varies.

Table 4.9: Non-dimensional first five natural frequencies of CFCF cracked CNTRC plate with various power law index

Pin		Modes Number				
		1	**2**	**3**	**4**	**5**
	distribution					
0.4	FG-X	16.876	21.011	38.814	43.515	57.022
	UD	15.530	19.195	35.336	40.132	52.194
	FG-A	14.631	18.172	33.313	38.177	49.463
	FG-O	13.890	17.055	31.223	35.989	46.416
0.8	FG-X	17.855	22.362	41.401	45.960	60.568
	UD	15.303	19.195	35.336	40.132	52.194
	FG-A	13.592	17.187	31.285	36.249	46.833
	FG-O	12.580	15.401	28.026	32.651	41.884
1	FG-X	18.256	22.920	42.471	46.956	62.024
	UD	15.530	19.195	35.336	40.132	52.194
	FG-A	13.069	16.755	30.362	35.383	45.679
	FG-O	12.041	14.735	26.729	31.268	40.042
1.4	FG-X	18.933	23.872	44.297	48.635	64.489
	UD	15.530	19.195	35.336	40.132	52.194
	FG-A	11.996	16.009	28.700	33.861	43.694
	FG-O	11.146	13.647	24.596	28.958	37.012
1.8	FG-X	19.492	24.660	45.812	50.010	66.519
	UD	15.530	19.195	35.336	40.132	52.194
	FG-A	10.793	15.396	27.227	32.584	42.080
	FG-O	10.436	12.802	22.921	22.921	27.111

4.5 CNTRC vs Carbon/epoxy plates

To establish the necessary fiber volume fraction in a traditional composite for equivalent stiffness to a nanocomposite, we conducted a comparative study. This investigation contrasted the performance of a four-layered, fully simply supported square carbon/epoxy composite plate ($200\times200\times4mm^3$) with that of a carbon nanotube (CNT)-reinforced nanocomposite plate, under varying crack lengths $(\bar{a}=0,0.4,0.8)$. The properties of the carbon fiber are $E_f=390GPa$, $G_f=20GPa$, $\nu=0.35$ and $\rho=1800Kg/m^3$.

Table 4.10: First Natural frequencies (Hz) for different volume fraction of Carbon/epoxy plate.

$\bar{a}$	Fiber volume fraction (%)	Carbon/epoxy	CNTs/epoxy FG-X	CNTs/epoxy UD
0.0	11	387.12	540.21	446.97
	14	404.09	604.07	496.50
	17	420.41	662.18	541.07
	20	436.12		
	22	446.93		
	32.5	496.48		
	42.5	540.25		
	42.7	541.10		
	58.5	604.12		
	60	610.69		
	65	629.99		
	73.3	662.20		
0.4	11	386.13	470.95	394.17
	12,4	394.14	-	-
	14	403.11	522.98	435.24
	17	419.42	570.19	471.92
	20	435.12		
	27.2	470.75		
	27.4	471.79		
	38.7	522.84		
	50.1	570.20		
0.8	11	384.61	390.91	334.35
	12.1	390.92	-	-
	14	401.59	427.50	364.63
	17	417.90	460.19	390.91
	18.8	427.38		
	25.3	460.13		

Table 4.10 shows that 17% CNT reinforcement maximizes the frequency of both cracked and un-cracked CNTRC plates (UD and FG-X). Matching this stiffness requires significantly higher fiber volume fractions in classical composites: 42.7% (UD) and 73.3% (FG-X).

For a crack length of $\bar{a}$ =0.4, the equivalent classical composite fiber volume fraction reduces to 27% (UD) and 50.1% (FG-X). At $\bar{a}$ =0.8, the FG-X equivalent drops to 25.3%, and UD-CNTRC becomes less stiff than the classical composite.

The CNTRC plate exhibits a greater sensitivity to crack presence and length, experiencing a more substantial drop in natural frequencies compared to the traditional composite.

4.6 Conclusion

This chapter presented a comprehensive analysis of the free vibration behavior of cracked CNT-reinforced composite plates using the XFEM-based MATLAB code developed in this work. The validation study confirmed the accuracy and robustness of the implemented formulation for different plate types, layer configurations, and crack scenarios. The investigation demonstrated that CNT distribution patterns strongly affect the stiffness and, consequently, the natural frequencies of cracked CNTRC plates. The results also highlighted the significant influence of crack length, crack location, geometric ratios, CNT volume fraction, and the power-law index on the vibrational response under various boundary conditions. Overall, the parametric study provided valuable physical insights into how damage and functional grading interact within multilayer CNT-reinforced laminates.

CHAPTER 5

EFFECT OF CNT REINFORCEMENT ON THE FREE VIBRATION BEHAVIOR OF CRACKED MULTILAYER LAMINATED COMPOSITE

5.1 Introduction

This chapter extends the investigation to the free vibration behavior of cracked laminated composite plates reinforced with carbon nanotubes (CNTs). Utilizing the established MATLAB program based on the extended finite element method (XFEM), this analysis now focuses on multi-layered structures. Here, we explore the dynamic characteristics of cracked laminated CNT-reinforced composite (CNTRC) plates, considering the combined influence of various CNT distribution patterns within each layer (UD, FG-X, FG-O, FG-A, and FG-V) and different stacking sequences. The effective elastic modulus, mass density, and Poisson's ratio of each CNT-reinforced ply are determined using the rule of mixture. A comprehensive parametric study is then conducted to analyze the effects of crack length, crack position, width-to-thickness ratios, CNT volume fraction, and the power law index (Pin) on the natural frequencies of these laminated CNTRC plates under various boundary conditions and stacking configurations. This chapter aims to provide novel insights into the dynamic response of cracked laminated nanocomposite structures, highlighting the crucial role of both intra-ply CNT distribution and inter-ply arrangement in their vibrational behavior.

The mechanical behavior of a laminated composite plate reinforced with functionally graded carbon nanotubes (FG-CNTs) is significantly affected by the CNT configuration and the arrangement, or stacking sequence, of its n constituent plies. This study investigates such plates, which have dimensions of thickness (h), width (W), and length (L), and are composed of plies each containing N_L finer layers (thickness $h/(n \cdot N_L)$). The CNTs within each ply are distributed according to five distinct patterns (FG-V, FG-A, FG-O, FG-X, and UD), visually represented in Figure 5.1. The variation in CNT volume fraction through the N_L layers of each ply is a key consideration. Figure 5.2 provides examples of common stacking sequences: (a) Cross-ply, with alternating 0° and 90° CNT ply orientations, and (b) Angle-ply, where CNT plies are oriented at ±45°.

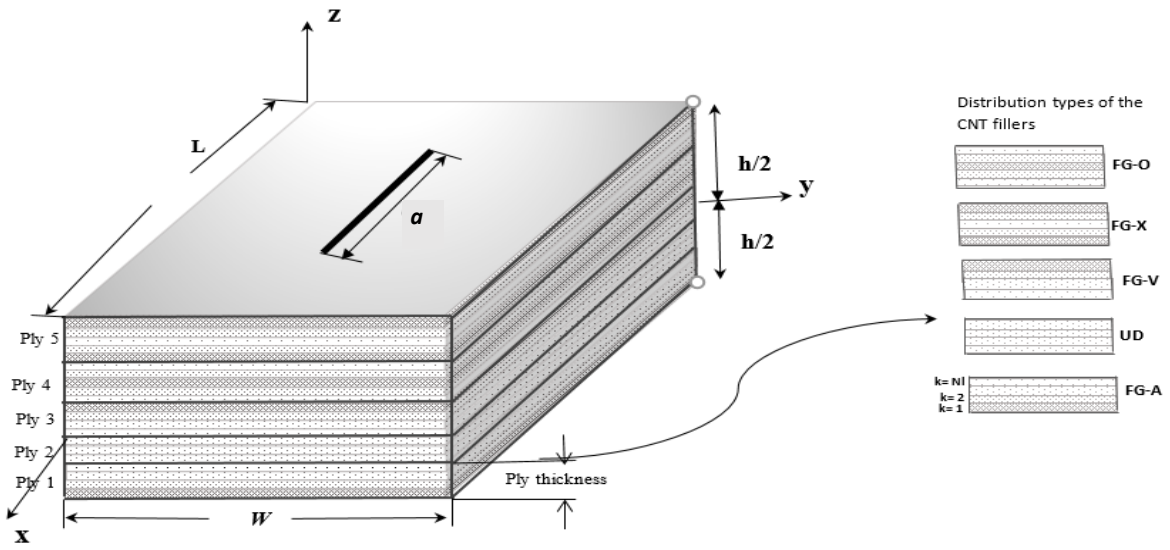

Figure 5.1: Laminated Composite Plate with Functionally Graded Carbon Nanotubes (FG-CNTs)

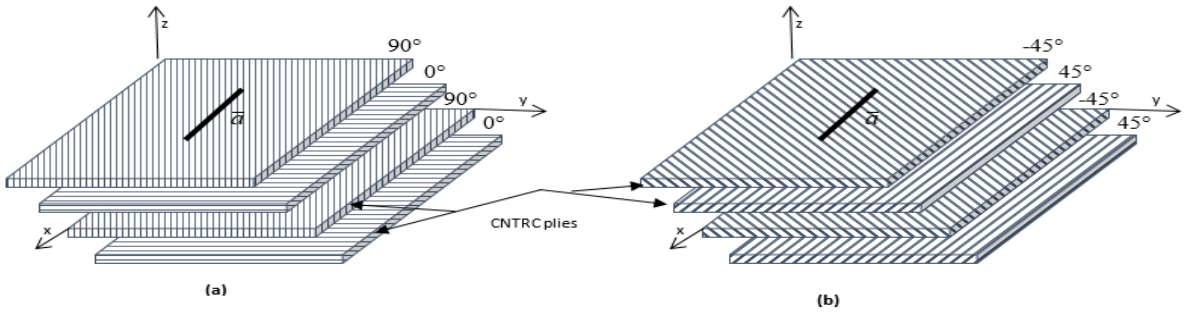

Figure 5.2: Examples of Stacking Sequences in Laminated Composite Plates: (a) Cross-ply (0°/90°), (b) Angle-ply (45°/-45°)

A comprehensive parametric study explored the combined effects of laminated plate configuration and carbon nanotube (CNT) distribution on the free vibration of cracked laminated plates. This investigation varied crack lengths, CNT volume fractions, geometric parameters, stacking sequences, ply numbers, and boundary conditions. The matrix material was poly(methyl vinyl pyrrolidone) (PMVP) with properties $E_m = 2.1GPa$, $\upsilon_m = 0.34$, and $\rho_m = 1150kg/m^3$. The CNTs had properties, $E_{11} = 5646.6GPa$, $E_{22} = 7080GPa$, $G_{12} = 1944.5GPa$,

$\rho_{CNT} = 1400 kg/m^3$ and $\upsilon_{12}^{CNT} = 0.175$. Table 5.1 provides CNT efficiency parameters for different volume fractions. The non-dimensional frequency parameter $\left(\bar{\omega} = \omega(L^2/h)\sqrt{\rho_m/E_m}\right)$ was calculated for square plates ($L=W$) with a through-the-thickness central crack, with the power-law index (*Pin*) set to 1.

Table 5.1: Effect of CNT Volume Fraction f_{CNT}^* on CNT Efficiency Parameter in Laminated Composite Plates.

f_{CNT}^*	0.11	0.14	0.17
η_1	0.149	0.150	0.149
η_2	0.934	0.941	1.381
η_3	0.934	0.941	1.381

5.2 Comparative study

This section presents a comparative study of the free vibration results obtained from our numerical investigation of virgin laminated carbon nanotube reinforced composite (CNTRC) plates. Our findings will be rigorously compared against established literature to assess the accuracy and reliability of our model. This comparison, highlighting both agreements and discrepancies with existing results for similar configurations and boundary conditions, aims to validate our model and identify potential avenues for future research or improvement.

Table 5.2: Comparisons of the first six non-dimensional frequencies of cross ply (0°/90°/0°/90°/0°) laminated CNTRC plates with two types of boundary conditions (*L/W=1, W/h=10)*

BC	Source of results		Mode number 1	2	3	4	5	6
SSSS	Reference [87]		14.383	19.463	19.468	27.318	30.704	38.526
	Chiker [58]	FG-X	14.276	19.257	19.257	26.882	30.415	37.050
	Present		14.934	19.476	19.476	28.481	3 2.680	38.951
	Reference [87]		14.241	19.463	19.468	27.026	30.602	38.296
	Chiker [58]	FG-V	14.118	19.253	19.253	26.536	30.276	37.016
	Present		14.781	19.477	19.477	28.148	32.563	38.952
	Reference [87]		14.277	19.414	19.419	27.098	30.579	38.312
	Chiker [58]	UD	14.170	19.208	19.208	26.654	30.288	36.956
	Present		14.823	19.427	19.427	28.237	32.545	38.237
	Reference [87]		14.207	19.463	19.468	26.955	30.578	37.240
	Chiker [58]	FG-O	14.096	19.257	19.257	26.497	30.278	37.048
	Present		14.744	19.476	19.476	28.067	32.535	38.951
CCCC	Reference [87]		19.784	31.074	32.862	40.732	46.552	49.369
	Chiker [58]	FG-X	19.878	30.895	32.974	40.051	45.639	48.231
	Present		19.618	31.029	33.690	41.517	46.710	49.874
	Reference [87]		19.678	30.902	32.773	40.585	46.324	49.294
	Chiker [58]	FG-V	19.758	30.681	32.678	39.839	45.369	48.128
	Present		19.481	30.794	33.576	41.319	46.399	49.875
	Reference [87]		19.680	30.906	32.736	40.554	46.315	49.209
	Chiker [58]	UD	19.771	30.772	32.664	39.868	45.407	48.071
	Present		19.500	30.828	33.551	41.312	46.428	49.748
	Reference [87]		19.652	30.862	32.752	40.549	46.270	49.277
	Chiker [58]	FG-O	19.737	30.666	32.672	39.848	45.361	48.130
	Present		19.447	30.734	33.547	41.268	46.321	49.874

Table 5.2 compares the first six non-dimensional frequency parameters for square cross-ply (0°/90°/0°/90°/0°) CNTRC laminated plates under two boundary conditions (CCCC and SSSS) and four CNT distribution patterns (UD, FG-X, FG-V, and FG-O). The CNT volume fraction and width-to-thickness ratio are fixed at 0.11 and 10, respectively. The results presented demonstrate very good agreement.

Table 5.3: Comparison of non-dimensional frequencies of cross-ply $(0°/90°)_n$ and angle ply $(45°/-45°)_n$ laminated SSSS CNTRC plates with different number of layers for $L/W = 1$, $W/h = 50$, $N_L = 20$ and $f_{CNT}^{*} = 0.11$

Stacking sequences	*n*	Distribution	Ref [104]	Chiker [58]	Present
$(0°/90°)_n$	1	FG-X	13.064	13.092	13.098
	2		17.975	17.985	18.001
	4		18.995	18.995	19.020
	1	UD	11.348	11.341	11.345
	2		17.714	17.688	17.704
	4		18.958	18.922	18.932
	1	FG-V	10.056	10.134	10.136
	2		17.495	17.510	17.528
	4		18.883	18.884	18.910
	1	FG-O	09.182	09.156	09.281
	2		17.378	17.495	17.412
	4		18.856	18.883	18.883
$(45°/-45°)_n$	1	FG-X	17.697	17.653	17.662
	2		24.601	24.550	24.571
	4		26.012	25.951	25.982
	1	UD	15.109	15.094	15.103
	2		24.180	24.134	24.154
	4		28.912	25.85	25.848
	1	FG-V	14.116	13.189	13.968
	2		23.946	23.870	24.005
	4		25.871	25.793	25.851
	1	FG-O	11.974	12.116	12.004
	2		23.761	23.946	23.741
	4		25.818	25.871	25.790

To validate the current findings, Table 5.3 compares the non-dimensional fundamental frequency parameters of simply supported square CNTRC laminated plates against the results reported by Chiker [58] and in Ref [104]. This comparison examines three different numbers of layers (*n=1,2,4*) and two stacking sequences: cross-ply (0°/90°) and angle-ply (45°/-45°), for a CNT volume fraction of *0.11* and a width-to-thickness ratio of *10*. The good agreement shown in the table supports the accuracy of the present results.

Table 5.4 concludes the comparative study by presenting the first six non-dimensional frequencies for simply supported square plates, focusing on the influence of laminated configurations with different numbers of cross-ply (0°/90°) plies. The excellent agreement observed with the results of Chiker et al [58]. validates the current findings. For n=1, the highest fundamental frequency is achieved with the $[X\text{-}X]_n$ arrangement, and the lowest with $[V\text{-}A]_n$.

However, for *n=2* and *n=4*, the $[A\text{-}V]_n$ stacking sequence results in the highest fundamental frequency, while [V-A]n leads to the lowest. Based on this analysis of plates with 4, 8, and 12 plies, it is suggested that optimal structural performance for CNTRC laminated plates is obtained by employing an A-type FG distribution in the bottom half and a V-type FG distribution in the top half, with a concentration of CNTs on the outermost surfaces of the plies.

Table 5.4: Comparison of first six non-dimensional frequencies of SSSS cross-ply (0°/90°) CNTRC laminated composite plates with various plate configuration (*L/W=1, W/h=50)*

Source of results		Mode number 1	2	3	4	5	6
Chiker [58]	[A-V]	10.425	29.301	29.353	41.145	63.382	63.672
Present		10.432	29.231	29.232	41.219	62.242	62.224
Chiker [58]	[V-A]	09.721	26.981	27.005	38.439	58.134	58.271
Present		09.715	26.891	26.891	38.471	57.015	57.015
Chiker [58]	[X-X]	13.092	36.911	36.958	51.394	79.461	79.714
Present		13.098	36.808	36.810	51.481	78.028	78.033
Chiker [58]	[A-A-V-V]	19.912	55.691	55.738	76.508	97.336	97.336
Present		19.993	55.590	55.591	76.806	97.380	97.385
Chiker [58]	[V-V-A-A]	15.124	42.557	42.597	58.986	90.938	91.140
Present		15.135	42.483	42.483	59.205	89.533	89.533
Chiker [58]	[X-X-X-X]	17.985	50.482	50.527	69.550	97.334	97.334
Present		18.001	50.394	50.394	69.819	97.384	97.384
Chiker [58]	[A-A-A-A-V-V-V-V]	20.005	55.881	55.908	76.736	97.324	97.324
Present		20.021	55.817	55.818	77.135	97.382	102.240
Chiker [58]	[A-A-A-A-V-V-V-V]	17.789	49.915	49.940	68.773	97.324	97.324
Present		17.811	49.861	46.862	69.131	97.382	102.228
Chiker [58]	[X-X-X-X-X-X-X-X]	18.995	53.194	53.220	73.148	97.322	97.322
Present		19.019	53.153	53.136	73.529	97.380	102.234

5.3 Free vibration of cracked laminated CNTRC plates

After the initial validation phase, the numerical investigation extends to the analysis of laminated composite plates containing centrally located cracks. The purpose of this stage is to evaluate the impact of these cracks on the plates' free vibration behavior. Throughout this section, the material and geometric properties of the plates remain constant: a CNT volume fraction (f^*_{CNT} =0.11), 20 layers (*n=20*), a square shape (*L/W=1*), and a high Width to thick ratio (*W/h*=50). The study will focus on how the introduction and variation in size of these central

cracks affect the non-dimensional frequencies $\left(\bar{\omega} = \omega(L^2/h)\sqrt{\rho_m/E_m}\right)$ of the laminated composite plates, allowing for generalized comparisons.

Table 5.5: The first five non-dimensional frequencies of cross ply (0°/90°/0°/90°/0°) laminate CNTRC plates with two types of boundary conditions and various length of the crack *(L/W=1, W/h=50)*

BC	Crack length $\bar{a}$		Mode number				
			1	2	3	4	5
SSSS	0.0	FG-X	19.452	40.348	64.595	74.459	81.256
	0.2		19.026	40.083	64.587	74.430	75.323
	0.4		18.180	38.436	64.501	66.703	74.324
	0.6		17.264	33.854	60.610	64.253	73.685
	0.8		16.624	26.624	57.367	63.830	64.333
	0.0	UD	19.277	39.774	64.158	73.812	80.029
	0.2		18.865	39.512	64.150	73.769	74.255
	0.4		18.048	37.928	64.066	65.801	73.681
	0.6		17.162	33.487	59.813	63.826	73.064
	0.8		16.544	26.410	56.618	63.272	63.627
	0.0	FG-V	19.176	39.440	63.917	73.465	79.315
	0.2		18.772	39.190	63.910	73.380	73.650
	0.4		17.196	37.637	63.827	65.212	73.335
	0.6		17.083	33.287	59.242	63.588	72.731
	0.8		16.466	26.304	56.046	62.838	63.327
	0.0	FG-O	19.110	39.224	63.764	73.225	78.862
	0.2		18.714	38.979	63.757	73.096	73.326
	0.4		17.925	37.450	63.676	64.696	73.098
	0.6		17.072	33.152	59.089	63.443	72.505
	0.8		16.477	26.277	55.941	62.578	63.168
CFCF	0.0	FG-X	20.210	20.636	43.589	54.083	54.648
	0.2		19.532	20.625	43.136	53.799	54.643
	0.4		18.043	20.477	42.512	51.474	54.560
	0.6		16.086	19.893	42.265	43.086	54.028
	0.8		13.992	18.358	31.709	42.240	51.706
	0.0	UD	19.881	20.312	43.204	53.244	53.816
	0.2		19.221	20.301	42.765	52.971	53.811
	0.4		17.772	20.157	42.157	50.735	53.730
	0.6		15.866	19.588	41.913	42.613	53.216
	0.8		13.824	18.093	31.416	41.890	50.973
	0.0	FG-V	19.683	20.121	42.984	52.750	53.332
	0.2		19.031	20.110	42.551	52.483	53.326
	0.4		17.594	19.968	41.948	50.308	53.274
	0.6		15.697	19.406	41.702	42.363	52.744
	0.8		13.657	17.926	31.269	41.680	50.554
	0.0	FG-O	19.562	20.002	42.841	52.444	53.028
	0.2		18.921	19.991	42.416	52.182	53.023
	0.4		17.514	19.852	41.824	50.040	52.945
	0.6		15.663	19.299	41.583	42.191	52.449
	0.8		13.679	17.848	31.167	41.563	50.288

Table 5.5 presents a comparative study of the first six non-dimensional frequencies for cross-ply (0°/90°/0°/90°/0°) CNTRC laminated plates subjected to simply supported (SSSS) and clamped-free (CFCF) boundary conditions, considering different normalized central crack lengths ($\bar{a}$ = 0, 0.2, 0.4, 0.6, 0.8). The results indicate that for shorter crack lengths ($\bar{a}$ =0 and 0.2), the CFCF boundary condition leads to higher frequencies (greater stiffness) compared to SSSS. However, this trend reverses for longer cracks ($\bar{a}$ =0.4,0.6,0.8), where the SSSS plate becomes stiffer. This behavior is attributed to the crack's alignment with the free edges in the CFCF configuration as it grows along the *x-axis*. Furthermore, the table consistently shows a decrease in fundamental frequencies with increasing crack length for all boundary conditions and fiber distributions, with FG-X exhibiting the highest and FG-O the lowest fundamental frequencies.

Table 5.6: Fundamental Non-dimensional frequencies of cross-ply $(0°/90°)_n$ and angle ply $(45°/-45°)_n$ laminated CFCF CNTRC plates with different number of plies and various crack length**.** (*L/W=1, W/h=50)*

Stacking sequences	*n*	Distribution	Crack length $\bar{a}$				
			0.0	0.2	0.4	0.6	0.8
$(0°/90°)_n$	2	FG-X	27.083	25.612	21.561	15.972	09.899
	4		28.545	27.063	23.295	18.482	13.829
	2	UD	26.644	25.209	21.261	15.829	09.969
	4		28.343	26.873	23.125	18.336	13.708
	2	FG-V	26.446	24.871	19.913	11.770	08.362
	4		28.399	26.898	22.998	17.915	12.872
	2	FG-O	26.216	24.822	21.002	15.779	10.219
	4		28.347	26.883	23.176	18.431	13.865
$(45°/-45°)_n$	2	FG-X	18.834	17.944	17.069	15.993	14.759
	4		19.296	18.871	17.950	16.820	15.529
	2	UD	18.061	17.666	16.806	15.748	14.534
	4		19.184	18.759	17.842	16.718	15.434
	2	FG-V	17.902	17.542	16.774	15.847	14.798
	4		19.193	18.779	17.887	17.797	15.557
	2	FG-O	17.788	17.401	16.554	15.515	14.320
	4		19.167	18.746	17.832	16.710	15.542

Table 5.6 presents the fundamental non-dimensional frequencies of clamped-free (CFCF) laminated plates with cross-ply (0°/90°) and angle-ply (45°/-45°) configurations, considering two ply numbers (*n*=2,4) and varying crack length ratios ($\bar{a}$ =0,0.2,0.4,0.6,0.8) for different fiber distribution patterns (UD, FG-X, FG-V, FG-O). Initially, cross-ply laminates are stiffer

than angle-ply, but this difference decreases with crack length incrases. FG-X generally provides the highest stiffness, especially without cracks, though the optimal fiber distribution can change based on laminate type and crack size (e.g., FG-V may be stiffer than FG-X in angle-ply laminates at larger crack ratios).

Table 5.7: Fundamental Non-dimensional frequencies of cross-ply $(0°/90°)_n$ and angle ply $(45°/-45°)_n$ laminated SSSS CNTRC plates with different number of plies and various crack length. (*L/W=1, W/h=50)*

Stacking sequences	*n*	Distribution	Crack length $\bar{a}$				
			0.0	0.2	0.4	0.6	0.8
$(0°/90°)_n$	2	FG-X	18.004	16.683	13.488	08.978	03.375
	4		19.020	17.669	14.677	10.979	07.701
	2	UD	17.706	16.421	13.316	08.965	03.767
	4		18.932	17.582	14.585	10.879	07.583
	2	FG-V	17.529	16.119	12.151	03.842	02.213
	4		18.910	17.542	14.441	10.467	06.690
	2	FG-O	17.415	16.170	13.178	09.044	04.382
	4		18.883	17.550	14.604	10.980	07.796
$(45°/-45°)_n$	2	FG-X	25.466	24.689	23.307	22.133	21.357
	4		26.189	25.388	23.969	22.787	22.072
	2	UD	25.065	24.304	22.945	21.787	21.020
	4		26.057	25.253	23.833	22.655	21.943
	2	FG-V	24.814	24.099	22.850	21.794	21.066
	4		26.034	25.249	23.865	22.715	22.016
	2	FG-O	24.669	23.923	22.588	21.448	20.688
	4		26.000	25.207	23.798	22.624	21.914

Table 5.7 presents a parametric study identical to that of Table 5.6 for laminated composite plates, with the sole difference being the boundary condition: simply supported on all sides (SSSS) instead of clamped-free (CFCF). A key observation from Table 5.7 is that SSSS boundary conditions generally lead to higher natural frequencies in angle-ply laminates compared to CFCF, irrespective of crack length and ply number (n=2,4). Consistent with Table 5.6, for un-cracked cross-ply laminates (0°/90°), FG-X exhibits the highest and FG-O the lowest natural frequencies for both n=2 and n=4. Increasing crack length causes a reduction in natural frequencies across all distributions, with FG-V being the most affected, becoming the least stiff at $\bar{a}$ =0.8. In contrast to cross-ply laminates, angle-ply laminates (45°/-45°) show minimal

sensitivity to increasing crack length, with FG-X consistently displaying the highest and FG-O the lowest natural frequencies.

Table 5.8: Fundamental Non-dimensional frequencies of cross-ply $(0°/90°/0°)_s$ and angle ply $(45°/-45°/45°)_s$ laminated SSSS CNTRC plates with different number of plies and various crack length. (*L/W=1, W/h=50)*

Stacking sequences	Distribution	Crack length $\bar{a}$				
		0.0	0.2	0.4	0.6	0.8
$(0°/90°/0°)_S$	FG-X	19.421	18.872	17.775	16.584	15.750
	UD	19.297	18.755	17.672	16.499	15.677
	FG-V	19.230	18.691	17.613	16.441	15.617
	FG-O	19.183	18.650	17.585	16.432	15.625
$(45°/-45°/45°)_S$	FG-X	25.368	24.387	22.362	20.385	18.967
	UD	25.194	24.219	22.204	20.235	18.818
	FG-V	25.093	24.122	22.113	20.144	18.725
	FG-O	25.032	24.064	22.063	20.102	18.689

An investigation, detailed in Table 5.8, examined the influence of symmetric cross-ply ($(0°/90°/0°)_S$) and angle-ply ($(45°/-45°/45°)_S$) stacking sequences on the natural frequencies of simply supported square laminated CNTRC plates. A key observation was that angle-ply laminates consistently yielded higher fundamental frequencies than their cross-ply counterparts with the same number of plies. Furthermore, the study revealed that increasing crack length reduced the free vibration frequencies for both laminate types and all considered CNT distribution patterns (FG-X, FG-O, UD, and FG-A). Across varying crack lengths, the FG-X distribution consistently provided the highest stiffness, while FG-O exhibited the lowest. This superiority of FG-X is attributed to its higher CNT concentration at the outer surfaces, which are critical for bending resistance. The lower stiffness of FG-O is likely due to its increased CNT content near the mid-plane, a less effective location for enhancing bending stiffness.

Table 5.9: Fundamental non-dimensional frequencies of cross-ply (0°/90°) CNTRC laminated composite plates with various plate configuration and various crack (*L/W=1, W/h=50)*

BC	Plate configuration	Crack length $\bar{a}$				
		0.0	0.2	0.4	0.6	0.8
CCCC	[A-A-V-V]	42.471	39.815	34.788	30.498	28.613
	[V-V-A-A]	32.560	30.799	27.538	24.898	23.790
	[X-X-X-X]	38.566	36.289	32.038	28.505	26.993
	[A-A-A-A-V-V-V-V]	42.633	40.137	35.754	32.307	30.914
	[V-V-V-V A-A-A-A]	38.156	36.077	32.492	29.762	28.695
	[X-X-X-X-X-X-X-X]	40.622	38.319	34.312	31.209	29.974
CFCF	[A-A-V-V]	29.868	28.131	23.244	16.256	07.748
	[V-V-A-A]	22.790	21.676	18.668	14.648	10.574
	[X-X-X-X]	27.083	25.612	21.561	15.972	09.899
	[A-A-A-A-V-V-V-V]	29.997	28.361	24.196	18.787	13.422
	[V-V-V-V A-A-A-A]	26.784	25.458	22.131	17.955	14.007
	[X-X-X-X-X-X-X-X]	28.544	27.062	23.294	18.481	13.828
SSSS	[A-A-V-V]	19.934	18.341	14.389	08.289	02.265
	[V-V-A-A]	15.138	14.161	11.855	08.863	06.053
	[X-X-X-X]	18.004	16.683	13.488	08.978	03.375
	[A-A-A-A-V-V-V-V]	20.021	18.530	15.181	10.889	06.766
	[V-V-V-V A-A-A-A]	17.811	16.616	14.010	10.910	08.343
	[X-X-X-X-X-X-X-X]	19.019	17.668	14.676	10.978	07.710

Table 5.10: Fundamental non-dimensional frequency of angle-ply (45°/-45°) CNTRC laminated composite plates with various plate configuration and various crack. (*L/W=1, W/h=50)*

BC	Plate configuration	Crack length $\bar{a}$				
		0.0	0.2	0.4	0.6	0.8
CCCC	[A-A-V-V]	40.322	38.778	36.412	34.990	34.484
	[V-V-A-A]	31.110	29.994	28.286	27.107	26.738
	[X-X-X-X]	36.698	35.324	33.186	31.889	31.441
	[A-A-A-A-V-V-V-V]	40.475	38.924	36.536	35.102	34.630
	[V-V-V-V A-A-A-A]	36.320	34.963	32.838	31.547	31.140
	[X-X-X-X-X-X-X-X]	38.610	37.146	34.876	33.206	33.064
CFCF	[A-A-V-V]	20.164	19.710	18.783	17.549	16.183
	[V-V-A-A]	15.618	15.288	14.557	13.650	12.609
	[X-X-X-X]	18.347	17.944	17.069	15.993	14.759
	[A-A-A-A-V-V-V-V]	20.236	19.785	18.813	17.624	16.264
	[V-V-V-V A-A-A-A]	18.154	17.761	16.902	15.844	14.636
	[X-X-X-X-X-X-X-X]	19.295	18.870	17.950	16.820	15.529
SSSS	[A-A-V-V]	28.067	27.190	25.654	24.368	23.538
	[V-V-A-A]	21.576	20.946	19.792	18.784	18.086
	[X-X-X-X]	25.466	24.689	23.307	22.133	21.357
	[A-A-A-A-V-V-V-V]	27.569	26.715	25.213	23.970	23.223
	[V-V-V-V A-A-A-A]	24.512	23.776	22.456	21.347	20.671
	[X-X-X-X-X-X-X-X]	26.188	25.387	23.968	22.785	22.071

The data in Tables 5.9 and 5.10 suggests a trend where the [A-V] configuration (FG-A top, FG-V bottom) provides the highest non-dimensional frequency parameters for both cross-ply and angle-ply laminates with two and four plies, likely due to the concentration of CNTs in the outer layers enhancing stiffness. However, this trend reverses with increasing crack length, especially at a substantial crack length ($\bar{a}$ = 0.8) for cross-ply laminates under CFCF and SSSS boundary conditions. This reversal is likely because the crack affects the upper surface, where the [A-V] configuration has a higher CNT density. Notably, the tables also show that for these specific conditions (CFCF and SSSS, significant crack in cross-ply), the [V-A] configuration (mid-plane CNT concentration) becomes a more effective solution. Its performance, indicated by higher non-dimensional frequency parameters and thus stiffness, appears less sensitive to the presence of cracks, potentially making it superior in these cases.

5.3.1 Effect of CNT volume fraction and plate Width/thick ratio

To understand the effect of CNT reinforcement on the mechanical behavior of cracked composite plates, the study varied CNT volume fraction and plate geometry. Figures 5.3 and 5.4 illustrate the relationship between fiber volume fraction and the natural frequencies of cracked laminated composite plates with CCCC and CFCF boundary conditions for cross-ply ((0°/90°)) and angle-ply ((45°/-45°)) layups, respectively. Within each layup, three configurations ([A-A-V-V], [V-V-A-A], and [X-X-X-X]) were compared. A consistent observation across both figures was the reduction in natural frequencies with increasing crack length, highlighting the weakening effect of cracks. Increasing fiber volume fraction generally improved the stiffness and vibration frequencies of both laminate types. Notably, the [A-A-V-V] configuration, with a higher concentration of CNTs in the outer layers (away from the neutral plane), consistently exhibited the best performance. In contrast, the [V-V-A-A] configuration, featuring more CNTs in the inner layers, typically showed lower frequencies. However, under specific conditions—a large crack and CFCF boundary in cross-ply laminates—the [V-V-A-A] configuration showed potential for superior performance. This anomaly might be attributed to a more effective interaction between the 90° oriented CNTs in the inner (V-V) layers and the matrix, which could better resist stress concentration caused by the crack under these particular circumstances. The results emphasize the significant influence of strategic CNT distribution within laminated composites on achieving optimal stiffness and vibration characteristics.

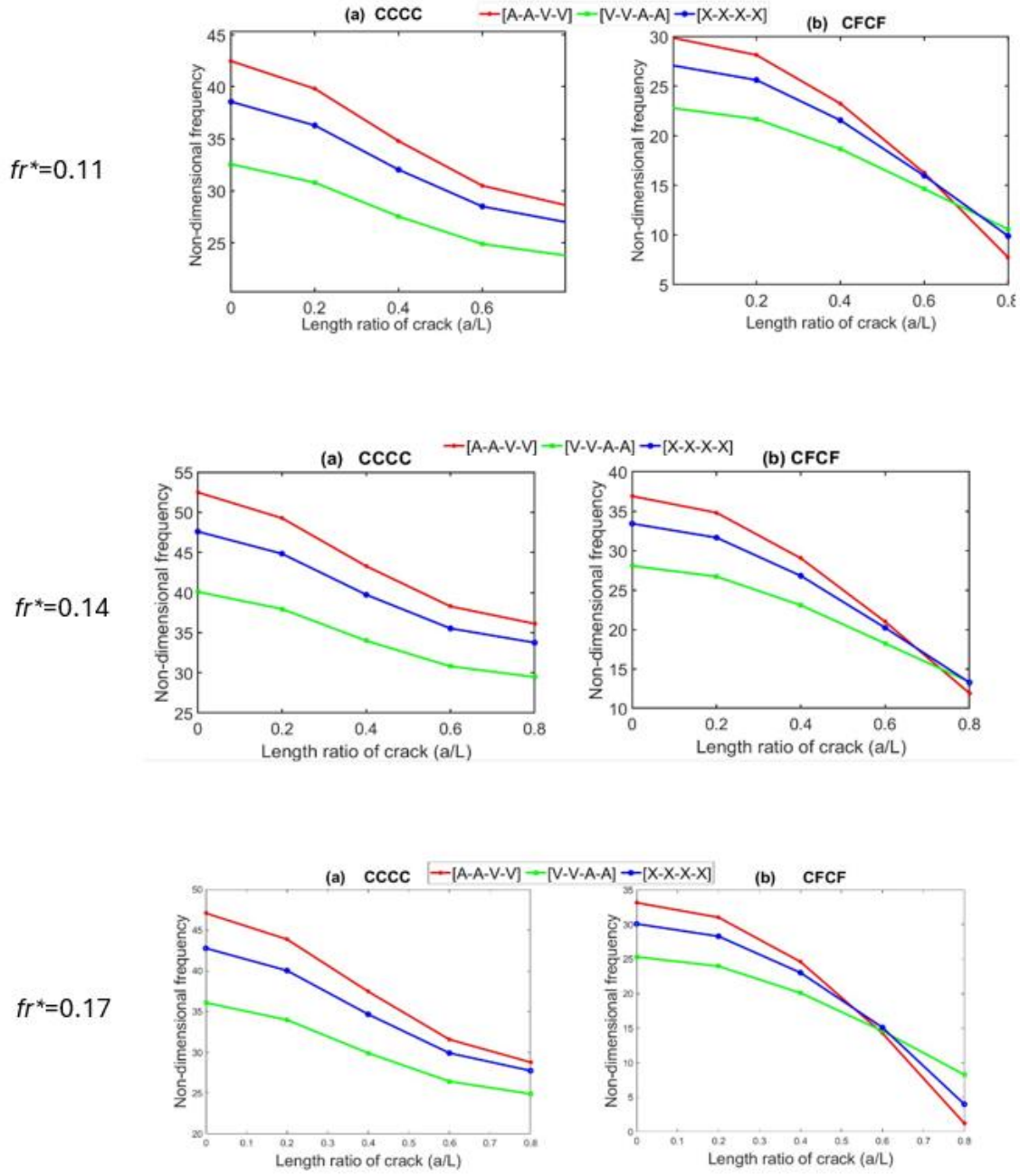

Figure 5.3: Effect of Crack Length on Fundamental Frequency in Cross-Ply (0°/90°) Laminate plate with different fiber volume fraction and plate configuration

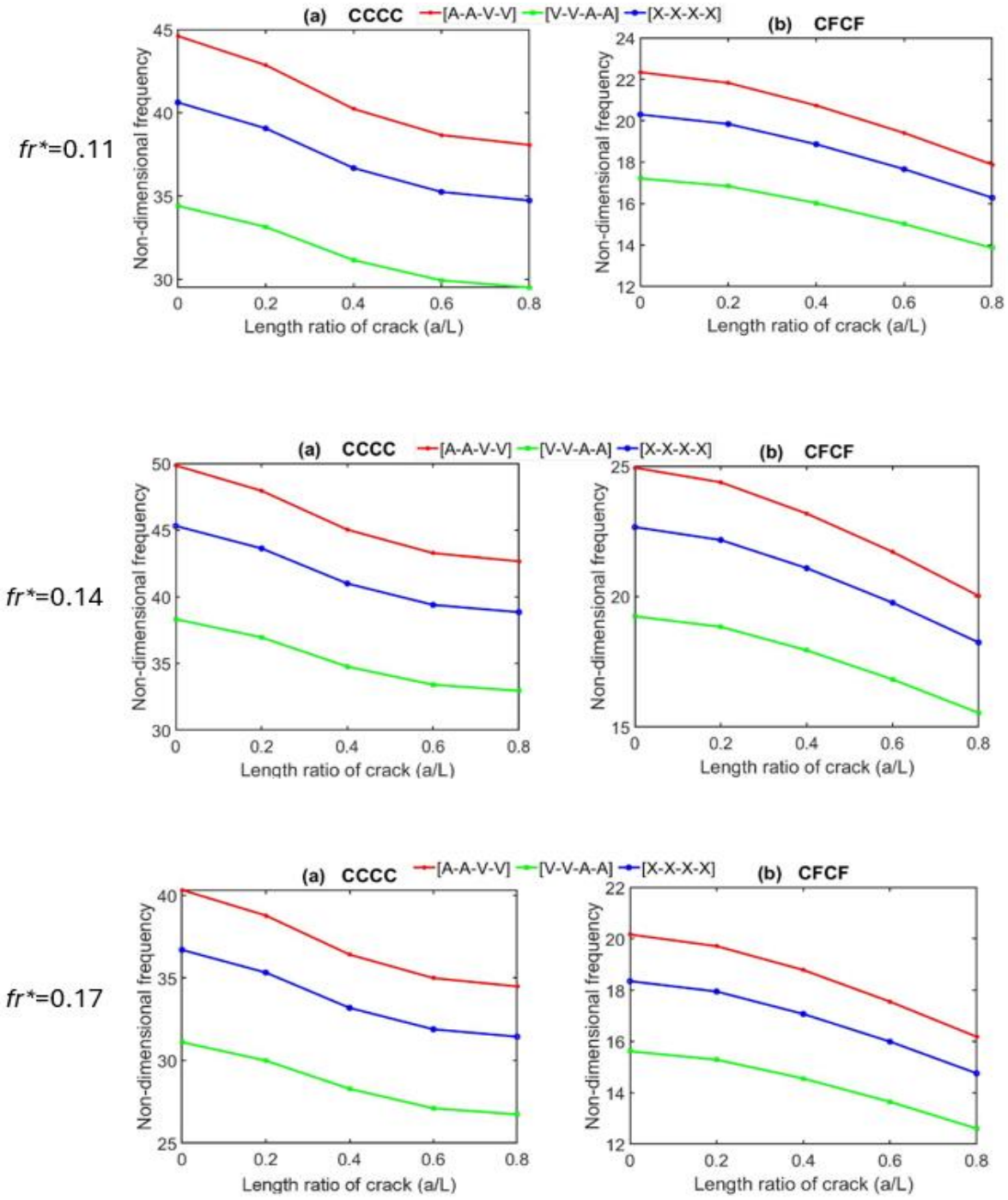

Figure 5.4: Effect of Crack Length on Fundamental Frequency in Angle-Ply (45°/-45°) Laminate plate with different fiber volume fraction and plate configuration

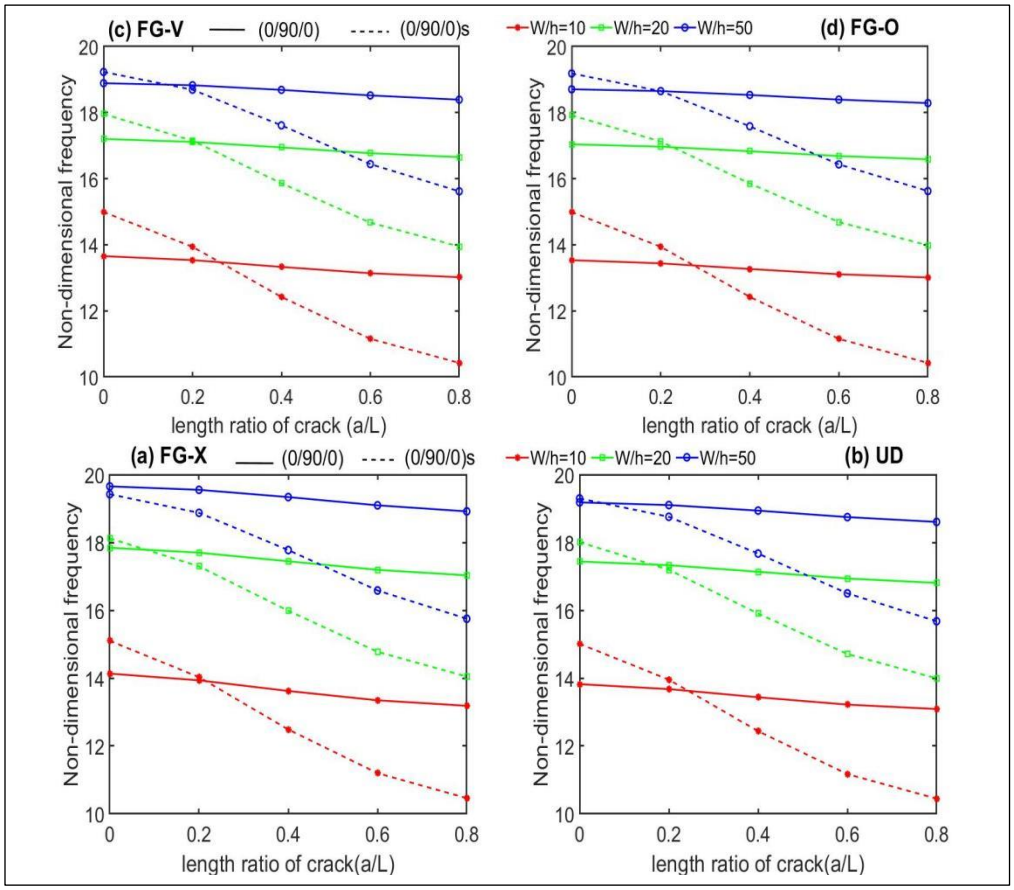

Figure 5.5: Effect of Crack Length on Fundamental Frequencies of SSSS Cross-Ply (0°/90°) Laminated square plate with different width to thick ratio.

Figure 5.5 investigates the combined effects of width-to-thickness (W/h) and crack length $\bar{a}$ on the natural frequencies of composite laminates. It specifically examines these effects for cross-ply laminates with two configurations: a basic three-ply laminate with a (0°/90°/0°) stacking sequence (n = 3) and a symmetric six-ply laminate with a symmetric stacking sequence $(0°/90°/0°)_s$ (n = 6).

The study observed a clear influence of both width-to-thickness ratio (W/h) and stacking sequence on the natural frequencies of the composite laminates (cross-ply and symmetric cross-ply). For both configurations, the highest W/h ratio ($W/h = 50$) resulted in the highest natural frequencies due to their reduced bending under vibration. Notably across all distribution patterns and for (W/h) ratios of 10, 20, and 50, the symmetric stacking sequence $(0°/90°/0°)_s$

exhibited higher frequencies, especially for un-cracked plates and plates with small crack lengths. This might be due to a more balanced distribution of stiffness within the laminate due to the symmetrical arrangement of plies. However, as the crack length increased, the natural frequencies for the symmetric stacking sequence dropped significantly. In some cases, they even fell below the frequencies of the basic stacking sequence (0°/90°/0°). This suggests that cracks disrupt the symmetrical stiffness advantage, potentially affecting the vibration behavior more severely in the symmetric configuration. Interestingly, FG-X and UD distributions in the high w/h configuration ($W/h = 50$) defied this trend, with the symmetric sequence maintaining superiority regardless of crack length. This could be due to inherent crack resistance properties of FG-X and UD or the high (W/h) ratio offering a more robust structure in the symmetric configuration.

5.3.2 Effect of power law-index

The vibration behavior of cracked CNT-reinforced composite (CNTRC) laminated plates is influenced by the distribution of the nonlinear nano-reinforcement. To investigate this, we examined the impact of the Pin power index, which characterizes the variability or uncertainty in how the nano-reinforcement is graded nonlinearly through the thickness of the plies.

Table 5.11: Fundamental non-dimensional frequencies of cross-ply (0°/90°) and angle- ply (45°/-45°) laminated CNTRC plates with various values of power-law index P_{in}, plate configuration and crack length (CFCF, $L/W=1$, $f^{*}_{CNT}=0.11$ and $W/h=50$)

Stacking sequences	$\bar{a}$	Plate configuration	P_{in}					
			0.0	0.4	0.8	1.0	1.4	1.8
(0°/90°)	0.0	[A-A-V-V]	26.644	28.275	29.415	29.868	30.613	31.201
		[V-V-A-A]	26.644	24.790	23.336	22.790	21.833	21.071
		[X-X-X-X]	26.644	26.882	27.022	27.083	27.192	27.285
	0.4	[A-A-V-V]	21.261	22.283	22.975	23.244	23.682	24.028
		[V-V-A-A]	21.261	20.042	19.071	18.668	17.989	17.440
		[X-X-X-X]	21.261	21.414	21.515	21.561	21.643	21.717
	0.8	[A-A-V-V]	09.969	09.108	08.202	07.748	06.867	06.042
		[V-V-A-A]	09.969	10.455	10.578	10.574	10.508	10.409
		[X-X-X-X]	09.969	09.874	09.886	09.899	09.931	09.974
(45°/-45°)	0.0	[A-A-V-V]	18.061	19.118	19.865	20.164	20.657	21.050
		[V-V-A-A]	18.061	16.876	15.979	15.618	15.023	14.554
		[X-X-X-X]	18.061	18.215	18.307	18.347	18.419	18.481
	0.4	[A-A-V-V]	16.806	17.777	18.464	18.738	19.192	19.553
		[V-V-A-A]	16.806	15.715	14.890	14.557	14.009	13.576
		[X-X-X-X]	16.806	16.947	17.032	17.069	17.135	17.193
	0.8	[A-A-V-V]	14.534	15.363	15.949	16.183	16.571	16.879
		[V-V-A-A]	14.534	13.601	12.894	12.609	12.138	11.766
		[X-X-X-X]	14.534	14.654	14.727	14.759	14.816	14.866

Table 5.11 illustrates the intricate effects of the power-law index (P_{in}), crack length, stacking sequence, and plate configuration on the natural frequencies of CFCF laminated CNTRC plates. For most cases involving ((0°/90°)) and ((45°/-45°)) stacking and varying crack lengths, a higher Pin value increases natural frequencies when CNTs are concentrated at the top and bottom surfaces [A-A-V-V] and [X-X-X-X] but decreases them when CNTs are concentrated at the mid-plane [V-V-A-A]. However, a contrasting trend emerges for the (0°/90°) layup with a substantial crack length of 0.8. In this specific scenario, increasing Pin leads to a reduction in natural frequencies for the surface-concentrated configurations and an increase for the mid-plane-concentrated one. This anomaly can be attributed to the influence of the 90° fiber orientation in the outer layers on the plate's response to vibration and stress in the presence of a significant crack.

5.4 Conclusion

In this chapter, the free vibration behavior of cracked laminated CNT-reinforced composite plates was thoroughly examined using the validated XFEM-based MATLAB program. The results demonstrated that both the CNT distribution within each ply and the stacking sequence across the laminate significantly influence the stiffness and natural frequencies of damaged multilayer plates. The study highlighted how crack length, crack location, geometric ratios, CNT volume fraction, and the power-law index interact differently in multilayer configurations compared to single-layer structures. The analyses also confirmed the strong coupling between intra-ply functional grading and inter-ply arrangement in shaping the dynamic response. Overall, this investigation provides new insight into the vibrational behavior of cracked laminated nanocomposite plates, offering valuable guidance for advanced structural design and optimization.

Conclusion

This research provides a comprehensive understanding of the vibration behavior of cracked Functionally Graded Carbon Nanotube Reinforced Composite (FG-CNTRC) plates using the Extended Finite Element Method (XFEM). The work began by establishing the scientific background related to composite and nanocomposite materials, with particular emphasis on the exceptional mechanical properties of carbon nanotubes, the challenges of their synthesis and dispersion, and their integration into matrix materials. The numerical formulation of XFEM was then developed to enable efficient modeling of cracks without remeshing, forming the theoretical basis for all subsequent analyses.

The study delivered important findings regarding the free vibration response of cracked FG-CNTRC plates. Results revealed the strong sensitivity of natural frequencies to crack length, crack location, CNT distribution patterns, plate geometry, CNT volume fraction, and the power-law index. CNT distributions such as FG-X consistently provided higher stiffness and improved vibrational performance, while increasing crack length led to substantial reductions in natural frequencies. Boundary conditions played a major role, with clamped edges significantly enhancing stiffness. Findings also showed that although CNT reinforcement offers superior mechanical performance, traditional composites can approach similar stiffness levels when the fiber volume fraction is sufficiently increased.

Further extending the investigation to multilayer laminated CNTRC plates highlighted the crucial influence of stacking sequence and the combined effects of intra-ply CNT distribution and inter-ply arrangement. The optimal laminate configuration was shown to depend on both the severity and the position of the crack, as well as on the grading law governing CNT distribution. The interaction between material grading, laminate architecture, and crack characteristics demonstrated the complexity and richness of the dynamic behavior in these advanced composites.

Overall, this thesis provides valuable insights into the interplay between microstructural design, material distribution, and structural discontinuities in CNT-reinforced composite plates. By

integrating XFEM with detailed material modeling, the study contributes to a deeper understanding of the vibration behavior of cracked nanocomposite structures and offers guidance for the optimized design of high-performance components subjected to dynamic loading.

REFRENCES

[1] S. Suresh and R. O. Ritchie, “Propagation of short fatigue cracks,” *Int. Met. Rev.*, vol. 29, no. 1, pp. 445–473, 1984, doi: 10.1179/imtr.1984.29.1.445.

[2] M. D. Sangid, “The physics of fatigue crack initiation,” *Int. J. Fatigue*, vol. 57, pp. 58–72, 2013, doi: 10.1016/j.ijfatigue.2012.10.009.

[3] Y. Jiang and M. Feng, “Modeling of fatigue crack propagation,” *J. Eng. Mater. Technol.*, vol. 126, no. 1, pp. 77–86, 2004, doi: 10.1115/1.1631026.

[4] H. A. Richard, *Fatigue Crack Growth Testing*. 2018. doi: 10.31399/asm.hb.v08.a0003317.

[5] C. K. Lin and J. H. Wang, “Environmental effects on fatigue crack growth in austempered ductile irons,” *Mater. Trans.*, vol. 42, no. 6, pp. 1085–1094, 2001, doi: 10.2320/matertrans.42.1085.

[6] B. Tomkins, “Fatigue crack propagation—an analysis,” *Philos. Mag.*, vol. 18, no. 155, pp. 1041–1066, 1968, doi: 10.1080/14786436808227524.

[7] A. K. Vasudeven, K. Sadananda, and N. Louat, “A review of crack closure, fatigue crack threshold and related phenomena,” *Mater. Sci. Eng. A*, vol. 188, no. 1–2, pp. 1–22, 1994, doi: 10.1016/0921-5093(94)90351-4.

[8] D. Nuttall, “Stress corrosion cracking – materials performance and evaluation,” *Corros. Eng. Sci. Technol.*, vol. 54, no. 3, pp. 276–276, 2019, doi: 10.1080/1478422x.2019.1574960.

[9] S. K. Dwivedi, M. Vishwakarma, and P. A. Soni, “Advances and Researches on Non Destructive Testing: A Review,” *Mater. Today Proc.*, vol. 5, no. 2, pp. 3690–3698, 2018, doi: 10.1016/j.matpr.2017.11.620.

[10] M. Saleem and H. Gutierrez, “Using artificial neural network and non-destructive test for crack detection in concrete surrounding the embedded steel reinforcement,” *Struct. Concr.*, vol. 22, no. 5, pp. 2849–2867, 2021, doi: 10.1002/suco.202000767.

[11] M. Rucka, “Special issue: ‘non-destructive testing of structures,’” *Materials (Basel).*, vol. 13, no. 21, pp. 1–6, 2020, doi: 10.3390/ma13214996.

[12] M. Elices, G. V. Guinea, J. Gómez, and J. Planas, “The cohesive zone model: Advantages, limitations and challenges,” *Eng. Fract. Mech.*, vol. 69, no. 2, pp. 137–163, 2001, doi: 10.1016/S0013-7944(01)00083-2.

[13] R. de Borst, J. J. C. Remmers, and A. Needleman, “Mesh-independent discrete numerical representations of cohesive-zone models,” *Eng. Fract. Mech.*, vol. 73, no. 2, pp. 160–177, 2006, doi: 10.1016/j.engfracmech.2005.05.007.

[14] S. A. Ponnusami, S. Turteltaub, and S. van der Zwaag, “Cohesive-zone modelling of crack nucleation and propagation in particulate composites,” *Eng. Fract. Mech.*, vol.

149, pp. 170–190, 2015, doi: 10.1016/j.engfracmech.2015.09.050.

[15] Q. H. Qin and Y. W. Mai, “BEM for crack-hole problems in thermopiezoelectric materials,” *Eng. Fract. Mech.*, vol. 69, no. 5, pp. 577–588, 2002, doi: 10.1016/S0013-7944(01)00095-9.

[16] A. M. Yan and H. Nguyen-Dang, “Multiple-cracked fatigue crack growth by BEMA,” *Comput. Mech.*, vol. 16, no. 5, pp. 273–280, 1995, doi: 10.1007/s004660050071.

[17] A. K. M. Farid Uddin, K. Numata, J. Shimasaki, M. Shigeishi, and M. Ohtsu, “Mechanisms of crack propagation due to corrosion of reinforcement in concrete by AE-SiGMA and BEM,” *Constr. Build. Mater.*, vol. 18, no. 3, pp. 181–188, 2004, doi: 10.1016/j.conbuildmat.2003.10.007.

[18] T. Belytschko, D. Organ, and C. Gerlach, “Element-free galerkin methods for dynamic fracture in concrete,” *Comput. Methods Appl. Mech. Eng.*, vol. 187, no. 3–4, pp. 385–399, 2000, doi: 10.1016/S0045-7825(00)80002-X.

[19] Z. Tang, S. Shen, and S. N. Atluri, “Analysis of materials with strain-gradient effects: A meshless local Petrov-Galerkin (MLPG) approach, with nodal displacements only,” *C. - Comput. Model. Eng. Sci.*, vol. 4, no. 1, pp. 177–196, 2003.

[20] T. Belytschko, Y. Krongauz, D. Organ, M. Fleming, and P. Krysl, “Meshless methods: An overview and recent developments,” *Comput. Methods Appl. Mech. Eng.*, vol. 139, no. 1–4, pp. 3–47, 1996, doi: 10.1016/S0045-7825(96)01078-X.

[21] T. BELYTSCHKO and T. BLACK, “ELASTIC CRACK GROWTH IN FINITE ELEMENTS WITH MINIMAL REMESHING T.,” *INERNATIONAL J. Numer. METHODS Eng.*, p. 20, 1999, doi: https://doi.org/10.1002/(SICI)1097-0207.

[22] N. Moës, J. Dolbow, and T. Belytschko, “A finite element method for crack growth without remeshing,” *Int. J. Numer. Methods Eng.*, vol. 46, no. 1, pp. 131–150, 1999, doi: 10.1002/(sici)1097-0207(19990910)46:1<131::aid-nme726>3.3.co;2-a.

[23] N. Moës, T. Belytschko, N. Mo, and T. Belytschko, “Extended finite element method for cohesive crack growth To cite this version : HAL Id : hal-01461938 Extended finite element method for cohesive crack growth,” *Eng. Fract. Mech.*, vol. 69, pp. 813–833, 2017.

[24] J. Dolbow, N. Moës, and T. Belytschko, “Discontinuous enrichment in finite elements with a partition of unity method,” *Finite Elem. Anal. Des.*, vol. 36, no. 3, pp. 235–260, 2000, doi: 10.1016/S0168-874X(00)00035-4.

[25] J. Dolbow *et al.*, “Modeling fracture in Mindlin-Reissner plates with the eXtended finite element method To cite this version : HAL Id : hal-01007064 Modeling fracture in Mindlin ± Reissner plates with the extended ® nite element method,” 2023.

[26] C. Daux, N. Moës, J. Dolbow, N. Sukumar, and T. Belytschko, “Arbitrary branched and intersecting cracks with the extended finite element method,” *Int. J. Numer. Methods Eng.*, vol. 48, no. 12, pp. 1741–1760, 2000, doi: 10.1002/1097-0207(20000830)48:12<1741::AID-NME956>3.0.CO;2-L.

[27] N. Sukumar *et al.*, “Extended Finite Element Method for three-dimensional crack modelling To cite this version : HAL Id : hal-01006859 Extended nite element method for three-dimensional crack modelling,” 2019.

[28] P. M. A. Areias and T. Belytschko, “Non-linear analysis of shells with arbitrary evolving cracks using XFEM,” *Int. J. Numer. Methods Eng.*, vol. 62, no. 3, pp. 384–415, 2005, doi: 10.1002/nme.1192.

[29] P. M. A. Areias, J. H. Song, and T. Belytschko, “Analysis of fracture in thin shells by overlapping paired elements,” *Comput. Methods Appl. Mech. Eng.*, vol. 195, no. 41–43, pp. 5343–5360, 2006, doi: 10.1016/j.cma.2005.10.024.

[30] H. Bayesteh and S. Mohammadi, “XFEM fracture analysis of shells: The effect of crack tip enrichments,” *Comput. Mater. Sci.*, vol. 50, no. 10, pp. 2793–2813, 2011, doi: 10.1016/j.commatsci.2011.04.034.

[31] M. Stolarska, D. L. Chopp, N. Mos, and T. Belytschko, “Modelling crack growth by level sets in the extended finite element method,” *Int. J. Numer. Methods Eng.*, vol. 51, no. 8, pp. 943–960, 2001, doi: 10.1002/nme.201.

[32] T. Belytschko *et al.*, “Arbitrary discontinuities in finite elements To cite this version : HAL Id : hal-01005275 Arbitrary discontinuities in nite elements,” vol. 50, no. 4, pp. 993–1013, 2019.

[33] J. Mergheim, E. Kuhl, and P. Steinmann, “A finite element method for the computational modelling of cohesive cracks,” *Int. J. Numer. Methods Eng.*, vol. 63, no. 2, pp. 276–289, 2005, doi: 10.1002/nme.1286.

[34] R. de Borst, J. J. C. Remmers, A. Needleman, and M. A. Abellan, “Discrete vs smeared crack models for concrete fracture: Bridging the gap,” *Int. J. Numer. Anal. Methods Geomech.*, vol. 28, no. 7–8, pp. 583–607, 2004, doi: 10.1002/nag.374.

[35] R. de Borst, M. A. Gutiérrez, G. N. Wells, J. J. C. Remmers, and H. Askes, “Cohesive-zone models, higher-order continuum theories and reliability methods for computational failure analysis,” *Int. J. Numer. Methods Eng.*, vol. 60, no. 1, pp. 289–315, 2004, doi: 10.1002/nme.963.

[36] S. Mariani and U. Perego, “Extended finite element method for quasi-brittle fracture,” *Int. J. Numer. Methods Eng.*, vol. 58, no. 1, pp. 103–126, 2003, doi: 10.1002/nme.761.

[37] P. Laborde *et al.*, “High order extended finite element method for cracked domains To cite this version : HAL Id : hal-00815711,” 2013, doi: 10.1002/nme.1370/abstract.

[38] M. Peters and K. Hackl, “Numerical aspects of the eXtended Finite Element Method Markus,” *proc.appl. math. mech*, vol. 28, no. SUPPL., pp. 305–310, 2005, doi: 10.1002/pamm.200510154 Numerical.

[39] E. Bechet *et al.*, “Improved implementation and robustness study of the X-FEM method for stress analysis around cracks To cite this version : HAL Id : hal-01006958 Improved implementation and robustness study of the X-FEM for stress analysis around cracks,” 2019.

[40] G. Ventura, “On the elimination of quadrature subcells for discontinuous functions in the eXtended Finite-Element Method,” no. June 2005, pp. 761–795, 2006, doi: 10.1002/nme.1570.

[41] Q. Z. Xiao and B. L. Karihaloo, “Improving the accuracy of XFEM crack tip fields using higher order quadrature and statically admissible stress recovery,” no. July 2005, pp. 1378–1410, 2006, doi: 10.1002/nme.1601.

[42] B. Faria, C. Guarda, N. Silvestre, J. N. C. Lopes, and D. Galhofo, “Strength and failure mechanisms of cnt-reinforced copper nanocomposite,” *Compos. Part B*, 2018, doi: 10.1016/j.compositesb.2018.02.033.

[43] T. Stern, “Fracture Mechanisms and Toughness in Polymer Nanocomposites : A Brief Review,” 2024.

[44] M. H. Woldemariam, G. Belingardi, E. G. Koricho, and D. T. Reda, “Effects of nanomaterials and particles on mechanical properties and fracture toughness of composite materials : a short review,” vol. 6, no. December, pp. 1191–1212, 2019, doi: 10.3934/matersci.2019.6.1191.

[45] V. Singhal, D. Shelly, A. Saxena, R. Gupta, V. K. Verma, and A. Jain, “Study of the Influence of Nanoparticle Reinforcement on the Mechanical and Tribological Performance of Aluminum Matrix Composites—A Review,” *Lubricants*, vol. 13, no. 2, 2025, doi: 10.3390/lubricants13020093.

[46] W. Abd-Elaziem *et al.*, “Influence of nanoparticles addition on the fatigue failure behavior of metal matrix composites: Comprehensive review,” *Eng. Fail. Anal.*, vol. 155, no. August 2023, p. 107751, 2024, doi: 10.1016/j.engfailanal.2023.107751.

[47] Z. Zhang *et al.*, “Promoting crack self-healing of nanocomposite coating by double slip systemic semi-coherent interface dislocation,” *Mater. Res. Lett.*, vol. 12, no. 7, pp. 467–476, 2024, doi: 10.1080/21663831.2024.2348661.

[48] M. Rahman, K. H. Khan, M. H. Parvez, and N. Irizarry, “Polymer Nanocomposites with Optimized Nanoparticle Dispersion and Enhanced Functionalities for Industrial Applications,” 2025.

[49] N. Stern, X. Hu, and G. Marom, “The effects of geometry and chemical composition of nanoparticles on the fracture toughness of ipp nanocomposites,” *J. Compos. Sci.*, vol. 4, no. 1, pp. 1–10, 2020, doi: 10.3390/jcs4010024.

[50] S. Tamayo-vegas, A. Muhsan, C. Liu, M. Tarfaoui, and K. Lafdi, “The Effect of Agglomeration on the Electrical and Mechanical Properties of Polymer Matrix Nanocomposites Reinforced with Carbon Nanotubes,” *Polymers (Basel).*, vol. 14, no. 9, 2022, doi: 10.3390/polym14091842.

[51] J. K. Pandey, K. Raghunatha Reddy, A. Pratheep Kumar, and R. P. Singh, “An overview on the degradability of polymer nanocomposites,” *Polym. Degrad. Stab.*, vol. 88, no. 2, pp. 234–250, 2005, doi: 10.1016/j.polymdegradstab.2004.09.013.

[52] R. Mohanty, “Vibration Analysis of Cracked Composite Plate Department Of Civil Engineering National Institute Of Technology Rourkela Rourkela-769008,” pp. 1–49.

[53] A. Israr, “VIBRATION ANALYSIS OF CRACKED To my parents and my family,” no. June, 2008.

[54] B. Mourad, “EFFETS DE LA LONGUEUR DE DELAMINAGE ET DE SA POSITION SUR LE COMPORTEMENT VIBRATOIRE DES PLAQUES COMPOSITES STRATIFIEES,” ecole national polytechnique, 2009.

[55] A. Negi, G. Bhardwaj, J. S. Saini, K. Khanna, and R. K. Godara, “Analysis of CNT reinforced polymer nanocomposite plate in the presence of discontinuities using XFEM,” *Theor. Appl. Fract. Mech.*, vol. 103, no. May, 2019, doi: 10.1016/j.tafmec.2019.102292.

[56] A. Negi, G. Bhardwaj, J. S. Saini, and N. Grover, “Crack growth analysis of carbon nanotube reinforced polymer nanocomposite using extended finite element method,” *Proc. Inst. Mech. Eng. Part C J. Mech. Eng. Sci.*, vol. 233, no. 5, pp. 1750–1770, 2019, doi: 10.1177/0954406218776034.

[57] M. H. Taheri and P. Memarzadeh, “Effect of crack on shear buckling of CNTRC plates,” *Int. J. Mech. Sci.*, vol. 229, no. July, p. 107519, 2022, doi: 10.1016/j.ijmecsci.2022.107519.

[58] Y. Chiker, M. Bachene, S. Bouaziz, M. Guemana, M. Ben Amar, and M. Haddar, “Free vibration analysis of hybrid laminated plates containing multilayer functionally graded carbon nanotube-reinforced composite plies using a layer-wise formulation,” *Arch. Appl. Mech.*, vol. 91, no. 1, pp. 463–485, 2021, doi: 10.1007/s00419-020-01783-3.

[59] K. Nguyen-Quang, T. Vo-Duy, H. Dang-Trung, and T. Nguyen-Thoi, “An isogeometric approach for dynamic response of laminated FG-CNT reinforced composite plates integrated with piezoelectric layers,” *Comput. Methods Appl. Mech. Eng.*, vol. 332, pp. 25–46, 2018, doi: 10.1016/j.cma.2017.12.010.

[60] A. Bachiri, A. A. Daikh, and A. Tounsi, “On the Thermo-elastic Response of FG-CNTRC Cross-ply Laminated Plates under Temperature Loading using a New HSDT,” *J. Appl. Comput. Mech.*, vol. 8, no. 4, pp. 1370–1386, 2022, doi: 10.22055/jacm.2022.40148.3529.

[61] H. Q. Tran, V. T. Vu, M. T. Tran, and P. Nguyen-Tri, “A new four-variable refined plate theory for static analysis of smart laminated functionally graded carbon nanotube reinforced composite plates,” *Mech. Mater.*, vol. 142, p. 103294, 2020, doi: 10.1016/j.mechmat.2019.103294.

[62] Z. X. Lei, L. W. Zhang, and K. M. Liew, “Buckling analysis of CNT reinforced functionally graded laminated composite plates,” *Compos. Struct.*, vol. 152, pp. 62–73, 2016, doi: 10.1016/j.compstruct.2016.05.047.

[63] L. Gebrehiwet, E. Abate, Y. Negussie, T. Teklehaymanot, and E. Abeselom, “Application of composite materials in aerospace & automotive industry,” *Int. J. Adv. Eng. Manag.*, vol. 5, no. 3, pp. 697–723, 2023, doi: 10.35629/5252-0503697723.

[64] R. R. Nagavally, “Composite Materials - History, Types, Fabrication Techniques, Advantages, and Applications,” *Proc. 29th IRF Int. Conf.*, no. 2, pp. 25–30, 2016.

[65] D. Hull and T. W. Clyne, “An Introduction to Composite Materials,” *An Introd. to Compos. Mater.*, 1996, doi: 10.1017/cbo9781139170130.

[66] M. Sen, “We are IntechOpen , the world ’ s leading publisher of Open Access books Built by scientists , for scientists TOP 1 %,” *Intech*, vol. 11, no. tourism, p. 13, 2016, [Online]. Available: https://www.intechopen.com/books/advanced-biometric-technologies/liveness-detection-in-biometrics

[67] N. Al-mutairi, “Nanocomposites Materials Definitions , Types and Some of Their Applications : a Review Nanocomposites Materials Definitions , Types and Some of Their Applications : a Review,” *Eur. J. Res. Dev. Sustain.*, vol. 3, no. 2, p. 2, 2022, [Online]. Available: https://scholarzest.com/index.php/ejrds/article/view/1833

[68] N. M. Saman, M. H. Ahmad, and Z. Buntat, “Application of Cold Plasma in Nanofillers Surface Modification for Enhancement of Insulation Characteristics of Polymer Nanocomposites: A Review,” *IEEE Access*, vol. 9, no. May, pp. 80906–80930, 2021, doi: 10.1109/ACCESS.2021.3085204.

[69] X. Li *et al.*, “Heat Transfer Enhancement of Nanofluids with Non-Spherical Nanoparticles: A Review,” *Appl. Sci.*, vol. 12, no. 9, 2022, doi: 10.3390/app12094767.

[70] D. G. Panpatte and Y. K. Jhala, “Nanotechnology for agriculture: Advances for sustainable agriculture,” *Nanotechnol. Agric. Adv. Sustain. Agric.*, no. November, pp. 1–305, 2019, doi: 10.1007/978-981-32-9370-0.

[71] B. Sapkota, W. Liang, A. VahidMohammadi, R. Karnik, A. Noy, and M. Wanunu, “High permeability sub-nanometre sieve composite MoS2 membranes,” *Nat. Commun.*, vol. 11, no. 1, pp. 1–10, 2020, doi: 10.1038/s41467-020-16577-y.

[72] B. E. Hirsch *et al.*, “Anion-induced dimerization of 5-fold symmetric cyanostars in 3D crystalline solids and 2D self-assembled crystals,” *Chem. Commun.*, vol. 50, no. 69, pp. 9827–9830, 2014, doi: 10.1039/c4cc03725a.

[73] P. J. F. Harris, “Carbon nanotube composites,” *Int. Mater. Rev.*, vol. 49, no. 1, pp. 31–43, 2004, doi: 10.1179/095066004225010505.

[74] I. M. Kamal and S. M. A.- Naimi, “Polymers and Nanotechnology,” no. August, pp. 0–35, 2015.

[75] S. Islam, M. Fuad, T. Ahmed, T. Tajwar, and N. Mamun, “Results in Materials Carbon nanotubes : Structure , properties and applications in the aerospace industry,” *Results Mater.*, vol. 25, no. December 2024, p. 100654, 2025, doi: 10.1016/j.rinma.2024.100654.

[76] Y. Gogotsi, *Nanotubes and Nanofibers*. 2006.

[77] B. I. Yakobson, “Mechanical relaxation and ‘ intramolecular plasticity ’ in carbon nanotubes,” vol. 918, no. 1998, pp. 1–4, 2014, doi: 10.1063/1.120873.

[78] T. A. Diffusionless, T. Aime, M. R. Falvo, G. J. Clary, R. M. T. Ii, and V. Chi, “Bending and buckling of carbon nanotubes under large strain,” vol. 389, no. October 1997, pp. 21–23, 1999.

[79] M. M. J. Treacy, T.W.Ebbesen, and J. M. Gibson, “Exceptionally high Young;s modulud observed for individual carbon nanotubes.”

[80] Y. Q. Zhu and T. Sekine, “Collapsing carbon nanotubes and diamond formation under shock waves,” no. May, pp. 689–693, 1998.

[81] F. Li, H. M. Cheng, S. Bai, and G. Su, “Tensile strength of single-walled carbon nanotubes directly measured from their macroscopic ropes,” vol. 77, no. 20, pp. 3161–3163, 2000.

[82] Z. L. Wang, R. P. Gao, P. Poncharal, W. A. De Heer, Z. R. Dai, and Z. W. Pan, “Mechanical and electrostatic properties of carbon nanotubes and nanowires,” pp. 3–10, 2001.

[83] M. Yu, B. S. Files, S. Arepalli, and R. S. Ruoff, “Tensile Loading of Ropes of Single Wall Carbon Nanotubes and Their Mechanical Properties Tensile Loading of Ropes of Single Wall Carbon Nanotubes and their Mechanical Properties,” no. September, 2014, doi: 10.1103/PhysRevLett.84.5552.

[84] R. H. Baughman, A. A. Zakhidov, and W. A. De Heer, “Carbon Nanotubes — the Route Toward Applications,” vol. 297, no. August, pp. 787–793, 2002.

[85] A. M. K. Esawi and M. M. Farag, “Materials & Design Carbon nanotube reinforced composites : Potential and current challenges,” vol. 28, pp. 2394–2401, 2007, doi: 10.1016/j.matdes.2006.09.022.

[86] Y. Chiker, M. Bachene, M. Guemana, B. Attaf, and S. Rechak, “Free vibration analysis of multilayer functionally graded polymer nanocomposite plates reinforced with nonlinearly distributed carbon-based nanofillers using a layer-wise formulation model,” *Aerosp. Sci. Technol.*, vol. 104, p. 105913, 2020, doi: 10.1016/j.ast.2020.105913.

[87] Z. X. Lei, L. W. Zhang, and K. M. Liew, “Free vibration analysis of laminated FG-CNT reinforced composite rectangular plates using the kp-Ritz method,” *Compos. Struct.*, vol. 127, pp. 245–259, 2015, doi: 10.1016/j.compstruct.2015.03.019.

[88] J. C. Halpin, “Journal of Composite Materials,” pp. 3–7, 2014, doi: 10.1177/002199836900300419.

[89] I. Nistor, O. Pantalé, and S. Caperaa, “Numerical implementation of the eXtended Finite Element Method for dynamic crack analysis,” *Adv. Eng. Softw.*, vol. 39, no. 7, pp. 573–587, 2008, doi: 10.1016/j.advengsoft.2007.06.003.

[90] J. Dolbow, N. Moës, and T. Belytschko, “Modeling fracture in Mindlin-Reissner plates with the extended finite element method,” *Int. J. Solids Struct.*, vol. 37, no. 48, pp. 7161–7183, 2000, doi: 10.1016/S0020-7683(00)00194-3.

[91] C. H. N. and Y. S. P. CONSTANCE YANG*, “Elastic Wave Propagation in Heterogeneous Plates,” *Bull. Seismol. Soc. Am.*, vol. 60, no. 3, pp. 769–784, 1966, doi: 10.1299/jsmekansai.2003.78._5-51_.

[92] C. Yasser, “COMPORTEMENT MÉCANIQUE DES PLAQUES COMPOSITES HYBRIDES RENFORCÉES AVEC DES PLIS EN NANOTUBE DE CARBONE

MONO-FEUILLETS," university yahia fares medea, 2021.

[93] J. . WHITNEY, "W / A Shear Correction Factors for Orthotropic Laminates under Static load," vol. 32, no. 2, pp. 302–304, 2016.

[94] J. Marsden and J. Scheurle, "The reduced Euler-Lagrange equations," *Dyn. Control Mech. Syst. Falling Cat Relat. Probl.*, pp. 139–164, 1993, doi: 10.1090/fic/001/07.

[95] Z. X. Lei, K. M. Liew, and J. L. Yu, "Buckling analysis of functionally graded carbon nanotube-reinforced composite plates using the element-free kp-Ritz method," *Compos. Struct.*, vol. 98, pp. 160–168, 2013, doi: 10.1016/j.compstruct.2012.11.006.

[96] B. Stahl and L. M. Keer, "Vibration and stability of cracked rectangular plates," *Int. J. Solids Struct.*, vol. 8, no. 1, pp. 69–91, 1972, doi: 10.1016/0020-7683(72)90052-2.

[97] K. M. Liew, K. C. Hung, and M. K. Lim, "A solution method for analysis of cracked plates under vibration," *Eng. Fract. Mech.*, vol. 48, no. 3, pp. 393–404, 1994, doi: 10.1016/0013-7944(94)90130-9.

[98] M. Bachene, R. Tiberkak, and S. Rechak, "Vibration analysis of cracked plates using the extended finite element method," *Arch. Appl. Mech.*, vol. 79, no. 3, pp. 249–262, 2009, doi: 10.1007/s00419-008-0224-7.

[99] N. D. Duc and P. P. Minh, "Free vibration analysis of cracked FG CNTRC plates using phase field theory," *Aerosp. Sci. Technol.*, vol. 112, p. 106654, 2021, doi: 10.1016/j.ast.2021.106654.

[100] R. Moradi-Dastjerdi and F. Aghadavoudi, "Static analysis of functionally graded nanocomposite sandwich plates reinforced by defected CNT," *Compos. Struct.*, vol. 200, pp. 839–848, 2018, doi: 10.1016/j.compstruct.2018.05.122.

[101] H. S. Shen and Y. Xiang, "Nonlinear analysis of nanotube-reinforced composite beams resting on elastic foundations in thermal environments," *Eng. Struct.*, vol. 56, pp. 698–708, 2013, doi: 10.1016/j.engstruct.2013.06.002.

[102] P. Zhu, Z. X. Lei, and K. M. Liew, "Static and free vibration analyses of carbon nanotube-reinforced composite plates using finite element method with first order shear deformation plate theory," *Compos. Struct.*, vol. 94, no. 4, pp. 1450–1460, 2012, doi: 10.1016/j.compstruct.2011.11.010.

[103] C. P. Wu and H. Y. Li, "Three-dimensional free vibration analysis of functionally graded carbon nanotube-reinforced composite plates with various boundary conditions," *JVC/Journal Vib. Control*, vol. 22, no. 1, pp. 89–107, 2016, doi: 10.1177/1077546314528367.

[104] B. Huang *et al.*, "Bending and free vibration analyses of antisymmetrically laminated carbon nanotube-reinforced functionally graded plates," *J. Compos. Mater.*, vol. 51, no. 22, pp. 3111–3125, 2017, doi: 10.1177/0021998316685165.